



Mapping and Assessing Surface Morphology of Holocene Lava Flow in Krafla, NE Iceland, Using Remote Sensing

Muhammad Aufaristama



**Faculty of Life and Environmental Sciences
University of Iceland
2015**

Mapping and Assessing Surface Morphology of Holocene Lava Flow in Krafla, NE Iceland, Using Remote Sensing

Muhammad Aufaristama

30 ECTS thesis submitted in partial fulfillment of a
Magister Scientiarum degree in Geo-information Science and Earth
Observation for Environmental Modelling

Advisors

Dr. Ármann Höskuldsson
Assoc. Prof. Ingibjörg Jónsdóttir
Professor Rannveig Ólafsdóttir

Faculty Representative
Dr. Kolbeinn Árnason

Faculty of Life and Environmental Sciences
School of Engineering and Natural Sciences
University of Iceland
Reykjavik, May 2015

Mapping and Assessing Surface Morphology of Holocene Lava Flow in Krafla, NE
Iceland, Using Remote Sensing

30 ECTS thesis submitted in partial fulfillment of a *Magister Scientiarum* degree in Geo-
information Science and Earth Observation for Environmental Modelling

Copyright © 2015 Muhammad Aufaristama
All rights reserved

Faculty of Life and Environmental Sciences
School of Engineering and Natural Sciences
University of Iceland
Askja, Sturlugötu 7
107, Reykjavík
Iceland

Telephone: 525 4000

Bibliographic information:

Muhammad Aufaristama, 2015,
*Mapping and Assessing Surface Morphology of Holocene Lava Flow in Krafla, NE Iceland,
Using Remote Sensing*
Master's thesis, Faculty of Life and Environmental Science, University of Iceland, pp.101.

Printing: Háskólaprent
Reykjavík, Iceland, May 2015

Abstract

Iceland is well known for its volcanic activity due to being situated on the spreading Mid Atlantic Ridge and a hot spot. This landmass is located in the North Atlantic Ocean between Greenland and Norway. In the past 1000 years there were about 200 eruptions occurring in Iceland, meaning volcanic eruptions occur on average every four to five years. Iceland currently has 30 active volcano systems, distributed evenly throughout the so-called Neovolcanic Zone. One of these volcanic systems is the Krafla central volcano. Krafla is located in northern Iceland at latitude 65°42'53" N, and longitude 16°43'40" W. Krafla has produced two volcanic events in historic times: 1724-1729 (Myvatn Fires) and 1975-1984 (Krafla Fires). The Krafla Fires began in December 1975 and lasted until September 1984. This resulted in about 36 km² covered by lava; a volume of 0.25-0.3 km³. Previous studies of lava surface morphology at Krafla focused on an open channel area mapped as 55% aa lava, 32% as pahoehoe, and the remaining 13% as the main lava channel. The earlier study was mostly field mapping, video recording and measuring pre-flow topography from aerial photographs. Therefore, studies by remote sensing are essential as a complementary tool to previous investigations and to extend the area of mapping. Using maximum likelihood and Spectral Angle Mapper (SAM) classification approach by selecting spectral reflectance endmembers, this study has successfully produced three detailed maps of lava surface morphology in Krafla lava field from three satellite images: SPOT 5 (Multispectral & Panchromatic), Landsat 8 OLI (Multispectral) and EO-1 Hyperion (Hyperspectral) satellite images. The overall accuracy of these lava morphology maps are 67.33% (SPOT 5), 52.67% (Landsat 8 OLI) and 61.33% (EO-1 Hyperion). These results show that remote sensing is an acceptable alternative to field mapping and assessing the lava surface morphology in the Krafla lava field. In order to get validation of the satellite image's spectral reflectance, in-situ measurements of the lava field's spectral reflectance using ASD FieldSpec3 is essential.

Keywords: Iceland, Neovolcanic Zone, Remote Sensing, Lava morphology, Spectral reflectance, Maximum Likelihood, Spectral Angle Mapper (SAM)

Ágrip

Eldvirkni á Íslandi tengist fráreksbelti Atlantshafsins og óvenjumikilli kvikuframleiðslu undir Íslandi, kennt heitum reit. Síðastliðin þúsund ár er talið að um 200 eldgos hafi orðið hér á landi. Síðustu hundrað ár hafa hinsvegar orðið um 44 eldgos eða að meðaltali eitt gos á tveggja og hálfársfresti. Um þrjátíu eldstöðvakerfi eru virk á landinu sem eru nokkuð jafn dreifð um eldvirka beltið. Eitt þessara kerfa er megineldstöðin Krafla á Norðurlandi. Á sögulegum tíma hafa tvær goshrinur átt sér stað í Kröflu: Mývatnseldar 1724-1729 og Kröflueldar sem hófust í desember 1975 og stóðu yfir, með hléum, fram í september 1984. Á þessum tíma rann hraun yfir um 36 km² lands og rúmmál þess var metið 0,25-0,3 km³. Fyrri rannsóknir á yfirborðsgerð hraunsins gefa til kynna að 55% séu apalhraun, 32% helluhraun og 13% hraunár og rásir. Byggja þessar niðurstöður einkum á vettvangsrannsóknum, myndböndum og samanburði loftmynda fyrir og eftir gos. Í þessari rannsókn eru fyrri greiningar bornar saman við flokkanir á hrauni frá Kröflueldum með fjarkönnunargögnum úr gervitunglum. Tvær aðferðir, "Maximum Likelihood" og "Spectral Angle Mapper", voru nýttar til að flokka hraunið og kortleggja eftir SPOT-5, LANDSAT-8 og EO-1 gervitunglamyndum úr fjölrófsskönnum. Af þessum þremur myndgerðum reyndust greiningar úr SPOT-5 vera áreiðanlegastar, í samanburði við fyrri kort, eða 67,33%, en samsvarandi niðurstöður með greiningum með EO-1 Hyperion myndum voru 61,33% og LANDSAT-8 OLI 52,67%. Niðurstöðurnar sýna að fjarkönnun geti nýst við flokkun á yfirborðsgerð hrauna, en til að bæta flokkunaraðferðir er nauðsynlegt að gera ýmsar mælingar á vettvangi, m.a. með geislunar/endurvarpsmælum sambærilegum við ASD FieldSpec3.

Lykilorð: Ísland, eldvirka beltið, fjarkönnun, Maximum Likelihood, Spectral Angle Mapper.

Table of Contents

List of Figures	vii
List of Tables.....	xii
Abbreviations.....	xiii
Acknowledgements	xiv
1 Introduction.....	1
1.1 Research Objectives.....	5
1.1.1 General Objectives	5
1.1.2 Specific Objectives	5
1.1.3 Research Questions	5
1.1.4 Hypotheses	5
2 Literature Review	7
2.1 Lava Morphology	7
2.2 Remote Sensing	11
2.3 Sensor and Satellite.....	11
2.3.1 Landsat 8 OLI	12
2.3.2 EO-1 Hyperion.....	13
2.3.3 SPOT 5.....	13
2.4 Spectral Reflectance	14
2.4.1 Lava Spectral Reflectance Curves	16
3 Study Area	19
3.1 Iceland's Volcanic Zone	19
3.2 North Volcanic Zone	22
3.3 Krafla	24
3.4 Krafla's Lava Morphology.	26
4 Data and Methods	31
4.1 Visual Image Interpretation	33
4.1.1 SPOT 5 Panchromatic Pre-Processing.....	33
4.1.2 Creation of random points	36
4.2 Histogram/Pixel Interpretation	38
4.2.1 SPOT 5 Pre-Processing.....	38
4.2.2 SPOT 5 training samples selection	41
4.2.3 Pixel histogram distribution.....	43
4.2.4 Supervised classification (Maximum likelihood classification).....	43
4.3 Spectral Image interpretation.....	44
4.3.1 Multispectral Image	44
4.3.2 Landsat 8 OLI Pre-Processing	44
4.3.3 Landsat 8 OLI spectral endmember selection	48

4.3.4 Hyperspectral Image.....	52
4.3.5 EO-1 Hyperion Pre-Processing	52
4.3.6 EO-1 Hyperion spectral endmember selection.....	57
4.3.7 EO-1 Hyperion spectral smoothing	57
4.3.7 Spectral Angle Mapper (SAM) classification	61
4.4 Accuracy Assessment.....	63
5 Analysis and Results.....	67
5.1 Lava Morphology Visual Interpretation	67
5.2 Lava Morphology Histogram Distributions	69
5.3 Lava Morphology Spectral Reflectance Analysis	73
5.3.1 Multispectral reflectance analysis	74
5.3.2 Hyperspectral reflectance analysis	76
5.4 Lava Morphology Classification	78
5.4.1 Effect of training samples in classification	78
5.4.2 Effect of endmember spectral in classification	78
5.5 Lava Morphology Accuracy Assessment.....	80
5.5.1 Effect of sample size, references and data quality on accuracy assessment	80
5.5.2 Descriptions of Kappa Statistics and Their Advances over Normal Accuracy Assessment	82
6 Discussions.....	83
6.1 Identifying lava surface morphology using remote sensing.....	83
6.2 Lava surface morphology in the Krafla lava fields	84
5 Concluded Remarks and Reccommendations	85
7.1 Concluded Remarks.....	85
7.1.1 Lava Morphology Histogram Distributions	85
7.1.2 Lava Morphology Spectral Reflectance	85
7.1.2 Lava Morphology Mapping and Assessing.....	85
7.2 Recommendations	86
References	87
Appendix I.....	93
Appendix II.....	101

List of Figures

Fig. 1 Frequency of lava flow types in Iceland	2
Fig. 2 Spectral band of Landsat 7 and spectral reflectance properties	2
Fig. 3 Diagrams showing a comparison between field spectra of selected sites (blue lines) and the corresponding Hyperion spectra sampled at the same location (red lines) in Mt. Etna	3
Fig. 4 Krafla central volcanoes and the 1975-84 lava field.....	4
Fig. 5 Cross section of a generic basaltic lava flow, showing some of the basic structural features that should be described when mapping flows. Flow surfaces, if preserved, presents variety of textures that range from smooth, ropy pahoehoe to spiny, rubbly aa lavas	7
Fig. 6 Lava morphology from Krafla lava field and Craters of the moon Lava field (a) Shelly Pahoehoe lava in Krafla; (b) Spinny pahoehoe lava in Craters of the moon (c) Rubbly Aa lava in Krafla; (d) Cauliflower Aa in Krafla; and (e) Slabby pahoehoe lava in Craters of the moon	9
Fig. 7 Lava morphology from Krafla lava field base on aerial photograph (a) Shelly Pahoehoe lava; (b) Spinny pahoehoe lava; (c) Rubbly Aa lava; (d) Cauliflower Aa; and (e) Slabby pahoehoe.....	10
Fig. 8 The classification of EM spectrum	11
Fig. 9 Interactions of EM radiation with the atmosphere and the Earth's.....	14
Fig. 10 Schematic diagrams showing (a) specular and (b) diffuse.....	15
Fig. 11 Average VNIR spectra of fresh and weathered surfaces of CRBG samples, five absorptions are shown	16
Fig. 12 Average spectral signature for different type of lava from Mt. Etna).....	17
Fig. 13 Mean reflectance spectra for Mauna Ulu surface units, derived from (a) ASTER, bands 1 to 3, and (b) MASTER, bands 1 to 11.....	18
Fig. 14 Iceland situated in the North Atlantic Ocean, at the junction of the Reykjanes and Kolbeinsey Ridges. The Iceland Basalt Plateau is marked by the darker dotted line around Iceland, and the present location of the mantle plume is marked by the red star. The purple stars show the previous locations of the mantle plume.....	19

Fig. 15 Map presenting the Neovolcanic Zone at the junction of the Reykjanes and Kolbeinsey Ridges to the south and north respectively. The Snaefellsnes and Öraefajökull Flank Zones are also shown, as well as the South Iceland Seismic Zone.....	20
Fig. 16 The Northern Volcanic Zone and its fissure swarms. Blue frame in inserted and main Figure shows the location of the Northern Volcanic Zone in Iceland.	23
Fig. 17 Lava flows produced by the eruptions of the 1975–84 Krafla Fires.....	25
Fig. 18 Lava flows from the Krafla Fires. The open-channel lava flow and initial pahoehoe.	27
Fig. 19 Surface morphology and lava channels of the 1984 open-channel lava flow.....	28
Fig. 20 A general flow chart of the study's work procedure. The four main steps are emphasized by different colors.	32
Fig. 21 Base map making process of the Krafla lava flow used for the surface analysis (a) Overlaying Rossi (1997) open channel map with aerial photograph; (b) Overlaying Rossi (1997) open channel map with aerial photograph and include spot 5 panchromatic.	34
Fig. 22 (a) Image before enhancement in grayscale; (b) image before enhancements in rainbow scale; (c) Image after the linear 5% enhancements in grayscale; (d) image after the linear 5% enhancement s in rainbow scale..	35
Fig. 23 The create random points tool in ArcGIS with 30 point each morphology and 20 meters minimum distance.....	36
Fig. 24 The location of the 150 random points generated in the Krafla's lava field.....	37
Fig. 25 (a) SPOT 5 Image before pan sharpening; (b) SPOT 5 Image before pan sharpening.	39
Fig. 26 (a) SPOT 5 Image before histogram equalization; (b) SPOT 5 Image after histogram equalization.	40
Fig. 27 Nine samples were collected from SPOT 5 image of Krafla area : (1) Rubbly AA; (2) sandur deposit; (3) Old Lava; (4) Pahoehoe; (5) Cauliflower AA; (6) Shelly Pahoehoe; (7) Upper Pleistocene formation; (8) Vegetation; and (9) Water.	41
Fig. 28 Nine sample points from SPOT 5 image of Krafla area : (1) Rubbly AA; (2) sandur deposit; (3) Old Lava; (4) Pahoehoe; (5) Cauliflower AA; (6) Shelly Pahoehoe; (7) Upper Pleistocene formation; (8) Vegetation; and (9) Water.	42
Fig. 29 Number of pixels which sampled for each class.....	43
Fig. 30 Radiometric calibration to convert into TOA reflectance.....	46

Fig. 31 Dark object subtraction (DOS) to convert into surface reflectance.	46
Fig. 32 (a) Image before convert to TOA reflectance; (b) Image after convert to TOA reflectance; (c) Image after convert to surface reflectance.....	47
Fig. 33 Illustration of mixed pixels and pure pixel.....	48
Fig. 34 Nine spectral endmember were collected from Landsat 8 OLI of Krafla area: (1) Rubbly AA; (2) sandur deposit; (3) Old Lava; (4) Pahoehe; (5) Cauliflower AA; (6) Shelly Pahoehe; (7) Upper Pleistocene formation; (8) Vegetation; and (9) Water.	49
Fig. 35 Spectral endmember points were collected from Landsat 8 OLI False color (7-4-6). area : (1) Rubbly AA; (2) sandur deposit; (3) Old Lava; (4) Pahoehe; (5) Cauliflower AA; (6) Shelly Pahoehe; (7) Upper Pleistocene formation; (8) Vegetation; and (9) Water.	50
Fig. 36 Landsat 8 OLI spectral reflectance curve from nine endmember points in the Krafla area.....	51
Fig. 37 The hyperspectral data cube structure. (a) Scan line: a push-broom sensor on an airborne or spaceborne platform collects spectral information for a one-dimensional row of cross-track pixels (b) Successive scan lines covered of the spectra for each row of cross-track pixels are stacked to acquire a three-dimensional hyperspectral data cube. Spatial information of a scene is represented by the x and y dimensions of the cube and the amplitude spectra of the pixels are projected into the z dimension. (c) The collected three-dimensional hyperspectral data cube presented as a stack of two-dimensional spatial images, each corresponding to a specific narrow waveband. A hyperspectral data cube usually contains of hundreds of such stacked images. (d) Spectral reflectance curves plotted for each material.....	53
Fig. 38 Example of vertical strip that appear on the EO-1 Hyperion band image (1) Band 125 and (2) Band 221.	54
Fig. 39 Hyperion image band 221; (1) before filtered by SPEAR Vertical Stripe Removal; (2) after filtered by SPEAR Vertical Stripe Removal.	55
Fig. 40 Schematic flow FLAASH code showing basic steps involved in radiance to reflectance conversion	56
Fig. 41 Parameters for ENVI FLAASH which used in this method.	56
Fig. 42 EO-1 Hyperion false color composite (46-33-20): (a) before applied FLAASH module; (b) after applied FLAASH module, there were horizontal strip which causes brightness degraded.....	58
Fig. 43 Eight spectral endmember were collected from EO-1 Hyperion of Krafla area : (1) Cauliflower AA; (2) Old lava; (3) Pahoehe; (4) Rubbly AA; (5) Sandur deposit; (6) Shelly Pahoehe; (7) Upper Pleistocene formation; and (8) Vegetation.	58

Fig. 44 Eight spectral endmember points were collected from EO-1 Hyperion of Krafla area : 1) Cauliflower AA; (2) Old lava; (3) Pahoehoe; (4) Rubbly AA; (5) Sandur deposit; (6) Shelly Pahoehoe; (7) Upper Pleistocene formation; and (8) Vegetation..	59
Fig. 45 EO-1 Hyperion spectral reflectance curve from nine endmember points in the Krafla area; (a) before smoothing; (b) after moving average smoothing.....	60
Fig. 46 (a) Maximum angles parameters for Landsat 8 OLI; (b) maximum angles parameters for EO-1 Hyperion.....	62
Fig. 47 Reference points overlay in (a) SPOT 5 classification; (b) Landsat 8 OLI classification; (c) EO-1 Hyperion classification.	65
Fig. 48 Surface morphology of Krafla based on visual image interpretation.	67
Fig. 49 Small patches of cauliflowers aa appear on aerial photograph (yellow line).	68
Fig. 50 Pixel histogram distribution of lava morphology in Krafla; (1) Cauliflower AA; (2) Rubbly AA; (3) Pahoehoe; and (5) Old lava.....	70
Fig. 51 Pixel histogram distribution of the area outside lava; (1) Vegetation; (2) Upper Pleistocene formation; (3) sandur deposit; and (4) water.	71
Fig. 52 SPOT 5 Mean pixel intensity plot for all bands in Krafla.	72
Fig. 53 Feature space plot band 2 / band 4.....	72
Fig. 54 Feature space plot band 3 / band 4.....	73
Fig. 55 Spectral reflectance curve of basalt from USGS, red lines show the absorptions features.	74
Fig. 56 Spectral reflectance of lava morphology comparison; (a) between laboratory measurement and lava in krafla lava field; (b) between cauliflowers aa and rubbly aa; (c) between shelly pahoehoe and pahoehoe.	75
Fig. 57 Spectral reflectance of lava morphology comparison between basalt from USGS laboratory measurement and basalt lava in Krafla lava field from remote hyperspectral remote sensing with the absorptions features.	76
Fig. 58 Spectral reflectance of lava morphology comparison between cauliflowers aa and rubbly aa in Krafla lava field, blue circle show the absorption feature between 2200-2300 nm found in rubbly aa.	77
Fig. 59 Spectral reflectance of lava morphology comparison between pahoehoe and shelly pahoehoe in Krafla lava field, in general pahoehoe have stronger absorption feature in Fe^{2+} and H_2O	77
Fig. 60 Krafla's Lava morphology classification base on maximum likelihood classification.....	79

Fig. 61 (a) Landsat 8 OLI SAM classification result; (b) EO-1 Hyperion SAM classification result	80
Fig. 62 Effect of sample size to accuracy assessment for different classified satellites data in Krafla lava field.....	81
Fig. A1 Band ratio $5/4 \cdot 3/4$ on Landsat 8 to discriminate between mafic and nonmafic rocks.	101

List of Tables

Table 1. Characteristic of spectral band of Landsat 8	13
Table 2. Volcanic systems in Iceland.	21
Table 3. Description of morphological lava types of the 1984 open-channel lava flow in Krafla.....	29
Table 4. Description of satellites/aerial data which used in this study.	31
Table 5. Description of SPOT 5 data which used in this study.....	38
Table 6. List of bad bands on the EO-1 Hyperion image.....	52
Table 7. Example of confusion matrix.	63
Table 8. Results of overall, producer and user accuracy including the Kappa statistics for three satellites image(1) SPOT 5; (2) Landsat 8 OLI; and (3) EO-1 Hyperion	82
Table A1. Hyperion spectral coverage and detail of not calibrated bands (Beck, 2003)....	93
Table A2. SPOT 5 image overall statistics of lava morphology in the Krafla lava field..	101

Abbreviations

NVZ = North Volcanic Zone

SPOT = *Satellite Pour l'Observation de la Terre*

EO-1 = Earth Observing One

OLI = Operational Land Imager

NIR = Near Infrared

SWIR = Short Waves Infrared

VNIR = Visible and Near Infrared

TOA = Top of Atmosphere

DOS = Dark of Subtraction

FLAASH = Fast Line-of-sight Atmospheric Analysis of Spectral Hypercubes

SAM = Spectral Angle Mapper

Acknowledgements

In the Name of Allah, the Most Beneficent and the Most Merciful. Alhamdulillah, all the praise and thanks be to Allah, the Almighty who gave me the ability to successfully finish this thesis.

I would like to thank the LPDP Scholarship for granting me the fellowship to give a great opportunity for study abroad and following course in Erasmus Mundus MSc Programme in Geo-information Science and Earth Observation for Environmental Modelling and Management (GEM).

I would like to give full of admiration, gratitude and big thanks to my supervisor Dr. Ármann Höskuldsson, Assoc. Prof. Ingibjörg Jónsdóttir and Prof. Rannveig Ólafsdóttir who kindly and patiently guides and supports me with their knowledge to accomplish this research.

I would like to thanks to ITC, University of Twente and University of Iceland to give me a chance to have a great study on world class and international environment.

I am grateful to Institute of Earth Sciences, University of Iceland for provide satellite data and aerial photographs of Krafla.

My sincere thanks to the five coordinators of the GEM programme especially for Prof. Rannveig Ólafsdóttir who kindly supported and motivated me since I arrived in Iceland. I am really grateful to them and Dr. Michael Wier and Drs. Raymond Nijmeijer as course coordinator during in ITC, University of Twente for their continuous guidance and support during the study.

I would like to express my gratitude to all the teachers of four institutions for their valuable knowledge and also to the Ms. Laura Windig and Ms. Marion Pierik for their help with information and logistics.

I would like to give humble appreciation to all my fellow classmates and Indonesian students in ITC, University of Twente who support me during the study.

Finally my deepest gratitude to my parents Sudarisman Sofian and Nenni Nuraeni, and my sisters Annisa Benaquina and Azeisha Dienarahmani, and my beloved friend Fella Tiffany who have always supported and inspired me to strive for higher quality of life.

1 Introduction

The Icelandic landmass was produced by repeated volcanic activity of various type, and nearly all types of volcanoes and styles of eruptions known on earth can be found there (Dugmore & Vésteinsson, 2012). According to Thordarson & Larsen (2007), eruptions styles range from explosive (produce over 95% of tephra) to effusive (produce over 95% of lava). Iceland has a high concentration of active volcanoes due to its location on the mid-Atlantic Ridge (divergent tectonic plate boundary) in combination with its position on a volcanic hot spot located underneath the island. Since the Norse settlement of Iceland in AD 874, 13 of 30 active volcano in Iceland have erupted (Thordarson & Höskuldsson, 2008). The occurrence of a volcanic eruption every fourth year on average makes Iceland one of the liveliest places in the world with regards to volcanic eruptions. Over the past 500 years, Iceland's volcanoes have erupted a third of the total global lava output (Kozák & Vladimír, 2010).

Lava is magma that reaches the surface and pours out over the landscape. Classified by flow behavior and/or morphology, there are three main types of lava flows in Iceland (1) aa lava; (2) pahoehoe lava and (3) pillow lava (Guðmundsson & Kjartansson, 2007). Prehistoric volcanic remains from the Holocene (younger than 10,000 – 12,000 years) are usually not glacially smoothed, but can appear to be quite old because of erosion and weathering which are rapid processes in Iceland (Guðmundsson & Kjartansson, 2007). Lava morphology refers to the characteristics of the surface morphology of a lava flow after solidification. According to Thordarson & Höskuldsson (2008), lava eruptions in Iceland takes place at monogenetic point-source and fissure type volcanoes as well as in central volcanoes typically occurring on caldera ring fractures or radial fissures. Purely effusive basalt and silicic events are known in the post-glacial volcanic succession, but effusion of intermediate magma without accompanying explosive phase has yet to be recorded. The basalt lava morphology spectrum spans the range of pahoehoe, rubbly pahoehoe to aa (Thordarson & Höskuldsson, 2008). Fig. 1 shows that the first two are by far the most common lava types in Iceland, representing 83% of the 190 lava flows analysed so far and fissure-fed pahoehoe are as common as shield forming pahoehoe.

Over the last 20 years or so a number of researchers have documented Holocene eruptive events and mapping distribution of Holocene lava morphology all over the world including Iceland (e.g. Rossi & Gudmundsson, 1996; Rossi, 1997; Kennish and Lutz, 1998; Duraiswami et al., 2008; Duraiswami et al., 2014; Murcia et al., 2014). Most of these studies are field mapping. Although field analysis and measurements are relatively accurate, such methods are usually time consuming especially when the lava field extends over large area. In order to improve accuracy and time of labour intensive field mapping, remote sensing should be the first option. Development of remote sensing for geological purposes is rapidly increasing. Remote sensing provides spectral, spatial, and temporal coverage for both geologic mapping and monitoring at numerous volcanoes throughout the world.

Remote sensing can be described as any technique which uses a remote device to detect and measure EM radiation (Timmermans, 1995). According to that theory there are two important things (1) wavelength of the radiation and (2) spectral reflectance. Satellite images consist of specific characteristic wavelength ranges. This wavelength spectrum is represented as bands in the image and shows the spectral signature for different properties (Fig. 2). Remote Sensing

technology for lava flow mapping has been well established for several years. According to recent studies, there are several satellites images that can be used for lava flow mapping (1) thermal infrared; (2) radar; and (3) optical (i.e. Flynn et al., 2001; Lombardo and Buongiorno, 2006; Lu et al., 2004; Tarquini & Favalli, 2011; Smets et al., 2010).

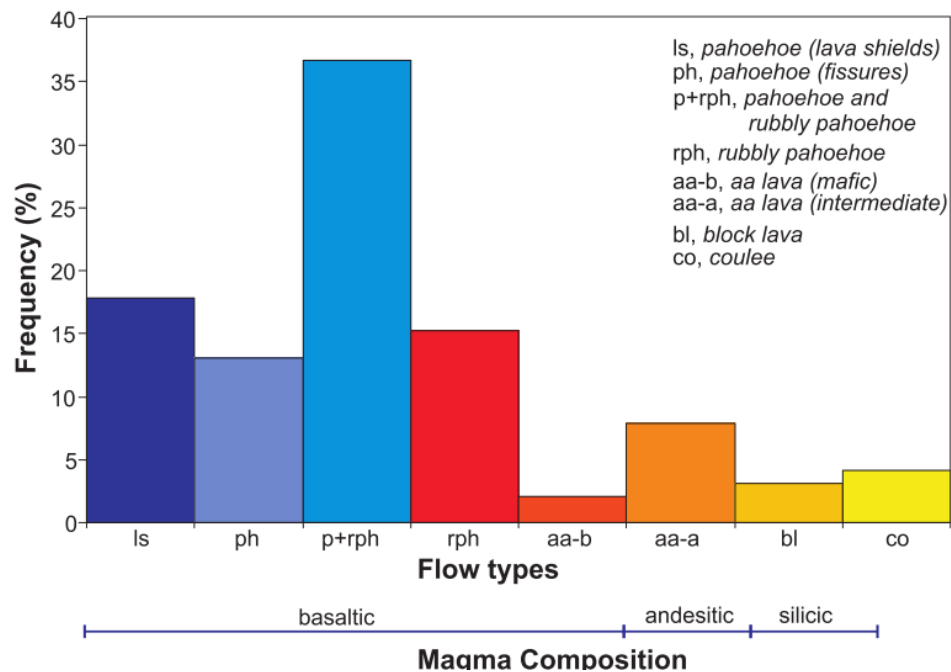


Fig. 1 Frequency of lava flow types in Iceland (Thordarson & Höskuldsson, 2008).

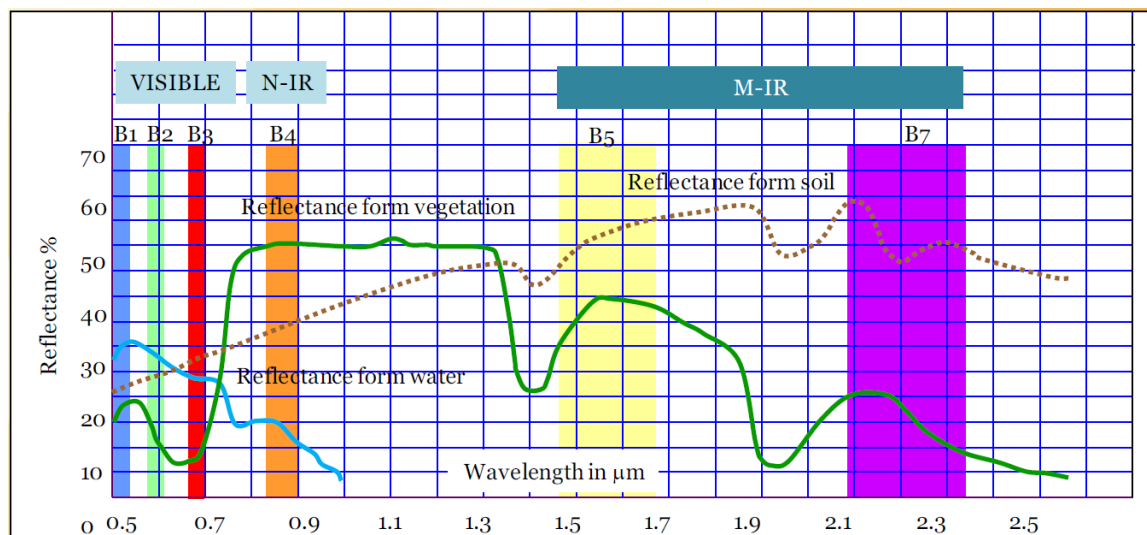


Fig. 2 Spectral band of Landsat 7 and spectral reflectance properties (Lwin, 2008).

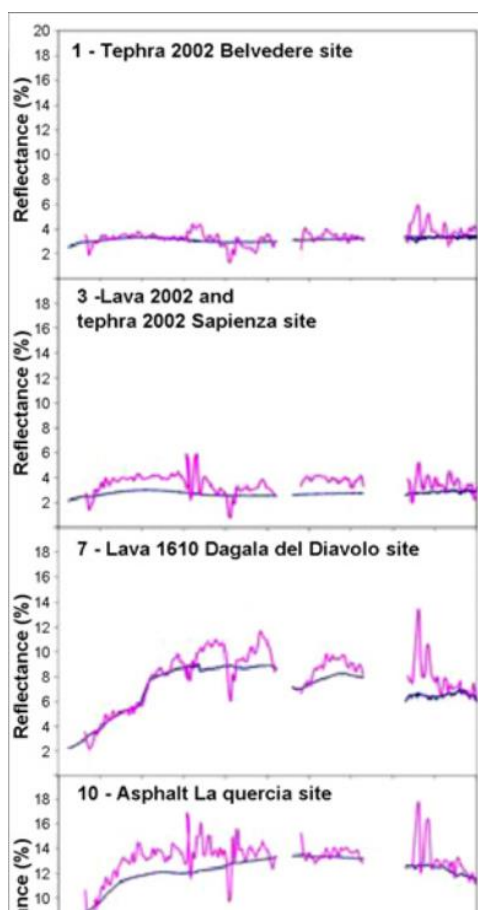


Fig. 3 Diagrams showing a comparison between field spectra of selected sites (blue lines) and the corresponding Hyperion spectra sampled at the same location (red lines) in Mt. Etna (Spinetti et al., 2009).

Furthermore, Byrnes et al. (2004) provide a detailed characterization of the surface morphology of Mauna Ulu, Hawaii and present a remote sensing approach using ASTER data and MASTER (Multispectral) to mapping and interpreting the emplacement of lava flow fields. Their results show that the mean spectral reflectance curves allow characterization of lava surface morphology. The study concludes that pahoehoe and other volcanic materials have higher reflectance compared with aa. A similar study to Byrnes et al. (2004) was done by Spinetti et al (2009) using spectral ground measurement on volcanic materials in Mt. Etna, Italy which were compared with hyperspectral (EO-1 Hyperion) data (Fig. 3). Their results show that based on spectral analysis, air-fall deposits are characterized by low reflectance values. This distinguishes them from other surface materials. Old lava flows show highest reflectance values due to weathering and vegetation cover.

Krafla lava field is located in the North East of Iceland (Fig. 4). During the Holocene, Krafla has many eruptive events, including two in historical time: 1724-1729 and 1975-1984 (Thordarson & Larsen, 2007). The latest eruptive episode, known as the “Krafla Fires”, lasted from 1975–1984, and resulted in 21 tectonic events, and 9 volcanic eruptions (Björnsson, 1985; Einarsson, 1991). This eruption covered an area of 36 km² lava; a volume of 0.25-0.3 km³ (Einarsson, 1991).

The Krafla lava field was chosen for this study due to it being mostly free of vegetation cover. The morphology of an open channel lava flow in Krafla has previously been mapped by Rossi (1997) at which time five flow facies were recognized: (1) the initial pahoehoe sheet; (2) proximal slab pahoehoe and aa; (3) shelly-type overflows from the channel; (4) distal rubbly aa lava; and (5) secondary outbreaks of toothpaste lava and cauliflower aa, around 55% is classified as aa, 32% as pahoehoe and the rest 13% is main lava channel. The previous study by Rossi (1997) was primarily field mapping, video recording and measuring pre-flow topography from aerial photographs. Therefore, a study by remote sensing is required as a complementary tool to previous investigations. The aim of this study is detailed mapping and assessment of surface morphology of the 1975-1984 Krafla lava field using remote sensing. There are three satellite image data for this study (1) SPOT 5; (2) Landsat 8 OLI; and (3) EO1-Hyperion. We focus on spectral reflectance signature and pixel histogram to map lava surface morphology, and then compare the result with very high resolution aerial photography and results from Rossi (1997). This map describes the variation in surface morphology within the Krafla lava field. This thesis will discuss the results and various limitations of this study related to the outcome from lava visual interpretation, lava histograms distribution, lava spectral reflectance and accuracy assessment. The effect of temporal variations, quality of

reference data, processed data, sample size and sample selection for reference points will also be discussed.

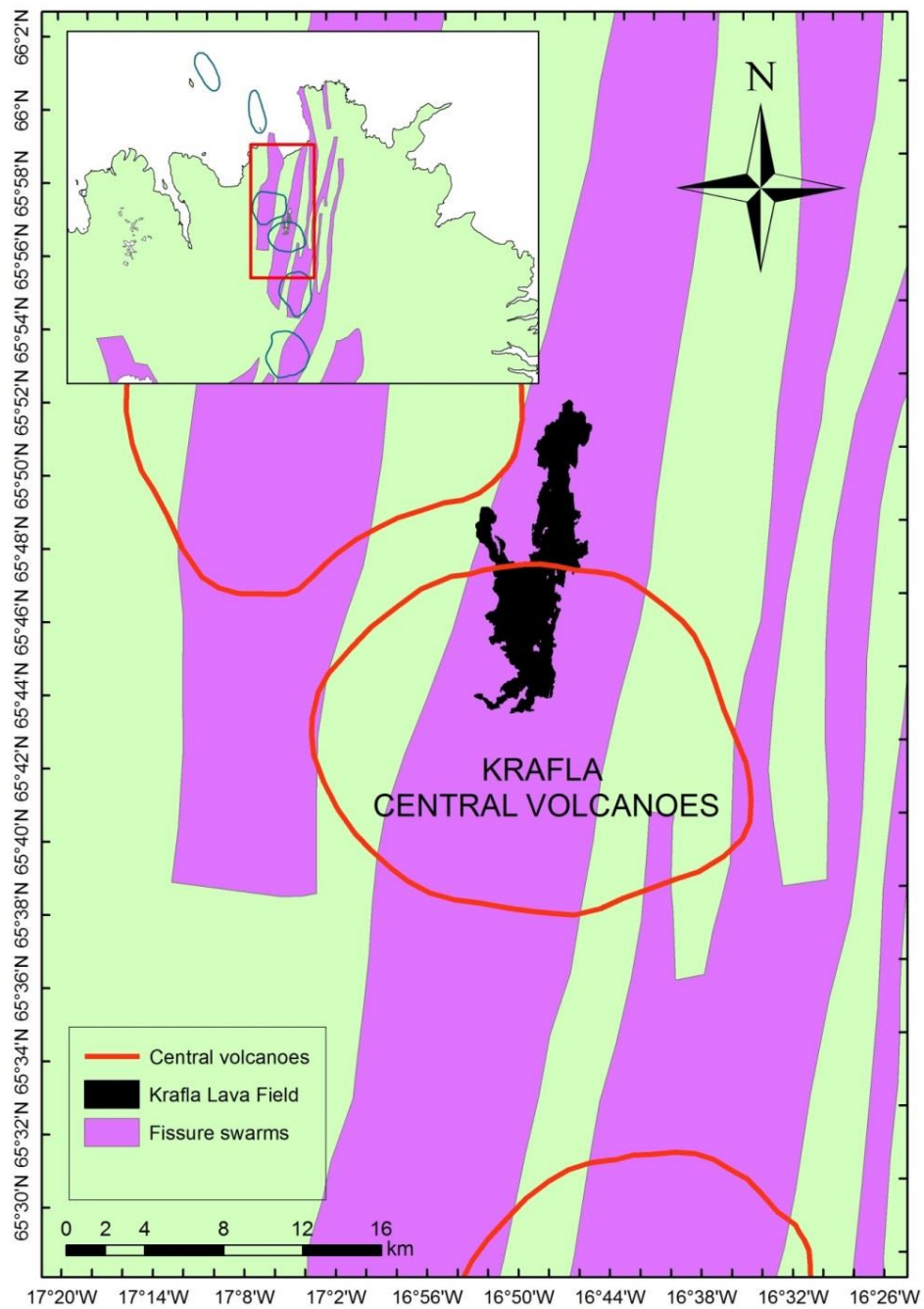


Fig. 4 Krafla central volcanoes and the 1975-84 lava field.

1.1 Research Objectives

1.1.1 General Objective

- To assess the potential of using hyperspectral and multispectral remote sensing for identifying lava surface morphology in the Krafla lava fields from 1984

1.1.2 Specific Objectives

- To identify lava surface morphology in Krafla using SPOT 5 multispectral and panchromatic data.
- To identify lava surface morphology in Krafla using EO-1 Hyperion and Landsat 8 OLI data.
- To classify and map the identified lava surface morphology using EO-1 Hyperion and Landsat 8 OLI data and SPOT 5 data.
- To assess the accuracy of the lava morphological map with reference to aerial photographs and existent maps.

1.1.3 Research Questions

- How can we identify lava surface morphology using combination SPOT 5 multispectral and panchromatic data?
- How can we identify lava surface morphology from EO-1 Hyperion and Landsat 8 OLI data?
- How to make detailed classification and map of identified lava surface morphology using EO-1 Hyperion and Landsat 8 OLI data and SPOT 5 data?
- How accurate is the method of the detailed lava surface morphology map produced by EO-1 Hyperion and Landsat 8 OLI data and SPOT 5 data?

1.1.4 Hypotheses

- Lava histogram/pixels distribution in the SPOT 5 scene can be used to identify characteristic lava morphology.
- Spectral reflectance in Landsat 8 OLI and EO-1 Hyperion scenes can be used to identify characteristic of lava surface morphology.
- It is possible to classify and map the details lava morphology by using maximum likelihood classification and spectral angle mapper.
- A certain degree of accuracy can be achieved from details lava surface morphology map that produced by SPOT 5, Landsat 8 OLI and EO-1 Hyperion compared to the existing lava morphology map and aerial photograph.

2 Literature Review

2.1 Lava Morphology

Lava morphology is related to the characteristics of the surface morphology of a lava flow after solidification (Murcia et al., 2014). Morphology of lava is the primary basis for classification of lava flows when rheological properties cannot be directly observed during emplacement (Kilburn, 2000). According to Kilburn (2000), solidified lava flows are grouped as pahoehoe (surface is smooth and continuous), aa (surface is rough and fragmented), and blocky (surface is brecciated). Furthermore, a transition surface morphology between aa and pahoehoe has been described as rough, spiny, slabby, ripply and grooved, among others (Rossi, 1997; Kilburn, 2000; Hon et al., 2008). Most basaltic lavas can be identified by the terms pahoehoe, aa, or block lava (Fig. 5) (Wohletz & Heiken, 1992).

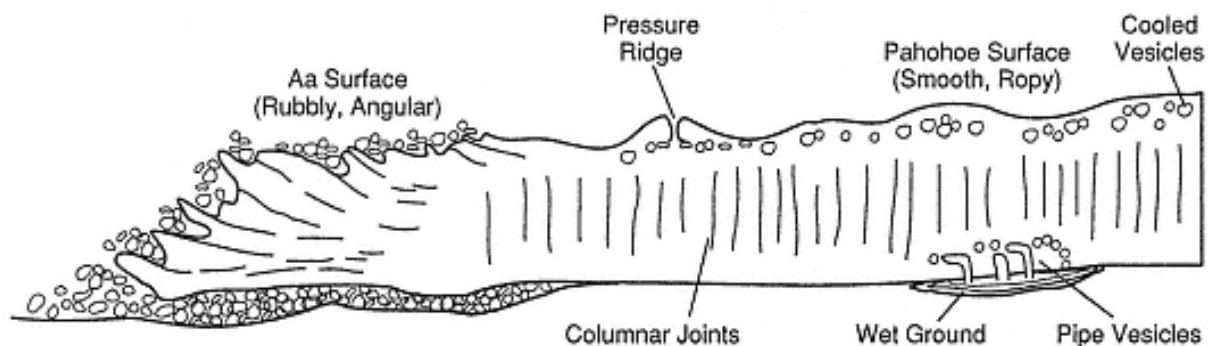


Fig. 5 Cross section of a generic basaltic lava flow, showing some of the basic structural features that should be described when mapping flows. Flow surfaces, if preserved, presents variety of textures that range from smooth, ropy pahoehoe to spiny, rubbly aa lavas (Wohletz & Heiken, 1992).

These transitional lava flows are commonly known as fine-aa, semi-hoe or toothpaste lava (Murcia et al., 2014). These distinct terms used to describe lava surface morphology are also known as facies or archetypes (Rossi, 1997) and provide a good first-order approach to understanding lava flow emplacement style and rheology (Kilburn, 2000). Aa and pahoehoe flows can be found on all of the volcanoes of the Big Island, Hawaii (Hon et al., 2008). In general, there seems to be trends to higher percentage of pahoehoe on the younger volcanoes (Hon et al., 2008). Pahoehoe lava has a fairly smooth surface as opposed to aa which is very rough (Fig. 6 and 7).

Pahoehoe Lava

The most common transitional pahoehoe types are slabby pahoehoe and spiny pahoehoe. Slabby pahoehoe flows are easily distinguished by their upturned slabs of pahoehoe crust (Hon et al., 2008). Whereas each of the individual crustal plates have a smooth pahoehoe crust, the random jumbled orientation of these plates gives the flows a very rough and jagged appearance (Fig. 6e and 7e) (Rossi, 1997, Hon et al., 2008; Murcia et al., 2014; Pedersen et al., 2015). This crustal texture requires relatively high strain rates in order to tear the crust into plates and to tilt and overturn the individual plates. Slabby pahoehoe lava is characterized by a flow top of crustal slabs and a pahoehoe base (Hon et al., 2008). The slabs are up to

several meters across and a few centimeters to decimeters thick (Hon et al., 2008; Murcia et al., 2014). This morphology is produced when pulses of lava disrupt and break up incipient pahoehoe crust, forming slabs that are rafted and pile up. Slabby pahoehoe forms when relatively fast moving pahoehoe flows become more viscous, allowing the molten lava to grab and rip the pahoehoe crust into chunks (Hon et al., 2008).

Spiny pahoehoe flows are covered by a rough spiny surface different from the smooth shiny surface of normal pahoehoe (Hon et al., 2008; Pedersen et al., 2015). Spiny pahoehoe flows commonly form as the last oozes out of dying pahoehoe flows or stagnating lobes of pahoehoe flows (Hon et al., 2008). Spiny pahoehoe also leaks from the edges and the fronts of some aa flows (Hon et al., 2008). Spiny pahoehoe flows have toes and ropes that appear similar to normal pahoehoe in general shape and continuity of the crust (Hon et al., 2008) (Fig. 6b and 7b).

Shelly pahoehoe is a very vesicular pahoehoe lava type with fragile lava crust (Murcia et al., 2014). It forms flow lobes and small lava tubes which become hollow inside as lava drains downslope or as the molten lava in the lobe-interior loses gas (Fig. 6a and 7a) (Rossi, 1997). Slightly buckled lava crusts and small lava channels up to a few meters in width are common on shelly-type lava flows. This morphology reflects mainly ponded or very slowly moving lavas. Lava up to hundreds of meters in diameter was pooled while a crust formed. Input of new lava, caused inflation and likely cracking of the solidified crust (Murcia et al., 2014). Subsequent outflow beneath the crust caused subsidence, generating the broad undulating surface and jigsaw jointed slabs that are piled up in some places. Lava was likely ponded temporarily in these proximal areas due to the damming caused by the build-up of outer fronts associated with the very flat topography (Murcia et al., 2014).

Rubbly pahoehoe lava is a flow characterized by a flow top of pahoehoe crustal rubble and a pahoehoe base (Pedersen et al., 2015). The crustal rubble is up to several decimeters in size and has previously been suggested to form when pulses of lava disrupt the mature crust of a pahoehoe flow, that is brecciated and the transported on top of the flow (Pedersen et al., 2015)

Aa Lava

Aa lavas have brecciated flow tops and bases (Pedersen et al., 2015). The breccia consists of jumbles of blocky lava and irregular shaped-clinker formed by viscous tearing of the chilled lava crust, which subsequently is rafted towards the flow front where it is dislodged from the front in caterpillar-track motion (Pedersen et al., 2015).

Rubbly aa is characterized with a clinkery and blocky surface (Rossi, 1997; Murcia et al., 2014) (Fig. 6c and 7c). Surface breccia varies from sand size to blocks several meters in diameter). Clasts are often slightly rounded due to attrition between the clasts during flow. This lava type has high thermal maturity; the crust during flow is broken by brittle failure (Rossi, 1997).

Cauliflower aa is caused by Irregular protrusions which resemble cauliflowers occur on the lava surface (Fig. 6d and 7d). This is an initial aa lava type in the transformation from pahoehoe to rubbly aa. Protrusions are initially attached to the massive lava beneath but commonly break and form loose debris on the flow surface (Rossi, 1997). Overall cauliflower aa is characterized as broad, smoothly undulating zones with typically clinkery surfaces.

Cauliflower aa is common in the shelly and slabby pahoehoe dominated zones where lava flows spilled out after the formation of these morphology (Murcia et al., 2014).

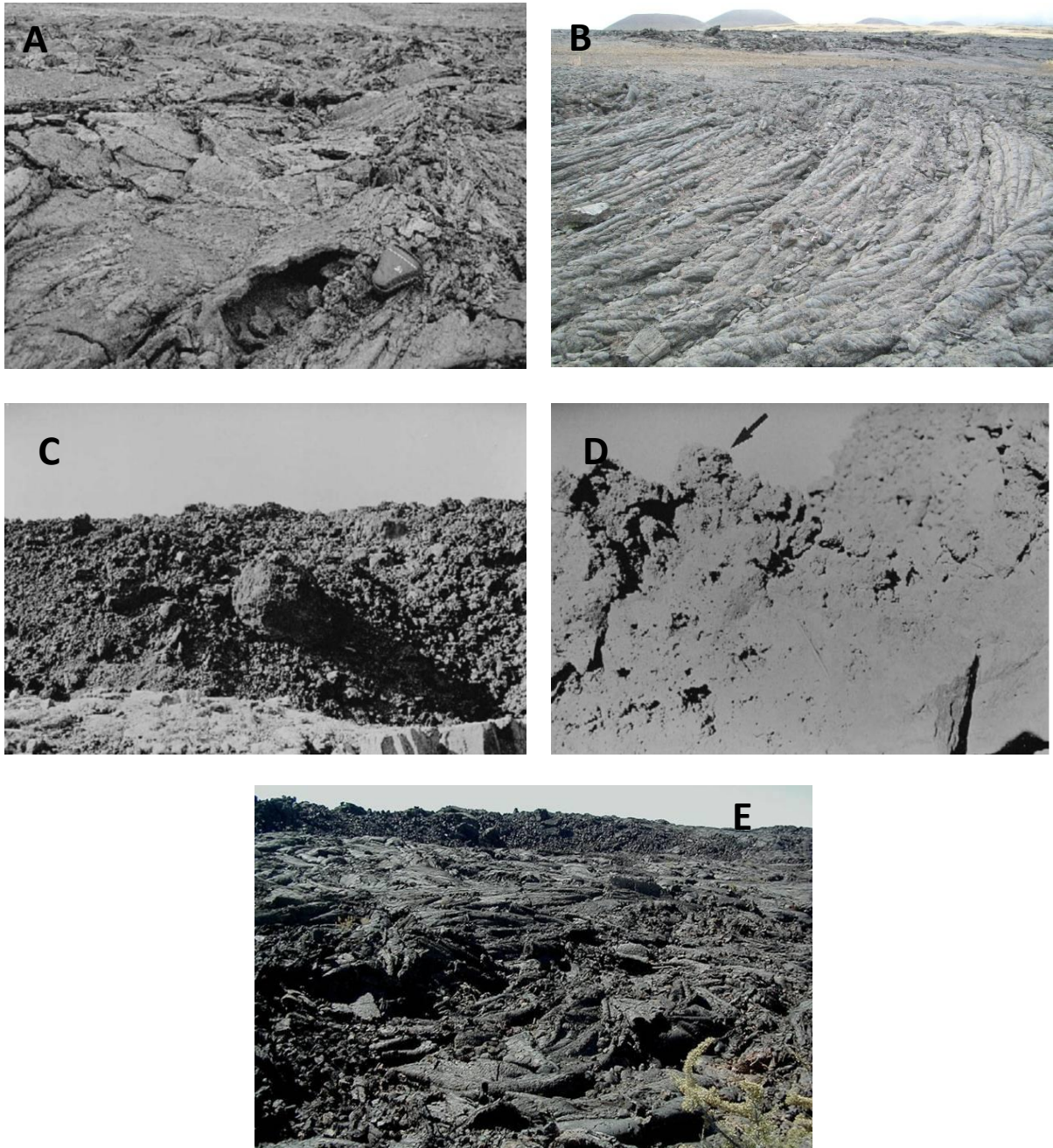


Fig. 6 Lava morphology from Krafla lava field and Craters of the moon Lava field (a) Shelly Pahoehoe lava in Krafla; (b) Spinny pahoehoe lava in Craters of the moon (c) Rubbly Aa lava in Krafla; (d) Cauliflower Aa in Krafla; and (e) Slabby pahoehoe lava in Craters of the moon (John, n.d.; Rossi, 1997)

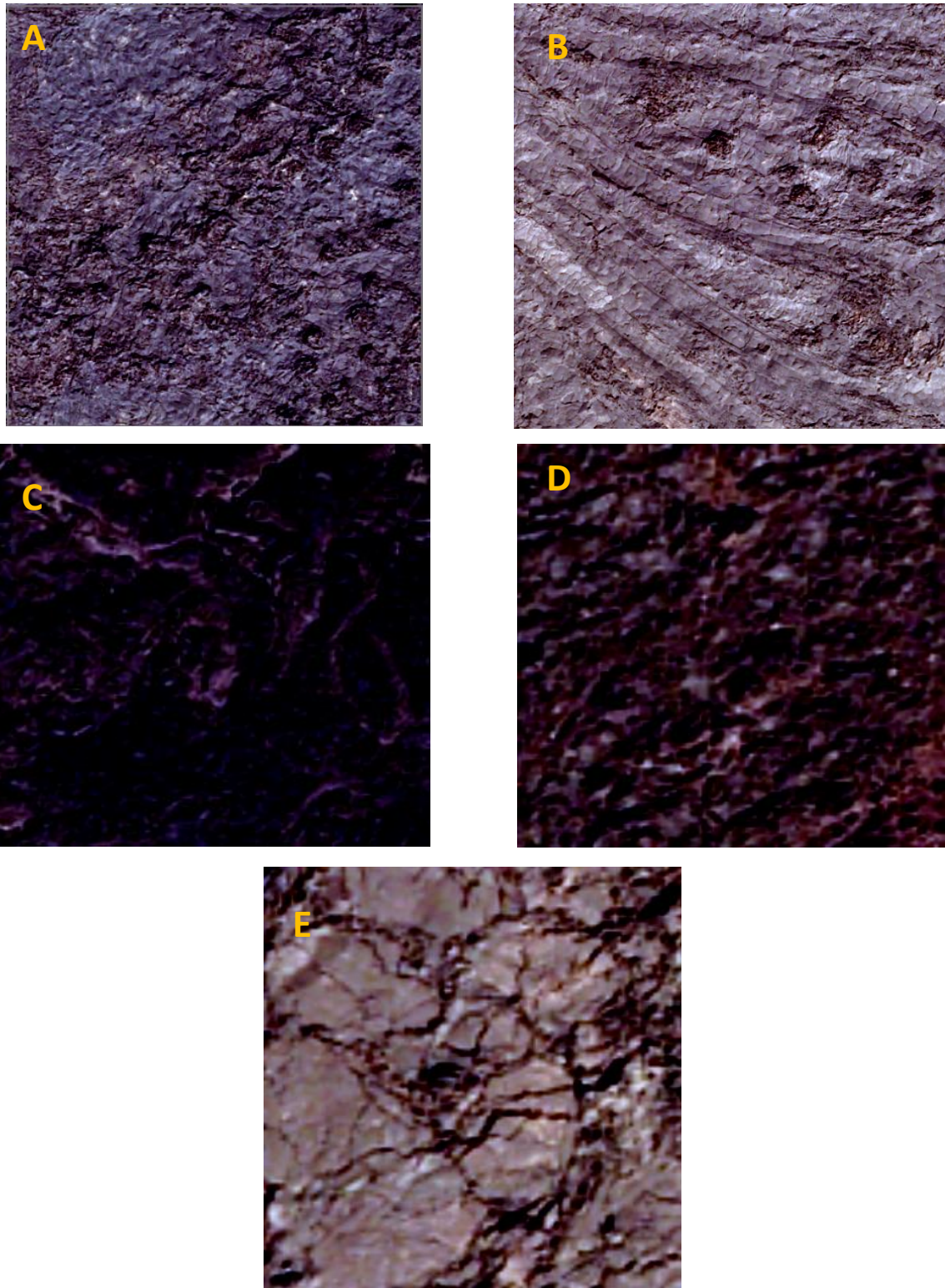


Fig. 7 Lava morphology from Krafla lava field base on aerial photograph (a) Shelly Pahoehoe lava; (b) Spinny pahoehoe lava; (c) Rubbly Aa lava; (d) Cauliflower Aa; and (e) Slabby pahoehoe.

2.2 Remote Sensing

Remote Sensing is the science of deriving information about objects on the Earth's surface from images using a wide range of the electromagnetic (EM) spectrum (Fig. 8). This technology has been rapidly increasing during the past decades. Based on diverse portions of the spectrum, it can be classified into: gamma rays, X-rays, UV radiation, visible radiation (light), infrared radiation, microwaves, and radio waves. Each of these named portions represents a range of wavelengths, not one specific wavelength (Bakx et al, 2012).

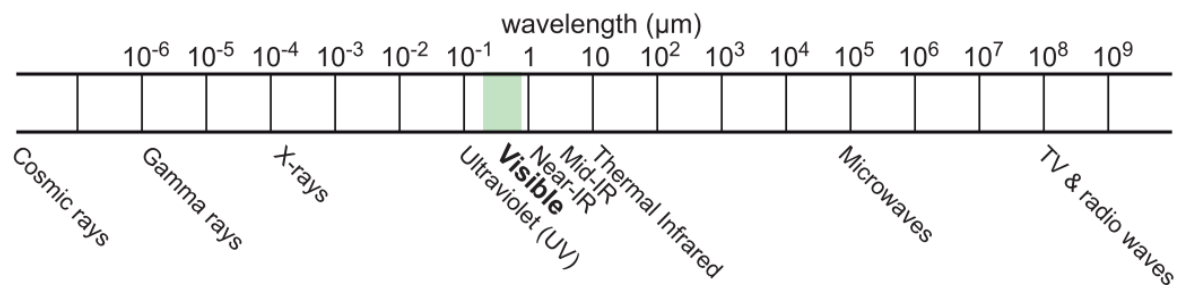


Fig. 8 The classification of EM spectrum (Bakx et al., 2012).

2.3 Sensor and Satellite

A sensor is a device which records the amount of EM energy striking it in a particular wavelength range (Timmermans, 1995). There are two types of sensors, active and passive ones. Active sensors provide their own source of illumination to make the energy for example radar, while passive sensors use external sources (in many cases the sun) for example earth resources satellites. A further division can be made looking at from where the remote sensing takes place. This can be done from following platforms:

- Ground platforms (Spectrometer)
- Airborne platforms (helicopters, aircraft)
- Spaceborne platforms (satellites)

This study is focus in spaceborne platform. Spaceborne sensors or satellites are frequently used in mineral exploration, monitoring volcano, crop forecasting etc. According to Timmermans (1995) there are five main types of satellites that can be distinguished :

- Photographic system. Aerial photography which is the oldest source of aerospace imagery. This taken in the visible part of the electromagnetic spectrum, and the range between 0.3 to 1.1 μm.
- System sensing the reflected radiation by the earth. These systems that work during daytime record the reflectance in a digital format. This can be done in one particular wavelength range, but also in different spectral ranges and so called multispectral scanner system.
- System sensing the emitted radiation from the earth. These systems record continuously the longwave radiation emitted by the earth's surface and the atmosphere, in a digital format.

- Active radar systems. The backscatter of radiation pulses emitted from an aircraft or satellite is recorded in a digital format.
- Passive radar systems. The emission in the microwave range can also be recorded by the satellites.

In this study the focus will be set on multispectral (Landsat 8 OLI) and hyperspectral (EO-1 Hyperion) sensors which are operating in optical spectrum.

2.3.1 Landsat 8 OLI

Landsat-8 was launched by the National Aeronautics and Space Administration (NASA) on 11 February 2013 from Vandenberg Air Force Base in California, USA (Bhardwaj et al., 2015). It is an American Earth observation satellite and the eighth satellite in the Landsat program. Landsat- 8 joins Landsat-7 on-orbit, providing increased coverage of the Earth's surface. It is in the form of free-flyer spacecraft carrying two sensors onboard: the Operational Land Imager (OLI) and the Thermal Infrared Sensor (TIRS). These two instruments collect image data for nine visible, near-infrared, shortwave infrared bands and two longwave thermal bands (Bhardwaj et al., 2015). The two sensors are better than its predecessors in all three resolutions, i.e., spatial (for thermal band), spectral (inclusion of three new narrower bands) and radiometric resolution. Adding to the legacy of multispectral and panchromatic (PAN) bands, the OLI is also equipped with two new spectral bands: band 1 (coastal/aerosol) and band 9 (cirrus cloud) (<http://landsat.gsfc.nasa.gov>).

According to USGS (n.d.) Landsat 8 Operational Land Imager (OLI) and Thermal Infrared Sensor (TIRS) images consist of nine spectral bands with a spatial resolution of 30 meters for Bands 1 to 7 and 9. New band 1 (ultra-blue) is useful for coastal and aerosol studies. New band 9 is useful for cirrus cloud detection. The resolution for Band 8 (panchromatic) is 15 meters. Thermal bands 10 and 11 are useful in providing more accurate surface temperatures and are collected at 100 meters. Approximate scene size is 170 km north-south by 183 km east-west (106 mi by 114 mi). Detail spectral bands on Landsat 8 show in the Table 1.

Unlike a single wide bandwidth thermal data collection in its predecessors (Landsat 4–7), the TIRS collects temperature information in two more narrow spectral bands with better spatial resolution than the Landsat TM TIR band. The radiometric resolution (acquisition at 12 bits and dispensing at 16 bits) is another significant development over traditional Landsat data (8 bit). They have high signal to noise ratio (SNR) radiometer performance, enabling 12-bit quantization of data allowing for more bits for better land-cover characterization. Landsat-8 provides moderate-resolution imagery, from 15 meters to 100 meters of Earth's surface and Polar Regions (Pour, 2014). Landsat-8 data have been distributed to the general public on non-discriminatory basis at no cost to the user. The data can be easily downloaded from the (<http://earthexplorer.usgs.gov> and <http://glovis.usgs.gov/>) online linkages.

Table 1. Characteristic of spectral band of Landsat 8 (USGS, n.d.-b).

Bands	Wavelength (micrometers)	Resolution (meters)
Band 1 - Coastal aerosol	0.43 - 0.45	30
Band 2 – Blue	0.45 - 0.51	30
Band 3 – Green	0.53 - 0.59	30
Band 4 – Red	0.64 - 0.67	30
Band 5 - Near Infrared (NIR)	0.85 - 0.88	30
Band 6 - SWIR 1	1.57 - 1.65	30
Band 7 - SWIR 2	2.11 - 2.29	30
Band 8 - Panchromatic	0.50 - 0.68	15
Band 9 – Cirrus	1.36 - 1.38	30
Band 10 - Thermal Infrared (TIRS) 1	10.60 - 11.19	100 * (30)
Band 11 - Thermal Infrared (TIRS) 2	11.50 - 12.51	100 * (30)

2.3.2 EO-1 Hyperion

Hyperion is a hyperspectral imaging radiometer, on board the EO-1 satellite, which was launched in the year 2000 in a polar orbit at 705 km altitude and with a 16-day repeat cycle (<http://eo1.gsfc.nasa.gov/miscPages/home.html>). The Hyperion imaging spectrometer collects radiation in 220 spectral channels ranging from 357 to 2576 nm with a 10 nm bandwidth. The instrument operates in a spatial resolution of 30 m (Spinetti et al., 2009). According to Beck (2003) the Level 1 Radiometric of Hyperion product has a total of 242 bands but only 198 bands are calibrated. Because of an overlap between the VNIR and SWIR focal planes, there are only 196 unique channels. Calibrated channels are 8-57 for the VNIR, and 77-224 for the SWIR. The reason for not calibrating all 242 channels is mainly due to the detectors' low responsivity. The bands that are not calibrated are set to zero in those channels (Table A1).

2.3.3 SPOT 5

SPOT 5 was launched on May 4, 2002 and has two high resolution geometrical (HRG) instruments that were deduced from the HRVIR of SPOT 4. They offer a higher resolution of 2.5 to 5 meters in panchromatic mode and 10 meters in multispectral mode (20 meter on short wave infrared 1.58 – 1.75 μm). The spectral band in the short wave infrared band (essential for vegetation data) is maintained at a resolution of 20 m due to limitations imposed by the geometry of the CCD sensors used in this band. SPOT 5 also features an HRS imaging instrument operating in panchromatic mode. SPOT 5 panchromatic offers high-spatial resolution (2.5 m) to obtain much more detailed information in order to improve the lava texture mapping. Information extracted from the conventional pixel-based approach does not provide sufficient detail for geologic mapping (Kassouk et al., 2014). This technique only uses grey values of individual pixels. Recognition of geologic objects and landforms requires an analysis of grey values in large areas along with contextual information (e.g. a DEM,

textural values, and size and shape) (Kassouk et al., 2014). The challenge is to divide the image into specific regions, which contain homogeneous pixels. The homogeneity can stem, for example, from similar brightness or color, roughness and texture (Kassouk et al., 2014).

2.4 Spectral Reflectance

The EM radiation will interact to earth's surface and when energy is incident on a certain earth feature there are three fundamental energy interactions possible with that surface. Those three energy interaction are (1) reflected; (2) absorbed; and (3) transmitted (Fig. 9).

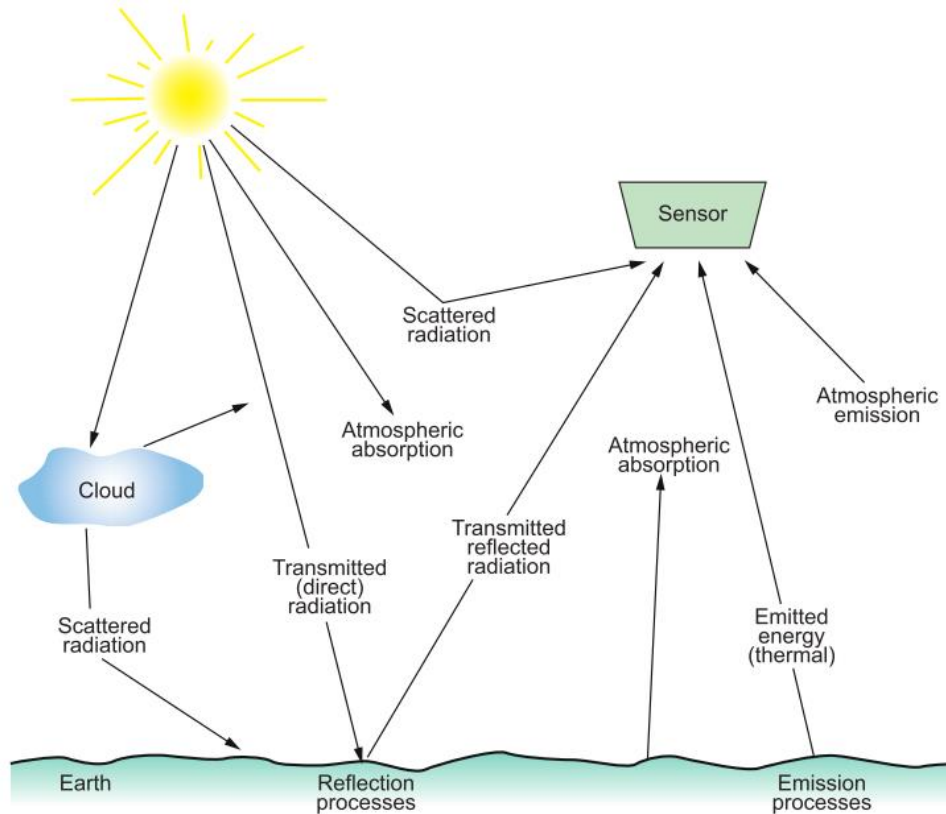


Fig. 9 Interactions of EM radiation with the atmosphere and the Earth's surface. (Bakx et al., 2012).

The proportions depend on the wavelength:

$$Ei(\lambda) = Er(\lambda) + Ea(\lambda) + Et(\lambda) \quad (1)$$

$Ei(\lambda)$ = The incident energy

$Er(\lambda)$ = The reflected energy

$Ea(\lambda)$ = The absorbed energy

$Et(\lambda)$ = The transmitted energy

The amount of energy being reflected, absorbed or transmitted will vary for different objects depending on the type and condition of the material. The dependency on the wavelength means that even within a given feature the distribution of reflected absorbed or transmitted energy will vary with different wavelengths. Due to these reasons, two objects may be indistinguishable from each other in one spectral region and be easily discriminated between in another spectral region. In the visible part of the EM spectrum, these spectral differences result in the phenomenon “color”. An object is called “blue” when it mainly reflects in the blue part of the visible region of the spectrum, “green” when reflection is dominant in the green part of the spectrum (Timmermans, 1995).

In this study the reflectance properties are very important. This property depends mainly on the surface roughness of the object compared with the wavelength of the EM radiation incident on the object. According to Bakx et al (2012) there are two type of reflection (1) specular reflection; and (2) diffuse reflection (Fig. 10).

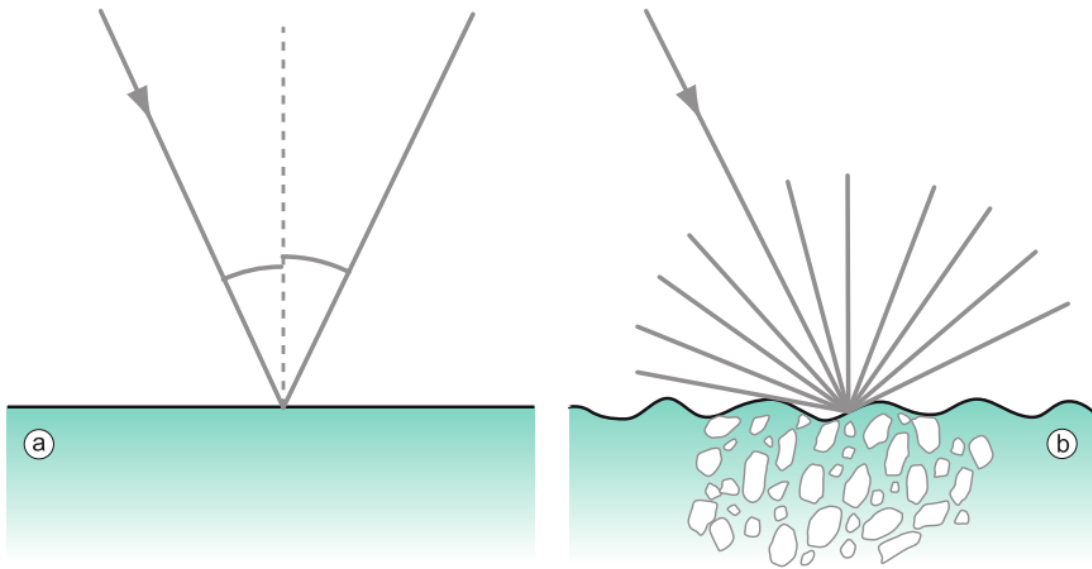


Fig. 10 Schematic diagrams showing (a) specular and (b) diffuse reflection (Bakx et al., 2012).

Specular reflection occurs when a surface is smooth and (almost) all of the radiation is directed away from the surface in a single direction. Specular reflection can take place, for example, for a water surface or a glasshouse roof. It results in a very bright spot (also called “hot spot”) in the sensed image. Meanwhile diffuse reflection occurs in the rough surface and the radiation is reflected almost uniformly in all directions (Timmermans, 1995; Bakx et al., 2012). The percentage of incident energy that is reflected back toward space can be explained in a formula:

$$\rho_{\lambda} = \frac{Er(\lambda)}{Ei(\lambda)} \quad (2)$$

Where ρ_{λ} is spectral reflectance. A graph of spectral reflectance of an object as a function of wavelength is called spectral reflectance curve.

2.4.1 Lava Spectral Reflectance Curves

Van Der Meer (2006) explains that spectral reflectance curves are often determined by the mineralogy. These absorption features are controlled by the particular crystal structure in which the absorbing species is contained and by the chemical structure of the mineral (Van Der Meer, 2006). Furthermore, according to Robertson et al (2013) spectral reflectance curves of basalt can be strongly affected by even thin coatings of silica and factors such as rind thickness, water-to-rock ratio, associated minerals, and texture/morphology may contain information about environmental formation conditions, and such factors may manifest themselves in visible-near infrared (VNIR) and thermal infrared (TIR) spectra. It is essential to know relations between lava surface morphology and spectral reflectance curves.

Michalski et al (2006) present the results of a lab spectroscopic study of weathered and fresh basalts from the Columbia River Basalt Group (CRBG) in Washington, using both VNIR and thermal emission wavelength. Spectra of fresh CRBG rock surfaces have five major absorptions at 1) 0.7–1 μm , 2) 1.05 μm , 3) 1.41 μm , 4) 1.91 μm , and 5) 2.32 μm (Fig. 11), corresponding to a) Fe^{3+} electronic absorptions in oxides/ hydroxides, b) Fe^{2+} electronic absorptions in pyroxene, c) O–H vibrations in hydroxyl, d) H_2O vibrations in mineralogy water (water absorptions), and e) M–OH vibrations in clay minerals (M=metals, Fe^{2+} or Mg^{2+} in their case) (Michalski et al., 2006). In general the Fe^{3+} absorption at short wavelengths is weak in fresh surfaces (Michalski et al., 2006).

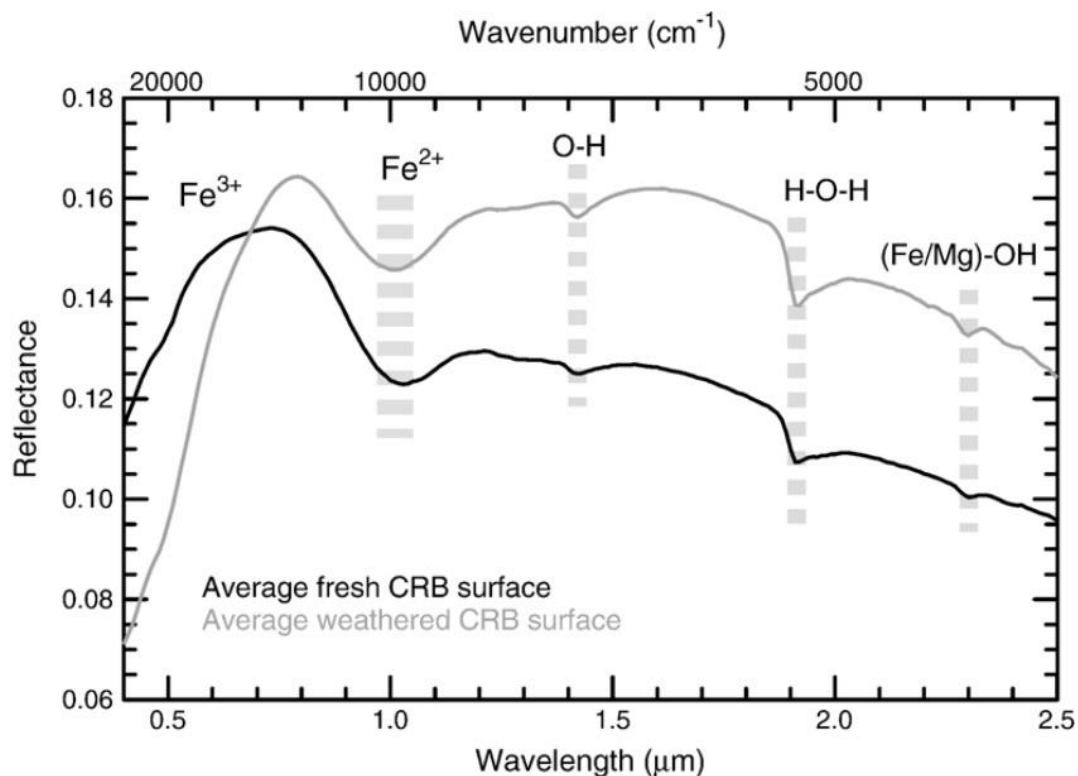


Fig. 11 Average VNIR spectra of fresh and weathered surfaces of CRBG samples, five absorptions are shown (Michalski et al., 2006).

Spinetti et al (2009) presented average spectral curves of different volcanic materials in Mt. Etna (including tephra) based on spectral ground measurement (Fig. 12), their results show

air-fall deposits are characterized by low reflectance values and distinguish them from other surface materials. Meanwhile old lava flows show the highest reflectance values due to weathering and vegetation cover (Spinetti et al., 2009). Lava spectral reflectance and textural features can be identified depending on the capabilities of the remote sensing instrument (Spinetti et al., 2009).

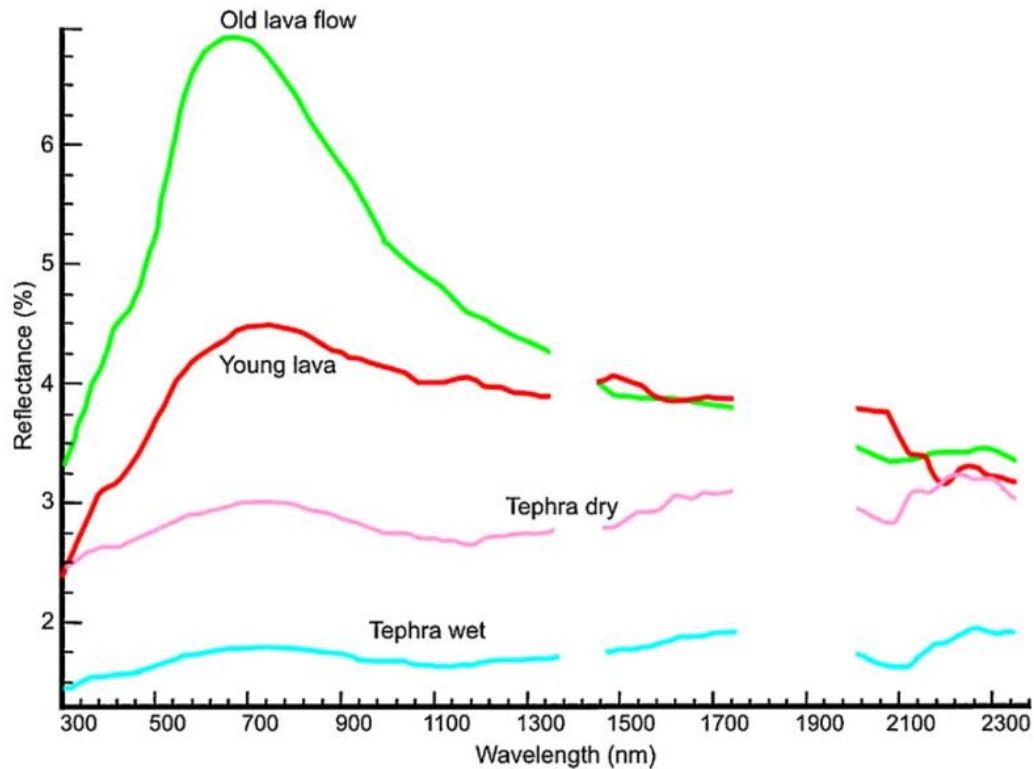


Fig. 12 Average spectral signature for different type of lava from Mt. Etna (Spinetti et al., 2009).

Byrnes et al. (2004) investigated surface units in the Mauna Ulu flow field, through field and remote sensing analyses using ASTER & MASTER datasets (Fig. 13). They found that mean spectral reflectance curves allow characterization of lava surface morphology, but using individual data pixels from those satellites give an insufficient resolution to identify typical individual lava flow units using endmember spectra. Mean reflectance curves show that pahoehoe has higher reflectance than aa (Fig.13). These reflectance and absorption characteristics from different satellites images (e.g SPOT 5, Landsat 8 OLI and EO-1 Hyperion) could be used for identify and assess lava surface morphology.

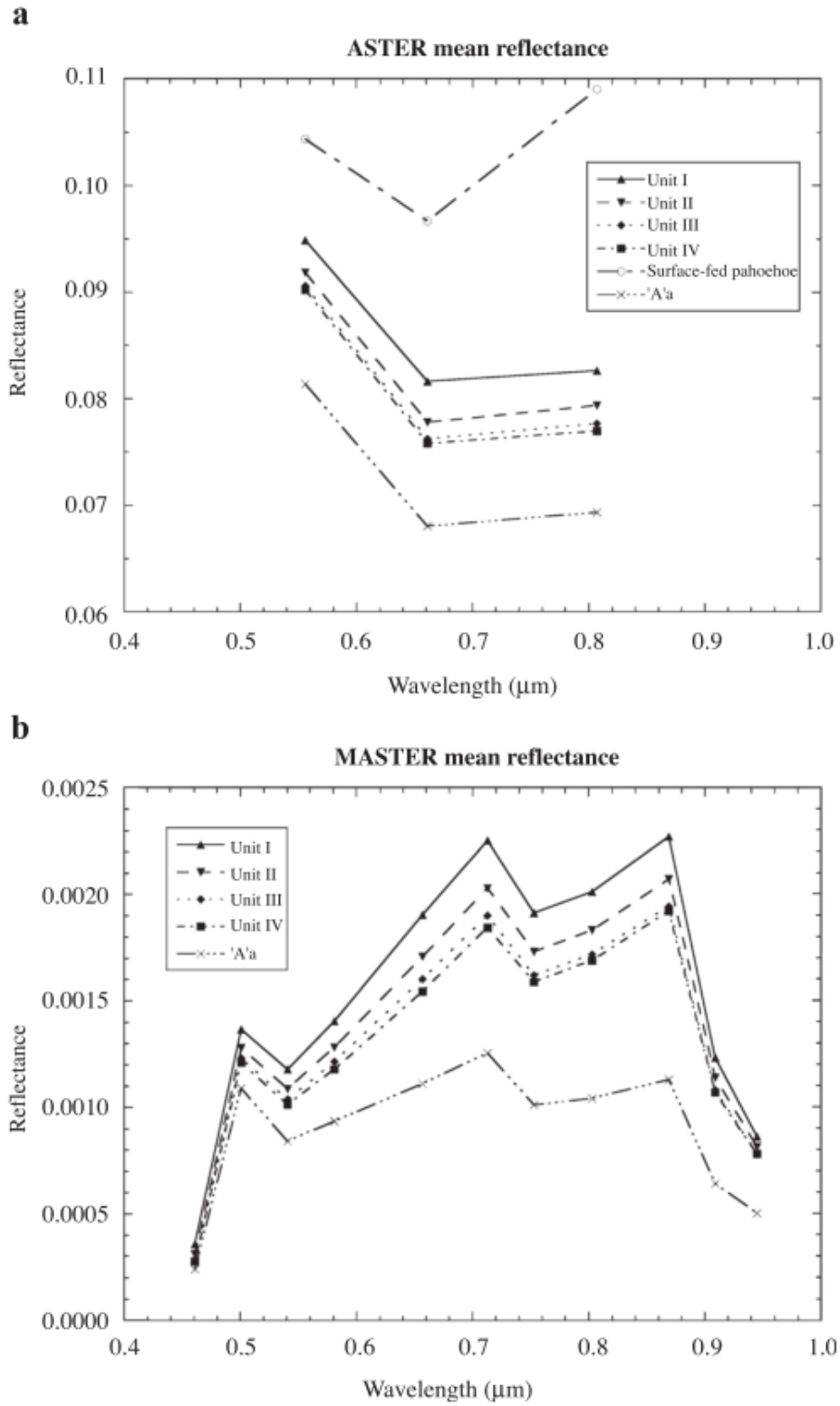


Fig. 13 Mean reflectance spectra for Mauna Ulu surface units, derived from (a) ASTER, bands 1 to 3, and (b) MASTER, bands 1 to 11 (Byrnes et al., 2004).

3 Study Area

3.1 Iceland's Volcanic Zone

Due to its situation at the Mid-Atlantic Ridge and the Greenland–Iceland–Faeroe Ridge, and above a mantle plume, Iceland has high levels of volcanic activity (Fig. 14). This fact together with the country's northern location, has led to the country's image as “Land of Fire and Ice”. The Mid-Atlantic Ridge is the divergent plate boundary of the Eurasian-African and North and South American plates, and is spreading at an average rate of approximately 2 cm per year. The Iceland Basalt Plateau rises more than 3000 m above the surrounding sea floor, has crustal thickness of 10–40 km and covers about 350,000 km² (Thordarson & Larsen, 2007; Thordarson & Höskuldsson, 2008).

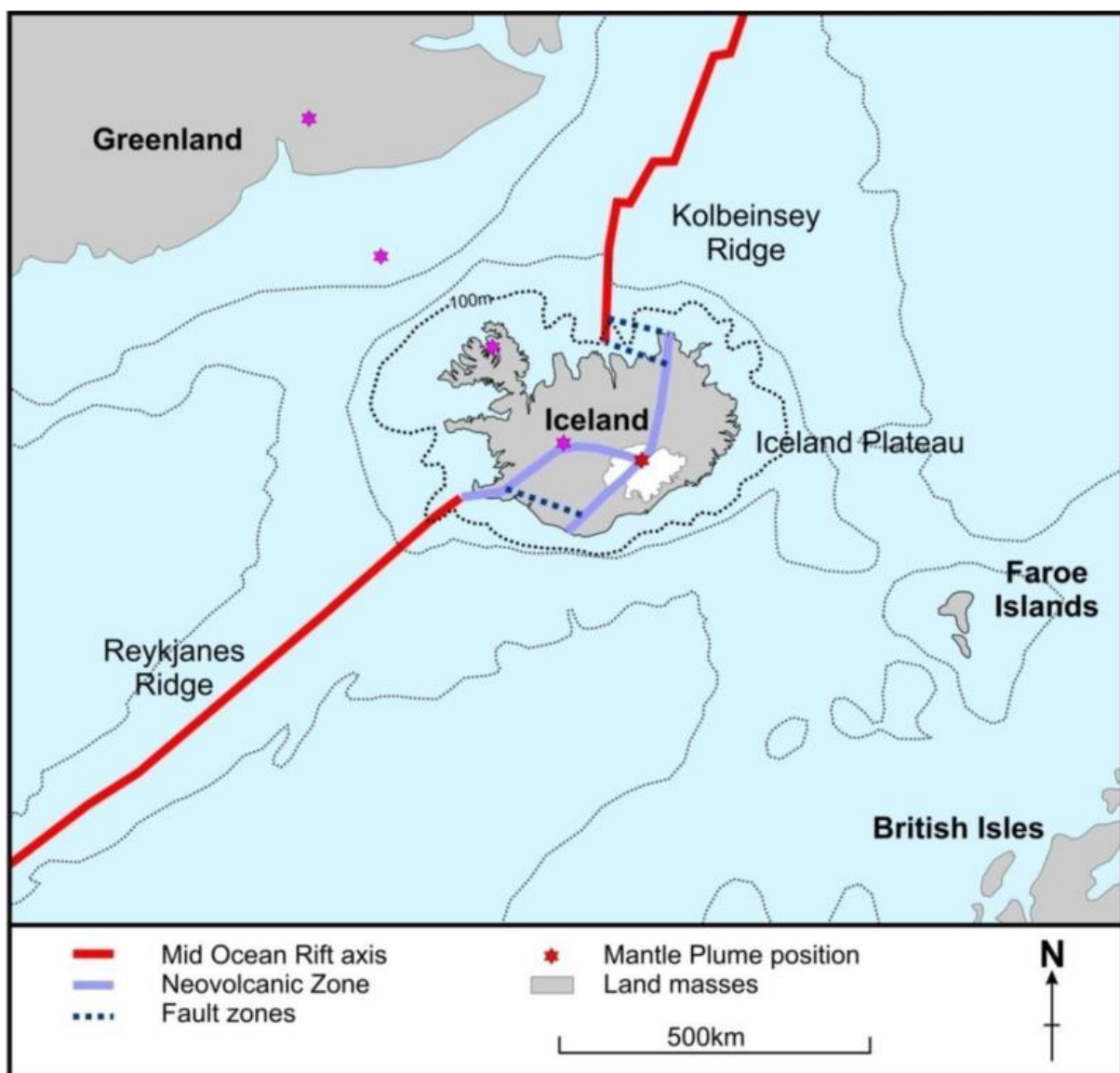


Fig. 14 Iceland situation in the North Atlantic Ocean, at the junction of the Reykjanes and Kolbeinsey Ridges. The Iceland Basalt Plateau is marked by the darker dotted line around Iceland, and the present location of the mantle plume is marked by the red star. The purple stars show the previous locations of the mantle plume (Thordarson & Larsen, 2007, modified by Andrew, 2008).

Active volcanism in Iceland is primarily constrained to the area known as the Neovolcanic Zone, defined as that part of Iceland containing rocks belonging to the Brunhes magnetic epoch ($<0.8\text{Ma}$) (Andrew, 2008). The Neovolcanic Zone contains of three subzones: the North Volcanic Zone (NVZ), the West Volcanic Zone (WVZ), and the East Volcanic Zone (EVZ) (Fig. 15).

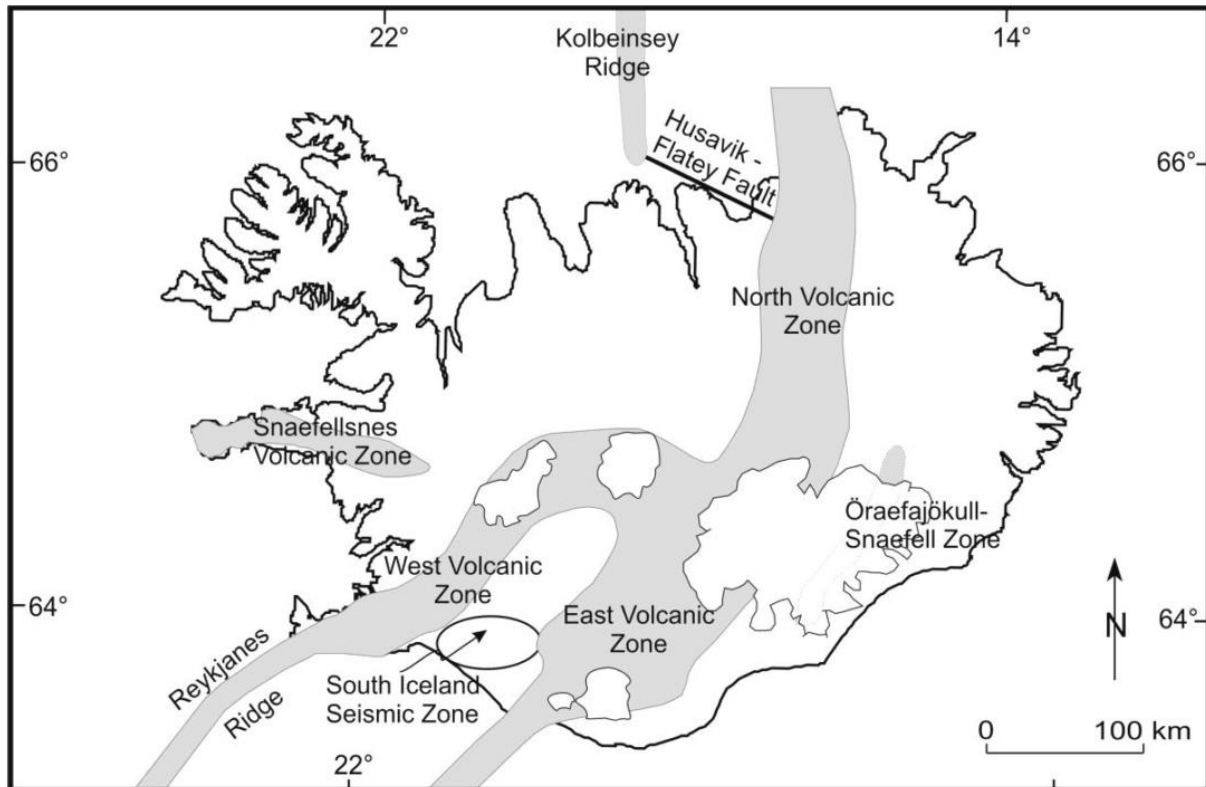


Fig. 15 Map presenting Iceland's Neovolcanic Zone at the junction of the Reykjanes and Kolbeinsey Ridges to the south and north respectively. The Snaefellsnes and Öraefajökull Flank Zones are also shown, as well as the South Iceland Seismic Zone. The latitude and longitude are indicated (Thordarson & Höskuldsson, 2008, modified by Andrew, 2008).

Volcanism surrounding the Neovolcanic Zone is primarily concentrated in volcanic systems and these are the main geological features in Iceland. There are 30 volcanic systems, distributed evenly throughout the Neovolcanic Zone (Table 2). Twenty of the 30 volcanic systems feature a fissure swarm (Andrew, 2008). According to Thordarson & Larsen (2007), 12 of those are well developed and mature swarms, 5 are of moderate maturity and 4 can be regarded as embryonic (Table 2). The mature and moderately mature fissure swarms are distinct narrow and elongated strips (5–20 km wide and 50–200 km long) with a high density of tensional cracks, normal faults and volcanic fissures, whereas embryonic swarms feature one or a few discrete volcanic fissures. The spreading and subsequent rifting of the crust that occurs at the plate boundary is not a continuous process, in either time or space. It occurs in different rifting episodes that most commonly are narrowed to a single volcanic system at any one time, although near-concurrent activity on two or more system is known to have occurred (Thordarson & Larsen, 2007 ; Thordarson & Höskuldsson, 2008; Andrew, 2008). Usually the entire system is activated in these episodes that can last for several years to decades and the tradition is to refer to such events as 'Fires'; for example the "Krafla Fires". These episodes

typically frequent earthquake swarms and volcanic eruptions within the central volcano and on the fissure swarm (Thordarson & Larsen, 2007).

Table 2. Volcanic systems in Iceland. Modified from Thordarson and Larsen (2007).

	Volcanic Zone	Name	Max. elev (masl)*a	Area (km ²)	Fissure swarm *b	Central Volcano	Name of Central Volcano
1	RVZ	Reykjanes	163	350	xxx	d	
2	RVZ	Krysuvik	393	300	xxx	d	
3	RVZ	Brennisteinsfjoll	621	280	xxx	d	
4	WVZ	Hengill	803	370	xxx	cv	Hengill
5	WVZ	Hromundartindur	283	25		d	
6	WVZ	Grimsnes	214	100	xx	d	
7	WVZ	Geysir *c	600	25		d	
8	WVZ	Prestahnjukur	1400	950	xxx	cv	Prestahnjukur
9	WVZ	Hveravellir	1000	720	xx	cv	Hveravellir
10	MIB	Hofsjokull	1800	2200	xxx	cv	Hofsjokull
11	MIB	Tungnafellsjokull	1520	530	xx	cv	Tungnafellsjokull
12	EVZ	Vestmannaeyjar	283	<480	xx	d	
13	EVZ	Eyjafjallajokul	1666	300		cv	Eyjafjallajokul
14	EVZ	Katla	1480	1300	x	cv	Myrdalsjokull
15	EVZ	Tindfjoll *c	1462	230		cv	Tindfjoll
16	EVZ	Hekla – Vatnafjoll	1491	720	xx	cv	Hekla
17	EVZ	Torfajokull	1278	900		cv	Torfajokull
18	EVZ	Bardarbunga	2009	2500	xxx	cv	Bardarbunga
19	EVZ	Grimsvotn	1722	1350	x	cv	Grimsvotn
20	NVZ	Kverkfjoll	1934	1600	xxx	cv	Kverkfjoll
21	NVZ	Askja	1510	2300	xxx	cv	Askja
22	NVZ	Fremrinamur	800	1200	xxx	d	
23	NVZ	Krafla	818	900	xxx	cv	Krafla
24	NVZ	Theistareykir	600	650	xxx	d	
25	OVB	Oraefajokull	2110	250		cv	Oraefajokull
26	OVB	Esjufjoll *d	1760	400		cv	Snaehetta
27	OVB	Snaefell *d	1833	170		cv	Snaefell
28	SVB	Ljosufjoll	1063	720	x	d	
29	SVB	Helgrindur	647	220	x	d	
30	SVB	Snaefellsjokull	1446	470		cv	Snaefellsjokull

Notes:

a. Maximum elevation above sea level.

b. xxx, mature; xx, moderate maturity; x, embryonic.

c. cv, central volcano; d, domain.

d. No verified eruption of Holocene age.

3.2 North Volcanic Zone

The Krafla volcanic system is a part of the Icelandic Northern Volcanic Zone (NVZ), that is about 200 km long part of the Mid-Atlantic Ridge boundary and extends northwards from the Vatnajökull glacier to the northern coast of Iceland (Fig. 16). In the southern part, the plate boundary continues underneath the glacier and continues southwards as the EVZ. In the north part, the NVZ is linked with the offshore Kolbeinsey Ridge by the Tjörnes Fracture Zone, which consists of the Dalvík, Húsavík and Grímsey strike-slip faulted areas (Hjartardóttir, 2013).

The NVZ has a North-South orientation and is mostly dominated by large swarms of faults and fissures which pass through a central volcano forming together a volcanic system. Volcanic fissure eruptions and silicic eruptions concentrate in the central volcanoes (Grönvold, 2008.; Hjartardóttir et al., 2012). There are two central volcanoes in NVZ, those are Krafla and Askja. A low, broad shield about 25 km in diameter forms the Krafla central volcano with a caldera in its center (Grönvold, 2008). The NVZ formed more than 12 million years ago (Hjartardóttir, 2013). NVZ contains about 5 volcanic systems with central volcanoes and fissure swarms.

A recent study from Hjartardóttir (2013) in NVZ showed that eruptions are less common at the distal parts of the fissure swarms than closer to the central volcanoes. The proximal parts of the fissure swarms also generally indicate higher fracture density, even when the effect of the age of the lava flows has been taken into account. Older lava flows such as Krafla and Askja Fissure Swarms have typically higher fracture densities, suggesting frequent dike intrusions into the same parts of the fissure swarms during postglacial times

In NVZ, Deformation primarily occurs within the central volcanoes especially where rifting episodes have recently taken place (Hjartardóttir et al, 2012). Earthquake activity in the NVZ reflects this pattern. During non-rifting periods, earthquakes usually take place within central volcanoes or at distinct places in the rift zone, often not within the fissure swarms (Einarsson, 1991). During rifting episodes, this pattern changes dramatically, as intensive earthquake activity is felt and measured both within the central volcanoes as well as in distinct parts of the fissure swarm associated with the volcano (Einarsson, 1991; Hjartardóttir et al., 2012; Hjartardóttir, 2013).

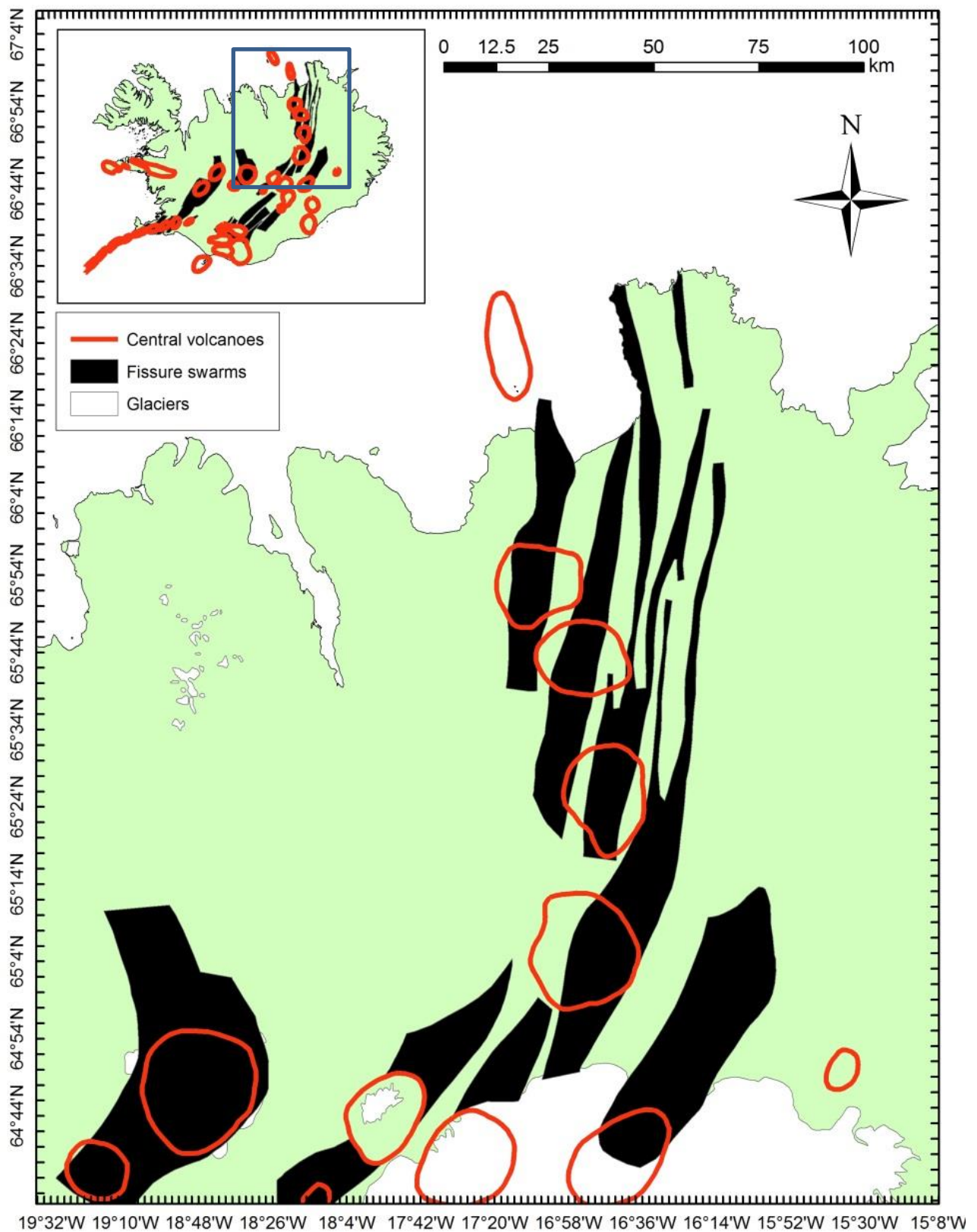


Fig. 16 The Northern Volcanic Zone and its fissure swarms. Blue frame in inserted and main Figure shows the location of the Northern Volcanic Zone in Iceland. Modified from Hjartardóttir (2013).

3.3 Krafla

Krafla is located in northern Iceland, approximately at latitude 65°42'53" N, and longitude 16°43'40" W (*cf.* Fig. 4). The Krafla central volcano has a ~8 km wide caldera that was formed in an eruption about 100,000 years ago (Rossi, 1997; Hjartardóttir et al., 2012). The caldera has since then widened about 2 km in an East-West direction due to plate spreading (Einarsson, 1991). The Krafla volcano is primarily basaltic, but silicic deposits are found in the vicinity of the caldera (Einarsson, 1991; Hjartardóttir et al., 2012). The magma chamber below Krafla is thought to be irregular in form (Hjartardóttir, 2013). The top of the chamber is situated at about 3 km depth, while the bottom of it is probably at less than 7 km depth (Einarsson, 1991). Analysis of ground deformation indicate that deeper magma reservoirs are also present (Hjartardóttir et al., 2012). Such a complex of magma chambers or reservoirs is also supported by studies of Grönvold (2008) which show that magma erupted during the Krafla rifting episode in 1975–1984 came from different magma reservoirs.

The Krafla fissure swarm is estimated to be about 80 km long and 4-10 km wide, consisting of more than 1000 tectonic fractures (Einarsson, 1991). The volcanism within the Krafla system is compositionally bimodal; the historic volcanism is dominated by tholeiitic basalt production. During the Holocene, Krafla has had many eruptive events. According to Thordarson & Larsen (2007) two major eruption episodes have occurred within the last 250 years in the Krafla fissure swarm. The former in the years 1724-1729, which is described as the "Mývatn fires", and the latter in the years 1975-1984, which is described as the "Krafla fires".

In the Krafla fires, the lava flows cover an area of about 36 km² and the total length of the discontinuous volcanic fissure is 11 km (Einarsson, 1991). During Krafla fires episodes, periods of intense earthquake activity and fault movements (often accommodating graben subsidence) occurred within the fissure swarm (Hjartardóttir et al., 2012). The rifting was accompanied by fissure eruptions (Einarsson, 1991; Hjartardóttir et al., 2012). Following the last episode of this event in September 1984, the Krafla magma chamber inflated again eventually fully recovering previous land elevation (Smithsonian Institution, 2013). Fig. 17 shows the lava flows which the Krafla fires produced in 1975-1984, covering an area of 36 km², a volume of 0.25-0.3 km³ (Thordarson & Larsen, 2007).

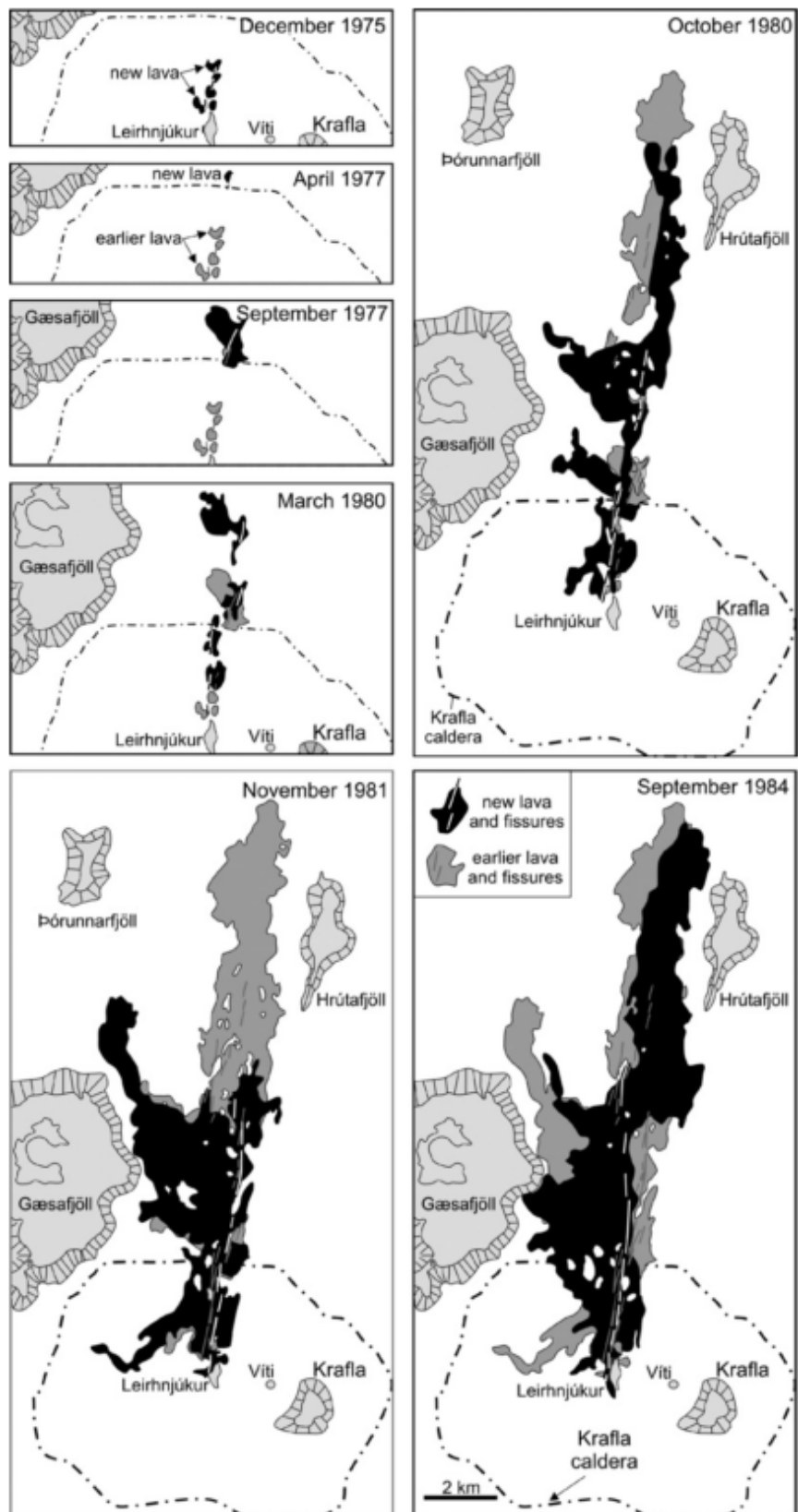


Fig. 17 Lava flows produced by the eruptions of the 1975–84 Krafla Fires (Thordarson & Larsen, 2007).

3.4 Krafla's Lava Morphology

Krafla's last eruptive episode, i.e. the "Krafla Fires", resulted in 21 tectonic events, and 9 volcanic eruptions (Björnsson, 1985; Einarsson, 1991). The total area covered with lavas is 36 km² and its volume is about 0.25-0.3 km³ (Einarsson, 1991). Fig. 18 shows that there are two temporal stages which formed the lava field that is the initial pahoehoe sheet and the later open channel flow (Rossi, 1997).

The eruption started on the 20th of December 1975, with the opening of a fissure which consisted of separate segments and had a total length of 8.5 km. The last and the largest episode started on the 4th of September 1984 and continued for two weeks (e.g. Rossi, 1997). Rossi (1997) shows that this volcanic fissure released a pahoehoe sheet which was emplaced mainly to the west of the fissure system. After two days of eruption, the effusive activity concentrated in one crater at the northern end of the fissure system. To the south of that crater only one vent remained active with slight phreatic activity.

The northern crater released olivine tholeiitic lava for 12 days (Rossi, 1997; Smithsonian Institution, 2013a). Lava fountaining in that crater created a spatter cone with a diameter of about 200 m. Lava flowed out from the crater from a breach in the spatter cone on its southern side. From there, the lava flowed out to the east and then followed the topographic depression of the rift valley towards the north. The lava flow was bounded on its western side by the January-February 1981 lava flow and on its eastern side partly by a fault scarp (Rossi, 1997). The final open-channel lava flow is 9 km long and 1 to 2 km wide (Fig. 18). The total area of the lava field that formed in two weeks of eruption is 24 km², of which the open-channel lava flow covers about 40% (Rossi, 1997).

Morphology of the open channel lava flows in Krafla have been mapped by Rossi (1997) and five flow facies are recognized (1) the initial pahoehoe sheet; (2) proximal slab pahoehoe and aa; (3) shelly-type overflows from the channel; (4) distal rubbly aa lava; and (5) secondary outbreaks of toothpaste lava and cauliflower aa. Around 55% is classified as aa, 32% as pahoehoe and the remaining 13% is the main lava channel (Fig. 19). The previous study by Rossi (1997) was primarily field mapping, video recording and measured pre-flow topography from aerial photographs.

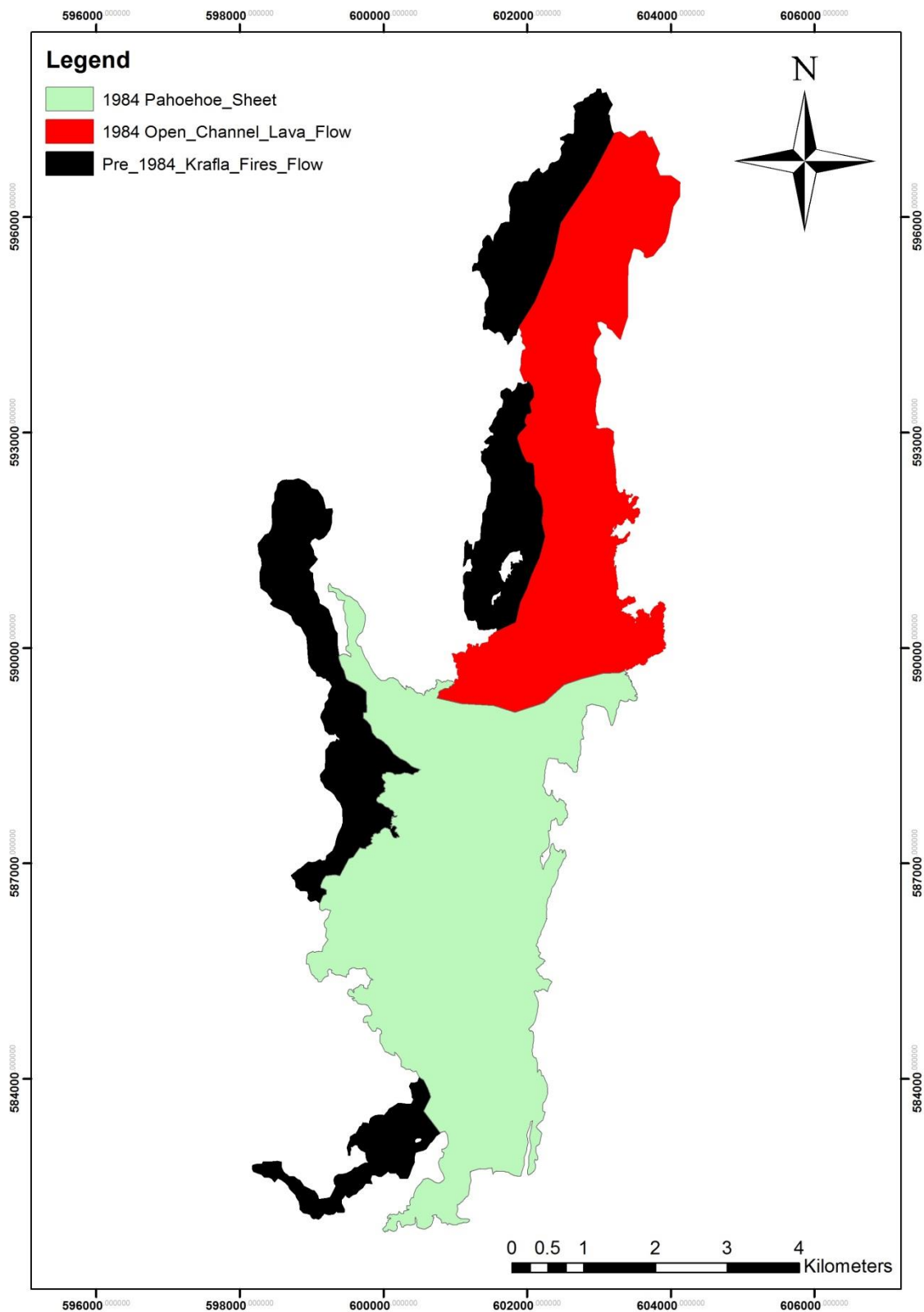


Fig. 18 Lava flows from the Krafla Fires. The open-channel lava flow and initial pahoehoe . Modified from Rossi (1997).

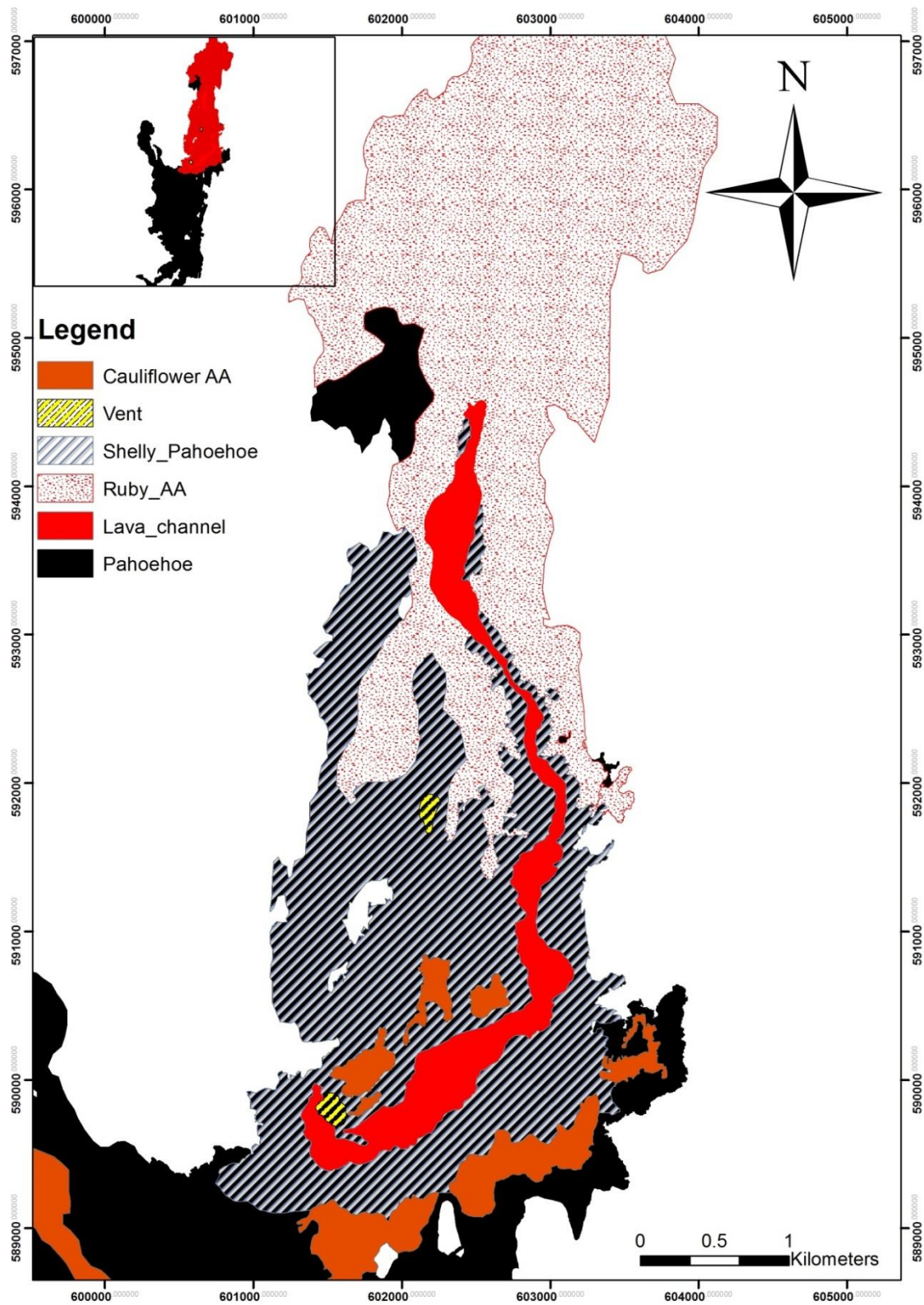


Fig. 19 Surface morphology and lava channels of the 1984 open-channel lava flow. Modified from Rossi (1997).

In this study five types of morphological lava are used that were recognized by Rossi (1997) in the Krafla lava field (Table 3).

Table 3. Description of morphological lava types of the 1984 open-channel lava flow in Krafla (Rossi, 1997).

Morphological lava type	Descriptions
Pahoehoe sheet	Smooth surface is divided into subhorizontal crustal plates, sometimes slightly buckled against each other. Flooding lava often forms pools when restricted by the surrounding topography, and may form perched lava ponds. In the pools, the cooling lava may convert in a manner observed in Hawaiian lava lakes. As the lava loses gas its volume decreases and the lava surface deflates. This process leaves high-lava marks against the surrounding topographical highs. Shelly-type lava lobes often form the margin of the sheet flow. Although sometimes ropy, the lava surface commonly lacks ropy textures.
Shelly-type lava	Very vesicular pahoehoe lava type with fragile lava crust. It forms flow lobes and small lava tubes which become hollow inside as lava drains downslope or as the molten lava in the lobe-interior loses gas. Slightly buckled lava crusts and small lava channels up to a few meters in width are common on shelly-type lava flows
Slabby pahoehoe	In Krafla cauliflower aa is often associated with slab pahoehoe. Forms from pahoehoe crust which is stretched and tilted during flow. Appears in lava channels where it is generally transitional between pahoehoe and aa. Tilted crustal plates also appear locally in sheet flows in a non-channelised flow regime.
Cauliflower aa	Irregular protrusions which resemble cauliflowers occur on the lava surface. This is an initial aa lava type in the transformation from pahoehoe to rubbly aa. Protrusions are initially attached to the massive lava beneath but commonly break and form loose debris on the flow surface.
Rubbly aa	Aa lava with a clinkery and blocky surface. Surface breccia varies from sand size to blocks several meters in diameter. Clasts are often slightly rounded due to attrition between the clasts during flow. This lava type has high thermal maturity; the crust during flow is broken by brittle failure

4 Data and Methods

To assess the potential of using hyperspectral and multispectral remote sensing for identifying lava surface morphology in the Krafla lava fields, the following three types of satellite data were used:

- EO-1 Hyperion (Hyperspectral)
- Landsat 8 OLI (Multispectral)
- SPOT 5 (Multispectral) & Panchromatic

Additionally, aerial photographs were used as a reference for lava morphology and to overlay with Krafla's open channel map from Rossi (1997). The data were acquired from different sources, from (1) the National Land Survey of Iceland (*Landmælingar Íslands*) for polygon map of Iceland; (2) *Samsýn* for aerial photograph via Institute of Earth Science, University of Iceland; (3) USGS (U.S. Geological Survey) for EO-1 Hyperion and Landsat 8 OLI; (4) Institute of Earth Science, University of Iceland for SPOT 5. Table 4 shows the description of those data.

There are mainly three software which are used in this study; (1) ArcMap® 10.2; (2) ERDAS Imagine® 2014 and (3) ENVI® 5.1 .

Table 4. Description of satellites and aerial data used in this study.

Satellites/Aerial Image	Spatial Resolution (m)	Date Acquisition	Band	Wavelength (nm)
EO-1 Hyperion	30	July 17 th , 2012	242	355.59 - 2577.08
Landsat 8 OLI	30	August 28 th , 2014	11	443 - 2201
SPOT 5	10	October 3 rd , 2002	4	500 - 1750
SPOT 5 Panchromatic	2.5	October 3 rd , 2002	1 (Panchromatic)	480 - 700
Aerial Photograph	0.5	July 28 th , 2012	3 (Visible)	400 - 700

In order to process the data, the workflow is divided into four main steps (Fig. 20):

1. Visual image interpretation
2. Histogram/pixel image interpretation
3. Spectral image Interpretation
4. Accuracy assessment.

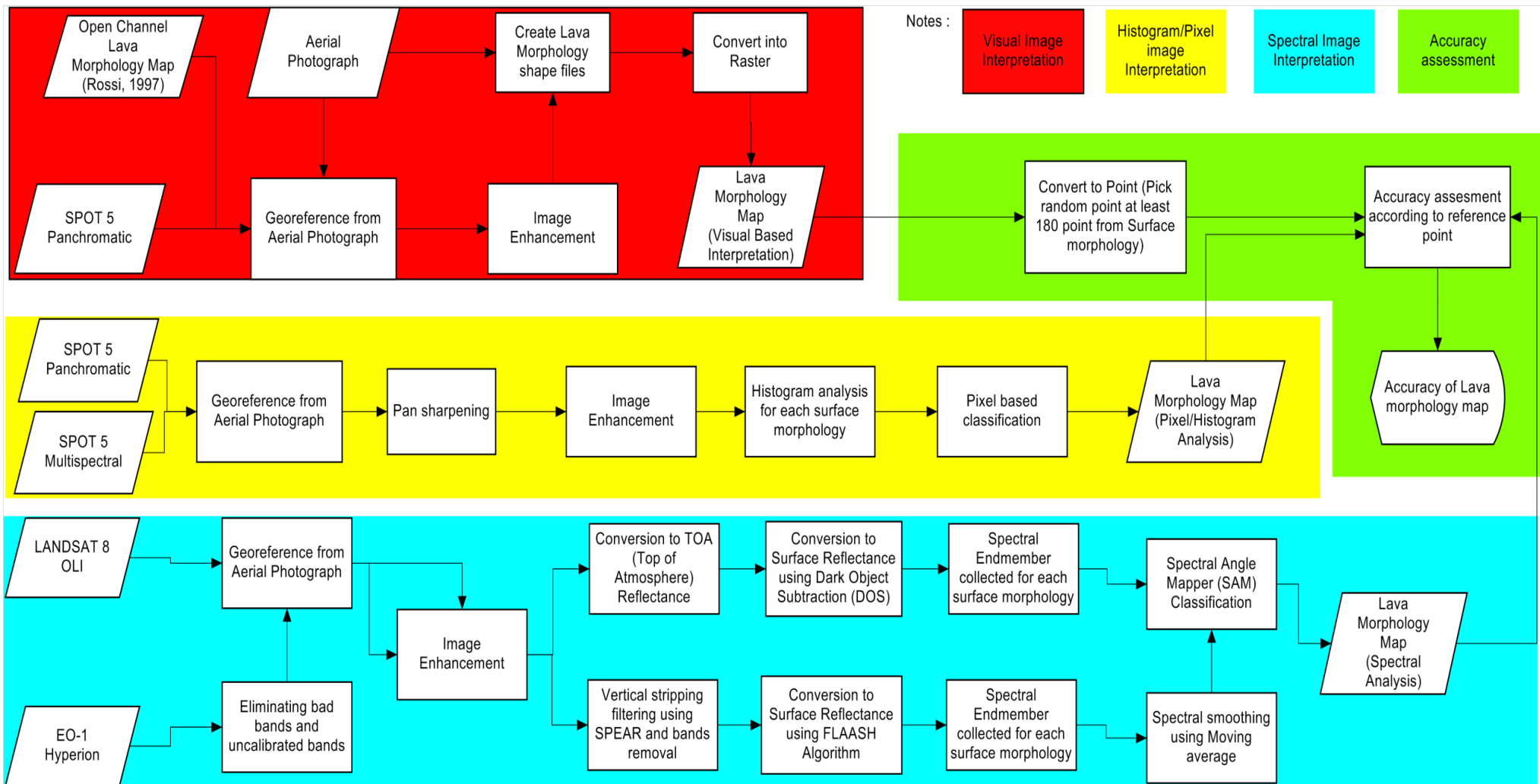


Fig. 20. A general flow chart of the study's work procedure. The four main steps are emphasized by different colors.

4.1 Visual Image Interpretation

As a first step the lava morphology was mapped from interpretation of very high resolution aerial photographs (0.5 meter resolution) provided by Samsýn (Fig. 21a). This aerial photography gives a good insight to the variety of surface morphology within the Krafla lava field. The outlines of the different lava morphology was derived from combinations of aerial photographs and Krafla's open channel lava morphology map from Rossi (1997) (Fig. 19). These combinations were made because it was difficult to distinguish between pahoehoe and shelly pahoehoe from the aerial photograph and also for reference points; SPOT 5 Panchromatic image was furthermore used in order to add the missing lava scene in the northern part of the aerial photograph (Fig. 21b) as well as to help distinguish the lava morphology after image enhancement.

In the interpretation the lava types cauliflower aa and slabby pahoehoe were combined according to Rossi (1997), because in the Krafla lava field cauliflower aa is often associated with slab pahoehoe.

4.1.1 SPOT 5 Panchromatic Pre-Processing

The SPOT 5 image used is dated from the 3rd of October 2002, with a panchromatic band (480–700 nm) and 2.5 meter resolution. SPOT 5 panchromatic was used in order to help visual image interpretation of each texture because the images clearly distinguish surface morphology of the lava field as good as aerial photographs. The image was projected in the Lambert Conformal Conic coordinate system on the ISN 1993 Lambert 1993 datum.

Image enhancement is used in order to clearly distinguish different lava textures. According to Kassouk et al (2014) the range of hues in panchromatic images and the diversity or complexity of volcanic structures are limited despite the image enhancement processing. This is why the rainbow color with 10 scale colors is added - in order to see the textures from visualization. The linear 5% method was used, which enhances the color and tonal variations. The contrast of the image was then improved by changing the intensity level of the pixels based on the intensity distribution of the input image. Fig. 22 shows a part of the original SPOT5 image of the study area after the linear 5% stretching. As a result of the image processing procedures the lava textures can be better distinguished.

A total of seven classes were distinguished, i.e.: (1) Rubbly aa; (2) old lava (1724-1729) (3) cauliflower aa and slabby pahoehoe; (4) pahoehoe; (5) shelly pahoehoe; (6) lava channel and (7) lava vent (Fig. 26). Only five classes were used for accuracy assessment excluding lava channel and lava vent (cauliflower aa, shelly pahoehoe, rubbly aa, shelly pahoehoe and old lava). This due the surface of main lava channel consisting of loose fragments. The smallest fragments are scoriaceous aa-clasts and aa-cauliflowers. Many large blocks are plates of pahoehoe crust rafted from the upstream parts of the flow (Rossi, 1997). Vents from which the lava was produced were not classified by lava morphology.

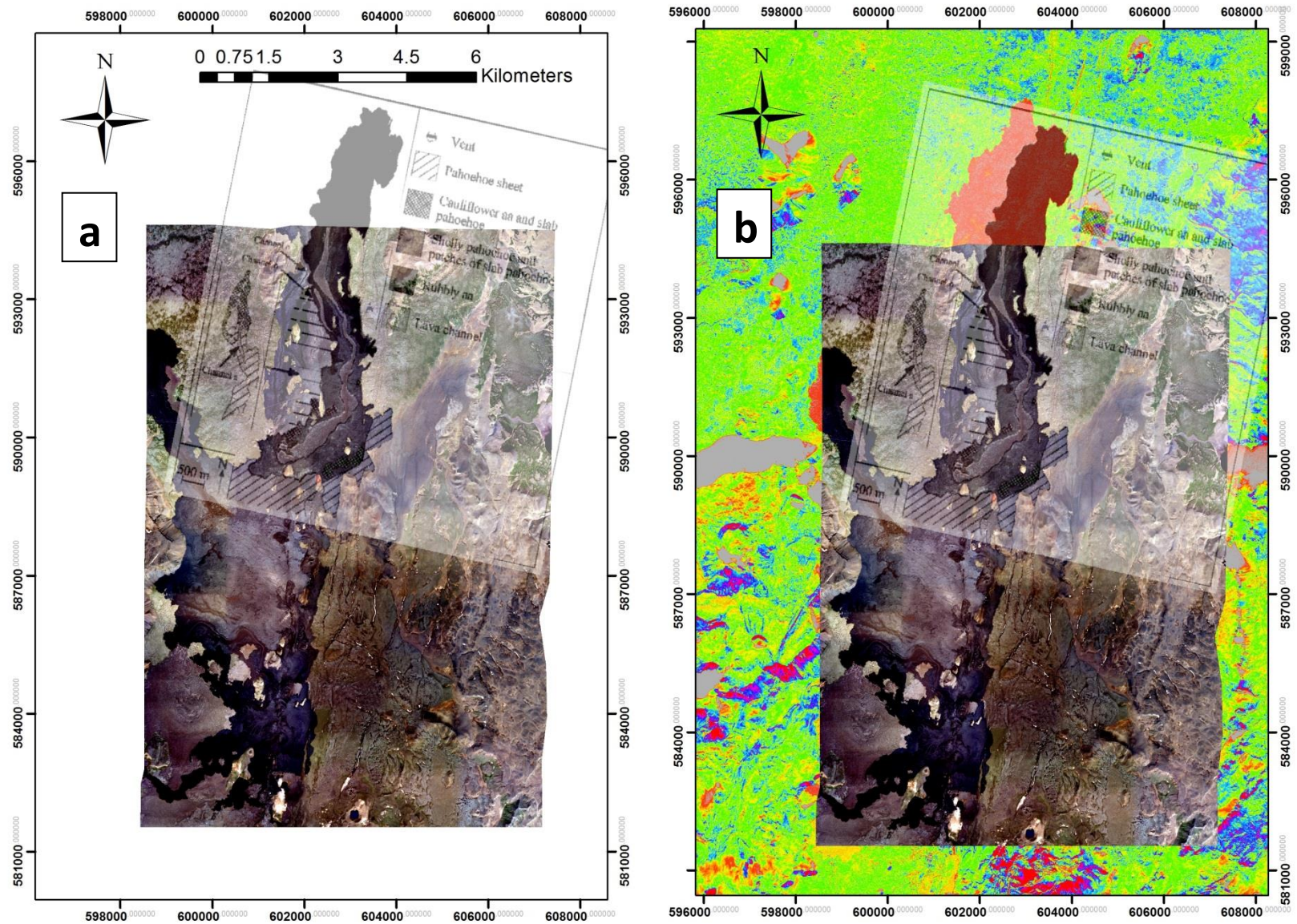


Fig. 21. Base map making process of the Krafla lava flow used for the surface analysis (a) Overlaying Rossi (1997) open channel map with aerial photograph; (b) Overlaying Rossi (1997) open channel map with aerial photograph and include spot 5 panchromatic.

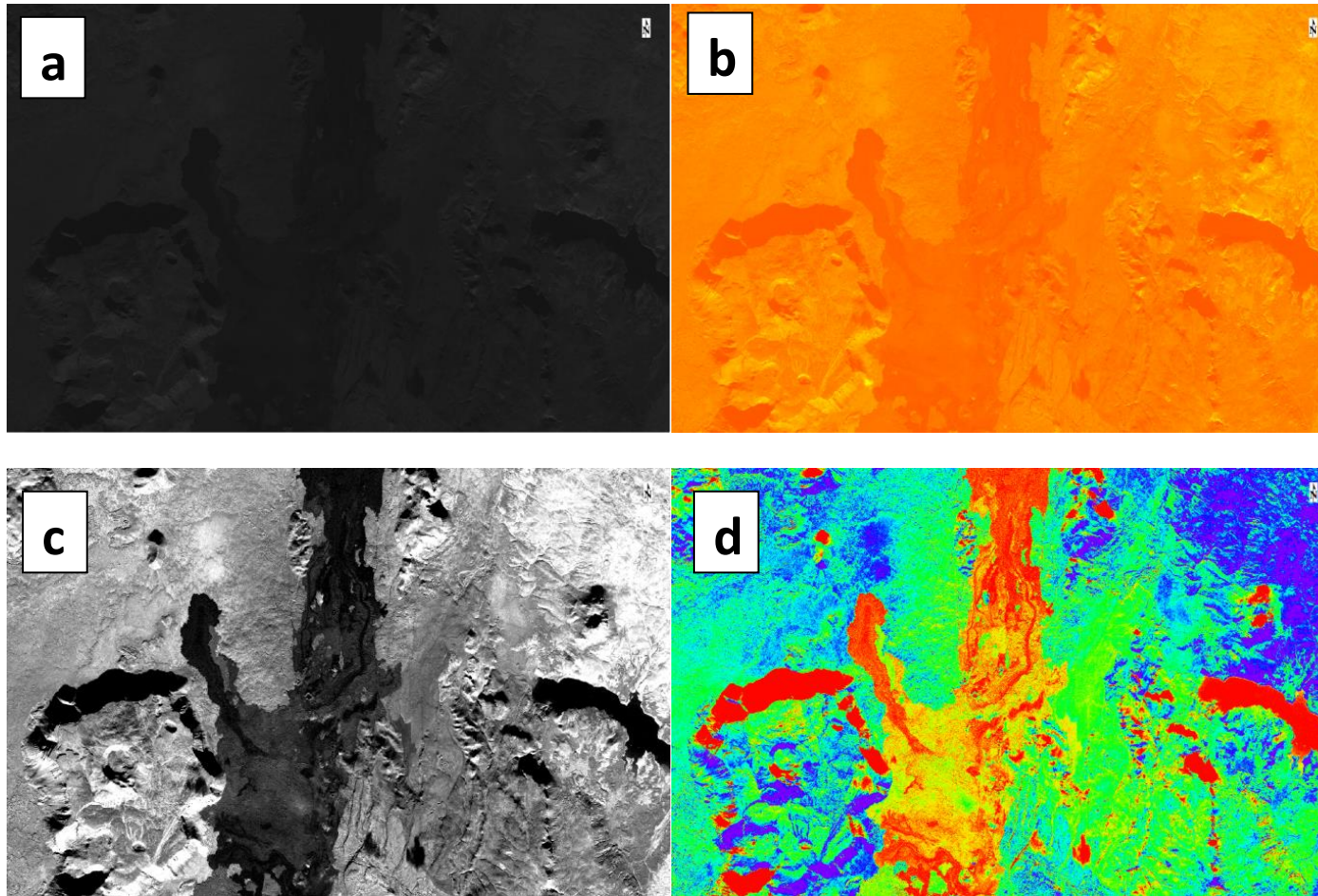


Fig. 22 (a) Image before enhancement in grayscale; (b) image before enhancements in rainbow scale; (c) Image after the linear 5% enhancements in grayscale; (d) image after the linear 5% enhancements in rainbow scale.

4.1.2 Creation of random points

In order to create sample points to be used in accuracy assessment of satellite image results, random points were generated. The sampling strategy that purposed on this method is random equal-stratified sampling (Hirzel & Guisan, 2002). The identical number of points is randomly selected in each class; the number chosen corresponds as closely as possible to the total number of points in the desired sample size. This process was done in ArcMap® 10.2, using the “Create Random Points” tool on the lava morphology feature class (Fig. 23). Points were randomly placed inside polygon features, along line features, or at point feature locations (ESRI, n.d.). Each feature in this feature class had the specified number of points generated inside it, with no points being closer than 20 meters to each other. In this case, if we specify 30 points, and the lava morphology feature class has 5 features (excluding lava vents and lava channel), 30 random points will be generated in each surface morphology, totaling 150 points.

Fig. 24 shows how random points were generated across the Krafla lava field. Every process of this tool will generate different points. These 150 points will be used for accuracy assessment of in the final step.

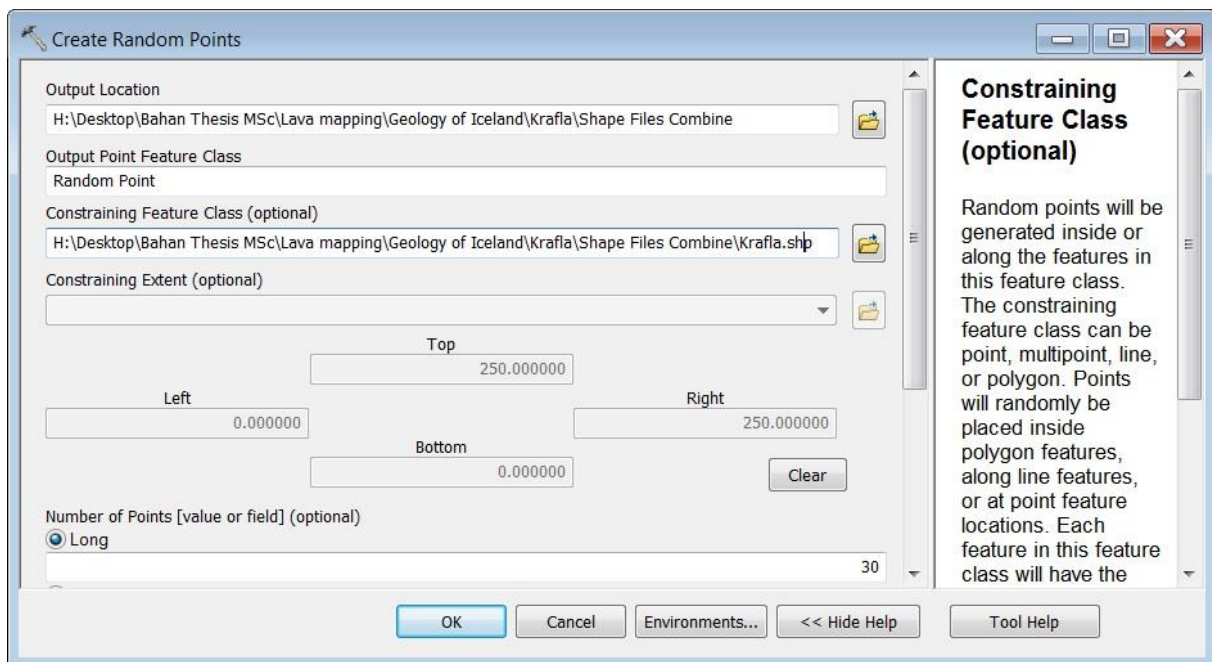


Fig. 23 The create random points tool in ArcGIS with 30 point each morphology and 20 meters minimum distance.

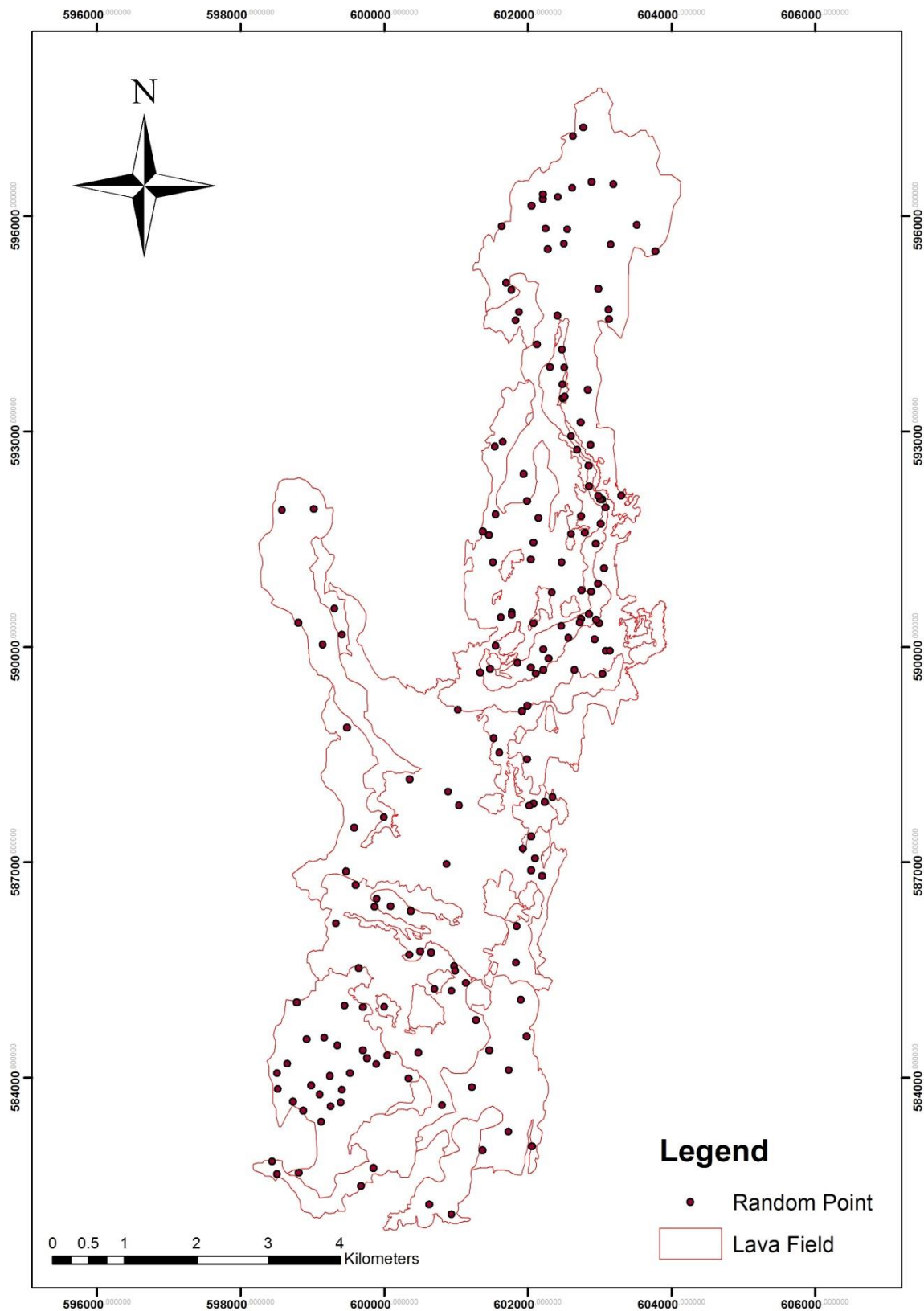


Fig. 24 The location of the 150 random points generated in the Krafla's lava field.

4.2 Histogram/Pixel Interpretation

This method will use SPOT 5 (Both panchromatic and multispectral band) in order to get a pixel histogram from the lava morphology. A description of the SPOT 5 images is shown in table 5. A histogram is a graph showing the number of pixels in an image at each different intensity value found in that image. For an 8-bit greyscale image there are 256 different possible intensities, and so the histogram will graphically display 256 numbers showing the distribution of pixels amongst those greyscale values. Histogram analysis shows the distribution of digital number (DN) from surface morphology.

Table 5. Description of SPOT 5 data which used in this study.

Spectral Bands	Resolution (m)	Wavelengths (nm)
B1 (Blue)	10	500 – 590
B2 (Red)	10	610 – 680
B3 (NIR)	10	780 – 890
B4 (SWIR)	20	1580 – 1750
Panchromatic	2.5	480 – 700

4.2.1 SPOT 5 Pre-Processing

SPOT 5 images, both multispectral and panchromatic, were projected into the Lambert Conformal Conic coordinate system on the ISN 1993 Lambert 1993 datum. In this method the panchromatic band is used to sharpen the multispectral band. Pan sharpening means using a panchromatic (single band) image to “sharpen” a multispectral image. In this case, to “sharpen” means to increase the spatial resolution of a multispectral image. A multispectral image contains a higher degree of spectral resolution than a panchromatic image, while often a panchromatic image will have a higher spatial resolution than a multispectral image. A pan-sharpened image represents a sensor fusion between the multispectral and panchromatic images which gives the best of both image types, high spectral resolution and high spatial resolution. Fig. 25 shows the SPOT 5 image (False color: 4-3-2) before and after sharpening.

For further processing and image enhancement, the histogram equalization method was used, which enhances the color variations and improves the dynamic range of the raster image. Histogram equalization employs a monotonic, non-linear mapping which re-assigns the intensity values of pixels in the input image such that the output image contains a uniform distribution of intensities (*i.e.* a flat histogram). This technique is used in image comparison of lava because it is effective in detail enhancement (Fig. 26).

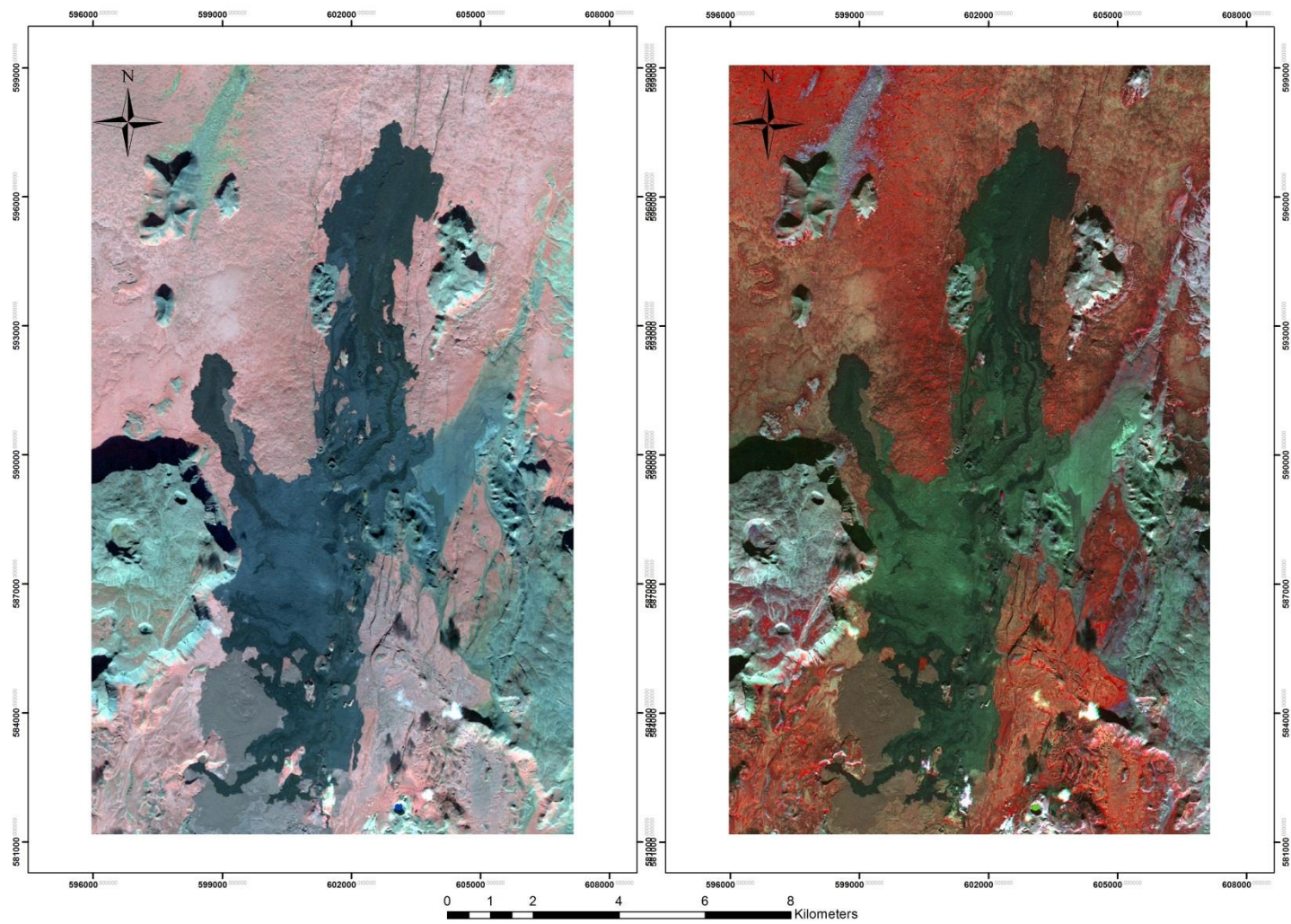


Fig. 25 (a) SPOT 5 Image before pan sharpening; (b) SPOT 5 Image before pan sharpening.

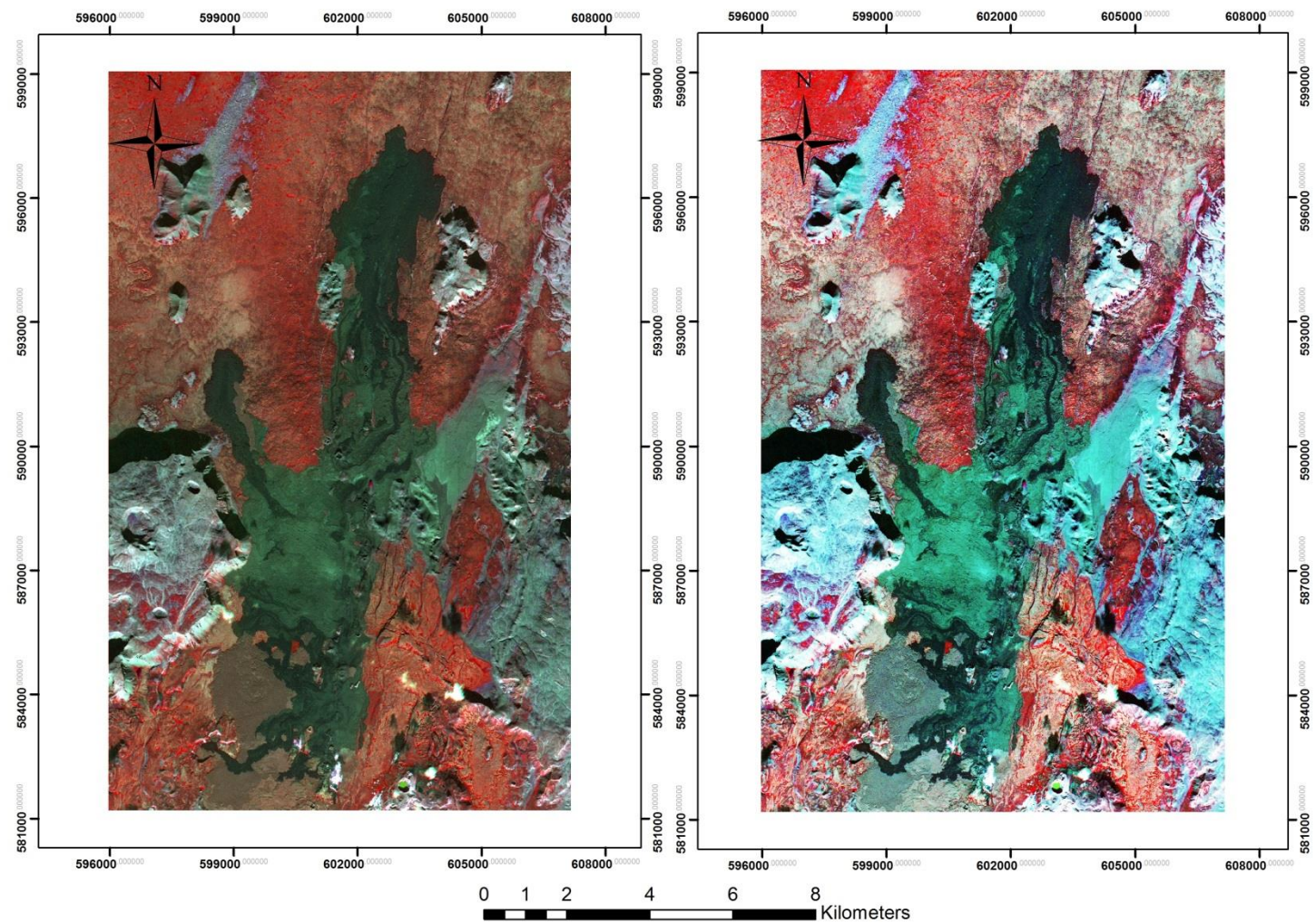


Fig. 26 (a) SPOT 5 Image before histogram equalization; (b) SPOT 5 Image after histogram equalization.

4.2.2 SPOT 5 training samples selection

This section explains how the image is classified by signatures using the area of interest (AOI) tools. This step was done using ERDAS Imagine® 2014. Fig. 27 and Fig. 28 show nine training samples which were collected. There include five type of lava morphology (1) pahoehoe; (2) rubbly aa; (3) old lava; (4) cauliflower aa; and (5) shelly pahoehoe. The other classes are; (6) sandur deposit; (7) upper Pleistocene formation; (8) vegetation and (9) water. Training samples were used for image classification. These samples were picked to represent classifications given by Rossi (1997) for the open channel lavas. Areas outside of the open channel were sampled according to visualization, homogeneous area and the geological map provided by Thordarson and Hoskuldsson (2014). These points were also used in endmember spectra collection in the next method.

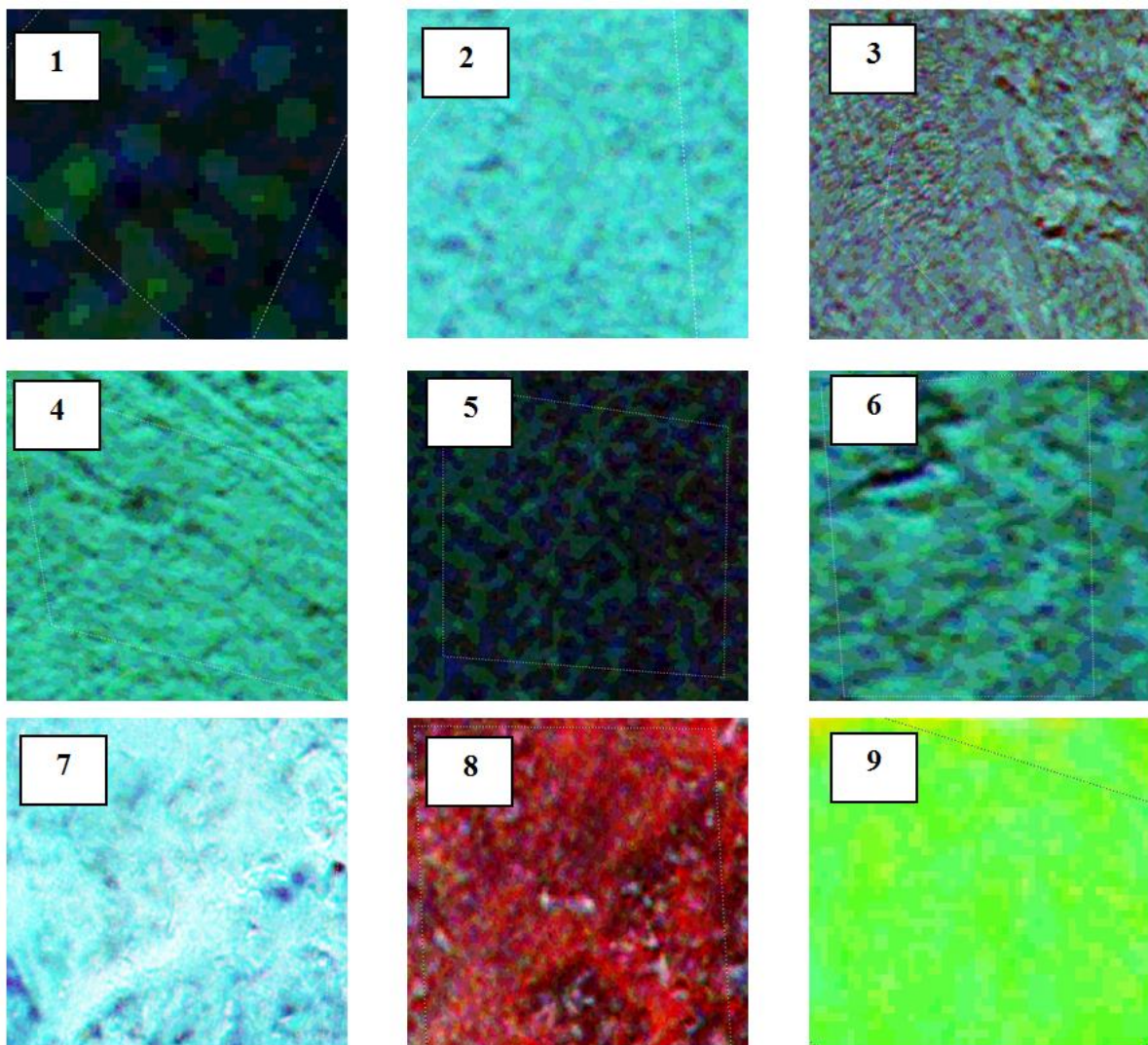


Fig. 27 Nine samples were collected from SPOT 5 image of Krafla area : (1) Rubbly AA; (2) sandur deposit; (3) Old Lava; (4) Pahoehoe; (5) Cauliflower AA; (6) Shelly Pahoehoe; (7) Upper Pleistocene formation; (8) Vegetation; and (9) Water.

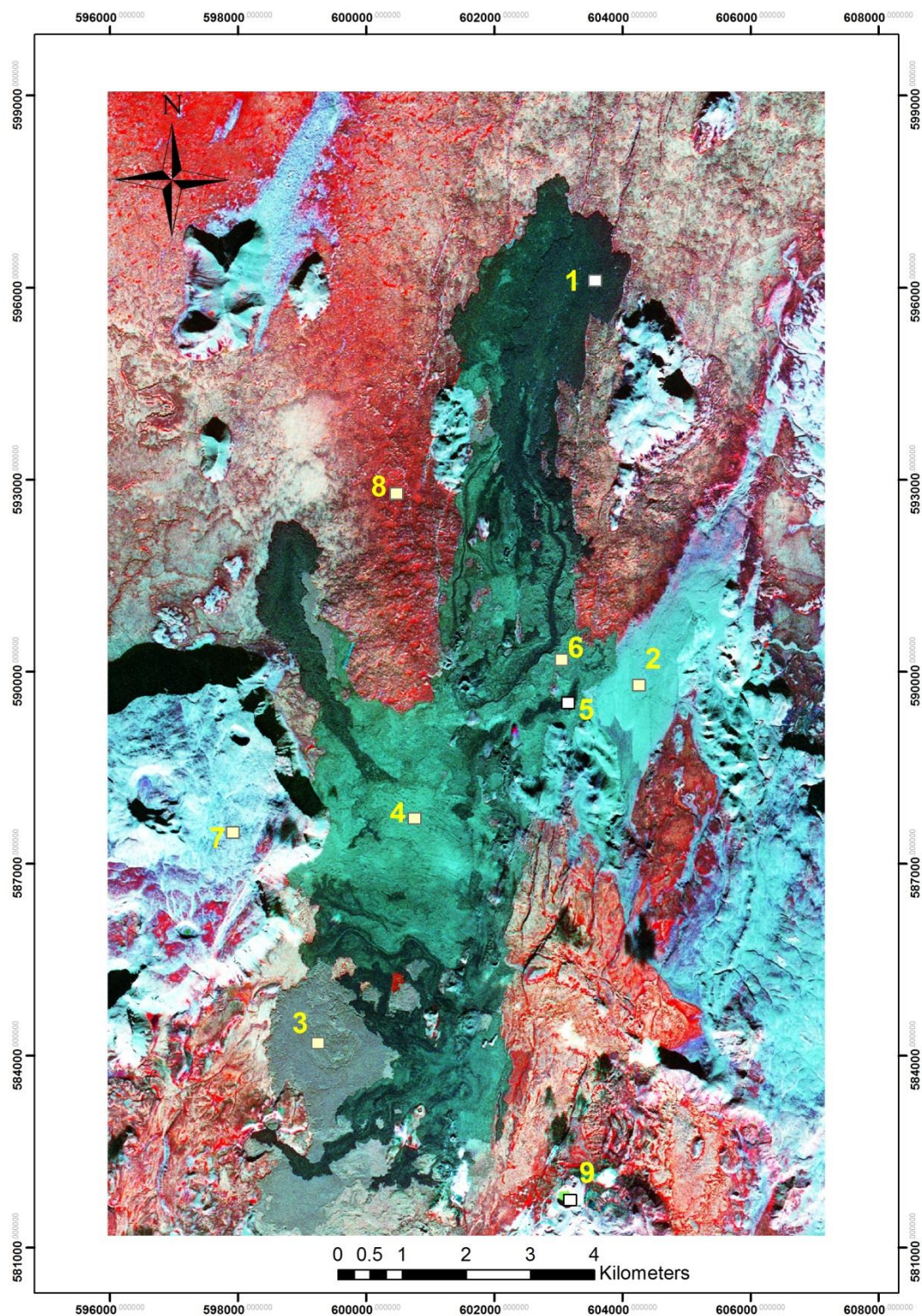


Fig. 28 Nine sample points from SPOT 5 image of Krafla area : (1) Rubbly AA; (2) sandur deposit; (3) Old Lava; (4) Pahoehoe; (5) Cauliflower AA; (6) Shelly Pahoehoe; (7) Upper Pleistocene formation; (8) Vegetation; and (9) Water.

4.2.3 Pixel histogram distribution

Histogram distribution was obtained from nine samples in the image. This histogram is a graph showing the number of pixels in an image at each different intensity value found in that image. In Fig. 29, under count there is the number of pixels, which are sampled. In order to apply later on the supervised classification (maximum likelihood classification), theoretically need $N+1$ pixels for each class (N = no. of bands) (Richards & Jia, 2006). In our case we have four bands, so at least five pixels are needed for each sample. In the results there are four histograms generated for each samples.

Signature Name	Color	Red	Green	Blue	Value	Order	Count	Prob.
Rubbly AA		0.647	0.000	0.000	2	2	972	1.000
Vegetation		0.000	1.000	0.000	3	3	5506	1.000
Sandur deposit		1.000	1.000	0.000	4	4	3181	1.000
Shelly Pahoehoe		0.000	1.000	1.000	5	5	848	1.000
Cauliflower AA		1.000	0.000	0.000	6	6	304	1.000
Pahoehoe		0.000	0.000	1.000	7	7	3116	1.000
Old Lava		1.000	1.000	1.000	8	8	4905	1.000
Upper Pleistocene Format		0.627	0.125	0.941	9	9	7790	1.000
Water		0.000	0.000	0.000	1	10	164	1.000

Fig. 29 Number of pixels which sampled for each class.

4.2.4 Supervised classification (Maximum likelihood classification)

This method will classify and produce a map from histogram distribution sample points. ERDAS Imagine applies maximum likelihood classification by calculating the following discriminant functions for each pixel in the image as the equation below (Richards, 1999):

$$g_i(x) = \ln p \left| \sum i \right| - \frac{1}{2} (x - m_i)^T \sum_i^{-1} (x - m_i)$$

i = Class

x = n -dimensional data (where n is the number of bands)

$\left| \sum i \right|$ = Determinant of the covariance matrix of the data in class ω_i

\sum_i^{-1} = Inverse matrix

m_i = Mean vector

Supervised classification requires prior knowledge of the objects to be classified to produce the training set based on spectral or pixel groupings. Maximum likelihood classification assumes that the statistics for each class in each band are normally distributed and calculates

the probability that a given pixel belongs to a specific class. Unless you select a probability threshold, all pixels are classified. Each pixel is assigned to the class that has the highest probability, that is, the maximum likelihood. If the highest probability is smaller than a threshold (in this case threshold probability is 1), the pixel remains unclassified (Richards, 1999).

4.3 Spectral Image interpretation

In this method, spectra are picked from the image at selected areas that were known to the interpreter from field work or previous studies. Nine spectral endmember points from each morphological type were collected for multispectral and eight spectral endmember points for hyperspectral.

4.3.1 Multispectral Image

A multispectral image is one that captures image data at specific frequencies across the EM spectrum. Spectral imaging can use bands of the EM spectrum that the human eye cannot detect. It was originally developed for space-based imaging. Multispectral images are the main type of images acquired by remote sensing (RS) radiometers. Separating the spectrum into many bands, multispectral is the opposite of panchromatic, which records only the total intensity of radiation falling on each pixel. Usually, satellites have three or more radiometers; for example, Landsat has seven).

4.3.2 Landsat 8 OLI Pre-Processing

The Landsat 8 OLI image from August 28th, 2014 was used in this method. The first step of the data pre-processing consisted of geometric correction, radiometric correction and atmospheric correction. Geometric correction was done by projecting the image in the Lambert Conformal Conic coordinate system on the ISN 1993 Lambert 1993 datum.

Radiometric correction is important for the successful conversion of digital image data from satellites to calibrated surface quantities in the earth. Atmospheric correction has an objective to retrieve the surface reflectance (that characterizes the surface properties) from remotely sensed imagery by removing the atmospheric effects. The methods to perform radiometric and atmospheric correction are explained below.

Conversion to TOA Reflectance

According to the USGS OLI band data can be converted to TOA planetary reflectance using reflectance rescaling coefficients provided in the product metadata file (MTL file). The following equation is used to convert DN values to TOA reflectance for OLI data as follows:

$$\rho\lambda' = M_\rho Q_{cal} + A_\rho$$

$\rho\lambda'$ = TOA planetary reflectance without correction for solar angle.

M_ρ = Band specific multiplicative rescaling factor from metadata.

A_ρ = Band-specific additive rescaling factor from the metadata.

Q_{cal} = Quantized and calibrated standard product digital number (DN)

TOA reflectance with a correction for the sun angle is then:

$$\rho\lambda = \frac{\rho\lambda'}{\cos(\theta_{sz})} = \frac{\rho\lambda'}{\sin(\theta_{se})}$$

$\rho\lambda$ = TOA planetary reflectance.

θ_{se} = Local sun elevation angle.

θ_{sz} = Local solar zenith angle; $\theta_{sz} = 90^\circ - \theta_{se}$

These equations were provided in the ENVI® 5.1 radiometric calibration packages (Fig. 30). For more accurate reflectance calculations, per pixel solar angles could be used instead of the scene center solar angle, but per pixel solar zenith angles are not currently provided with the Landsat 8 products.

Conversion to Surface Reflectance using Dark Object Subtraction (DOS)

Dark object subtraction (DOS) searches each band for the darkest pixel value. Assuming that dark objects reflect no light, any value greater than zero must result from atmospheric scattering. The scattering is removed by subtracting this value from every pixel in the band. This simple technique is effective for haze correction in multispectral data, but it should not be used for hyperspectral data. The principals of DOS includes (1) find the darkest object in the image; (2) assume that its spectral reflectance should be all zero (target radiance); (3) the measured values above zero are assumed to be the atmospheric noise (or path radiance) and uniformly distributed on the image area; (4) subtract the path radiance from each pixel radiance of the image, then we should get a relatively atmospheric free image. This process was done in ENVI® 5.1 as shown in Fig. 31.

Fig. 32 shows that the image before and after corrections was done. The image uses a true color composite (Band: 4-3-2). According to surface reflectance we can go further to analyze lava morphology by collecting reflectance spectra from selected area.

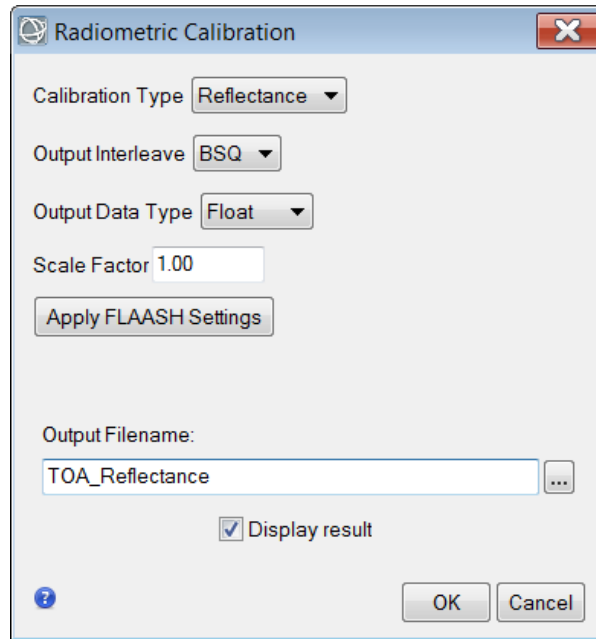


Fig. 30 Radiometric calibration to convert into TOA reflectance.

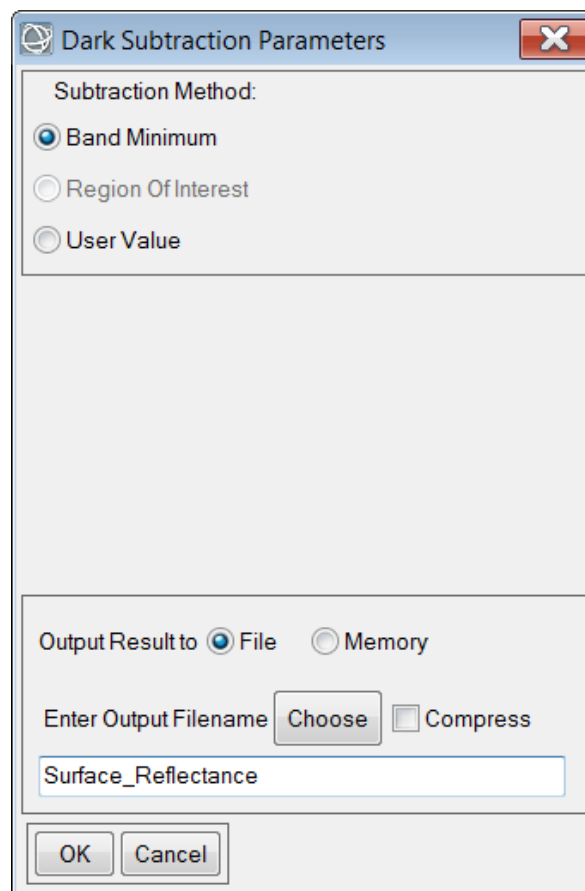


Fig. 31 Dark object subtraction (DOS) to convert into surface reflectance.

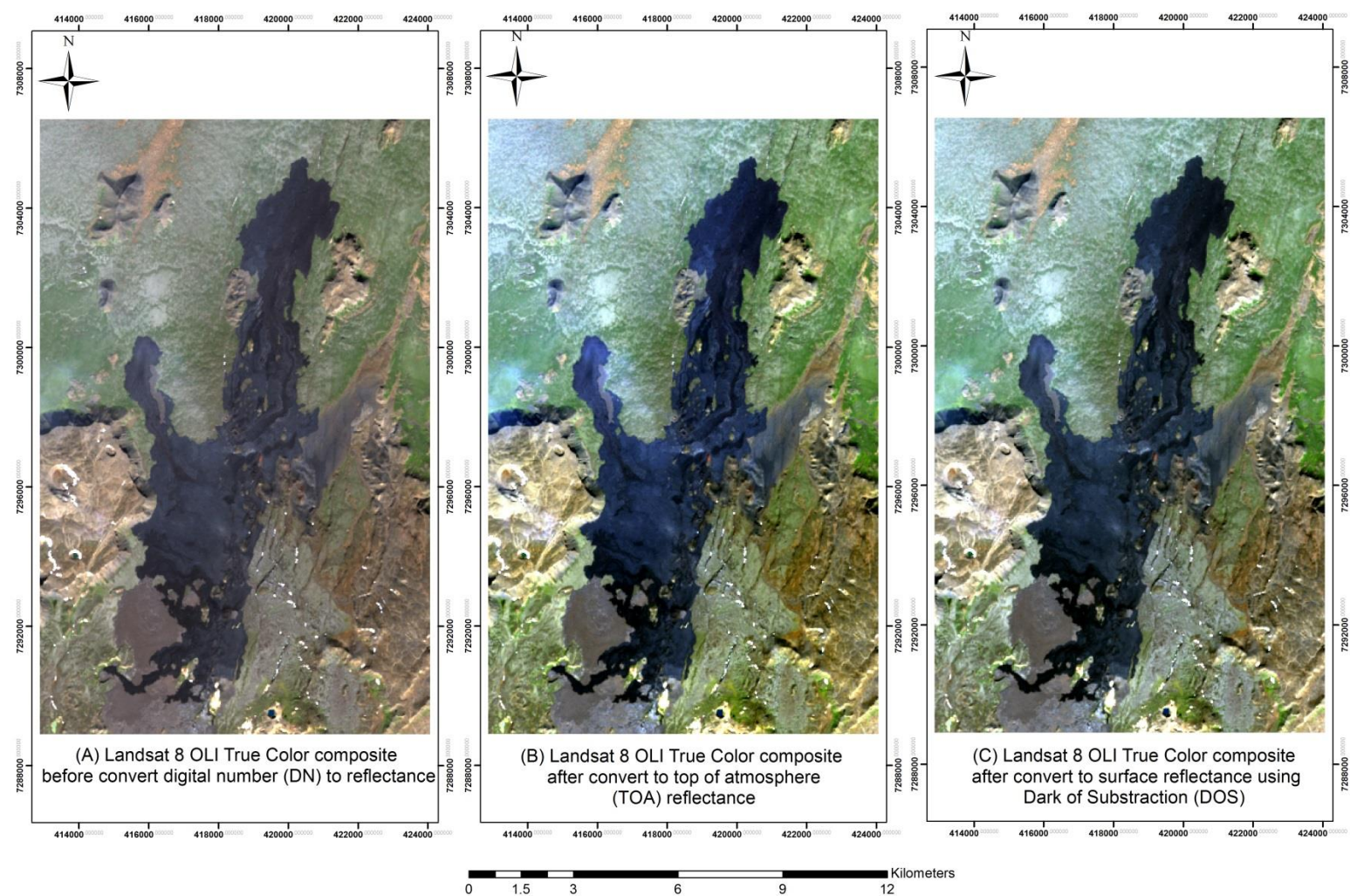


Fig. 32 (a) Image before convert to TOA reflectance; (b) Image after convert to TOA reflectance; (c) Image after convert to surface reflectance.

4.3.3 Landsat 8 OLI spectral endmember selection

In this method, spectra are picked from the image at selected areas that were known to the interpreter from field work or previous studies. Nine spectral endmember points from each morphological type were collected (Fig. 34 and Fig. 35). These include five type of lava morphology (1) pahoehoe; (2) ruby aa; (3) old lava; (4) cauliflower aa; and (5) shelly pahoehoe. The other classes are; (6) Holocene lava formation; (7) upper Pleistocene formation; (8) vegetation and (9) water. Endmembers of lava morphology were chosen according to the classification of Rossi (1997) for inside the main lava channel and according to visualization, spectral characteristic and also the geological map that provide by Thordarson and Hoskuldsson (2014). Nine spectral reflectance curves were obtained according to these endmember points (Fig. 36). These spectral will be classified in the next step using Spectral Angle Mapper (SAM).

Spectral endmember is the average spectral signature of a pure surface cover type in the image that represents a class that we want to spectrally classify or identify in an image (Fig. 33). Pure spectral endmembers are usually defined under idealized in situ or laboratory conditions where reflectance spectra are acquired using a portable spectrometer that focus only on a single surface. When in situ measurements are not possible, spectral endmembers can also be derived from "pure" features in the imagery. Selection of endmembers from the image itself can be done when having prior knowledge on the occurrence of materials imaged in the scene. Manual picking from image data assumes spectral homogeneity.

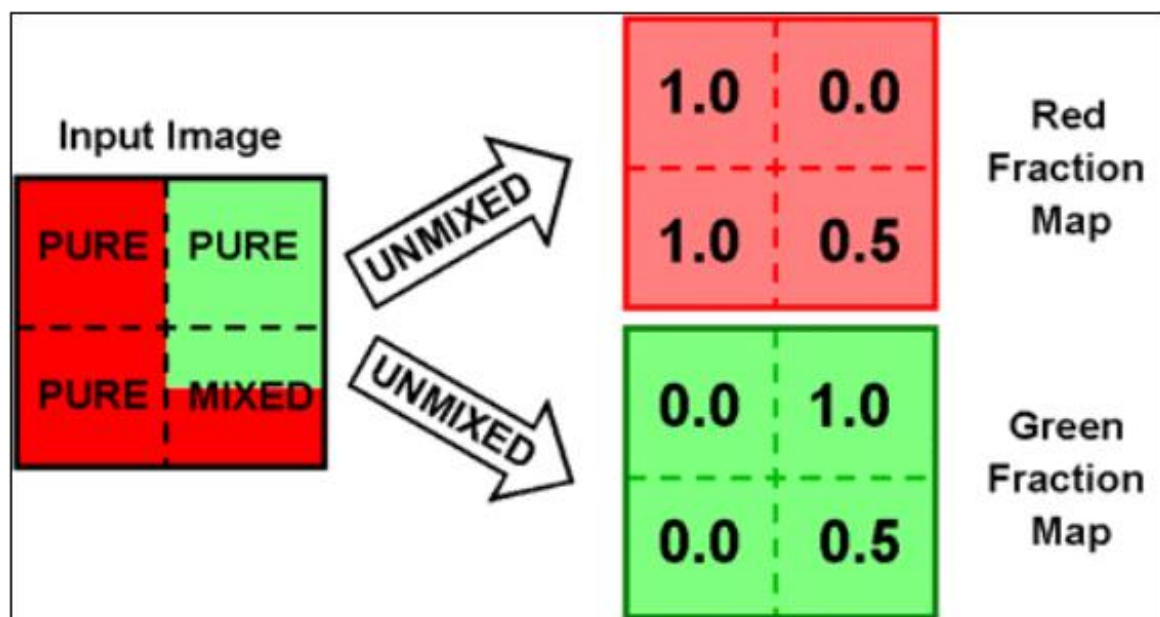


Fig. 33 Illustration of mixed pixels and pure pixel (Newland, 1999).

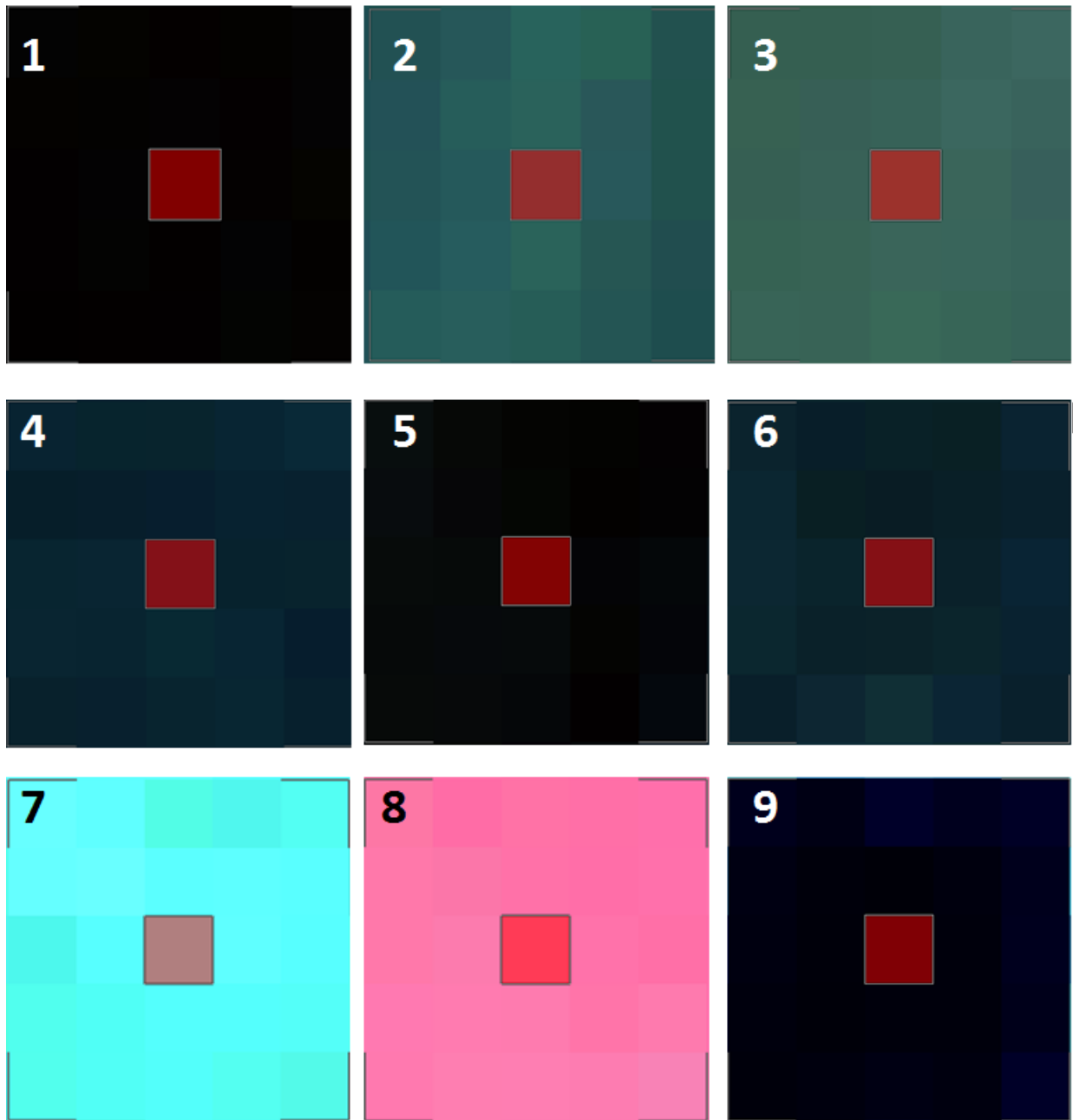


Fig. 34 Nine spectral endmember were collected from Landsat 8 OLI of Krafla area : (1) Rubbly AA; (2) sandur deposit; (3) Old Lava; (4) Pahoehoe; (5) Cauliflower AA; (6) Shelly Pahoehoe; (7) Upper Pleistocene formation; (8) Vegetation; and (9) Water.

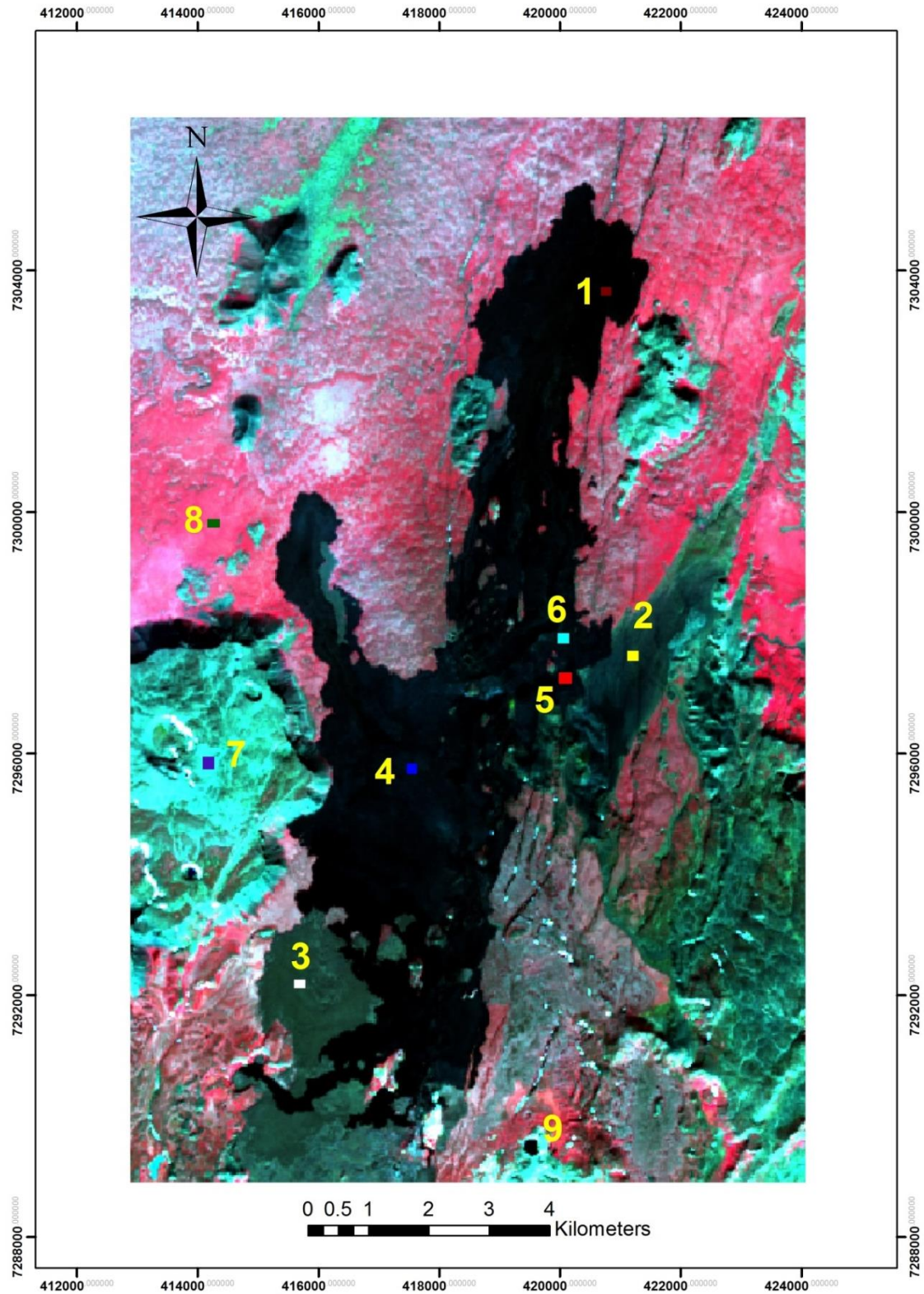


Fig. 35 Spectral endmember points were collected from Landsat 8 OLI False color (7-4-6), area : (1) Rubbly AA; (2) sandur deposit; (3) Old Lava; (4) Pahoehoe; (5) Cauliflower AA; (6) Shelly Pahoehoe; (7) Upper Pleistocene formation; (8) Vegetation; and (9) Water.

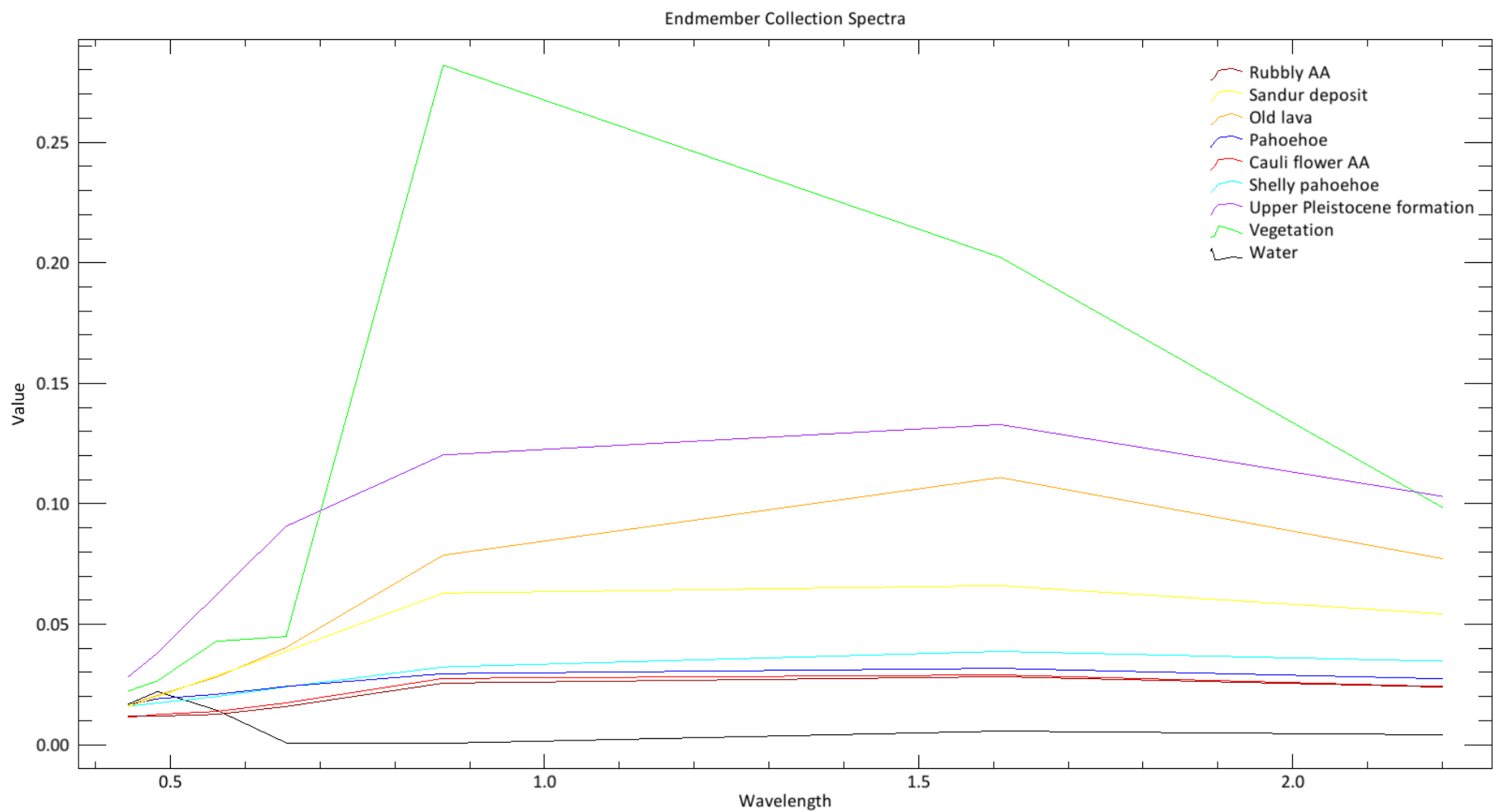


Fig. 36 Landsat 8 OLI spectral reflectance curve from nine endmember points in the Krafla area.

4.3.4 Hyperspectral Image

Due to the success of multispectral sensing, researchers developed hyperspectral sensors to sample the expanded reflectance range of the electromagnetic spectrum, which extends from the visible region (0.4 to 0.7 μm) through the SWIR (about 2.5 μm) in hundreds of narrow contiguous bands about ten nanometers wide (Shaw & Burke, 2003). Mostly of hyperspectral sensors operate over the VNIR/SWIR bands, exploiting solar illumination to detect and identify materials on the basis of their reflectance spectra (Shaw & Burke, 2003) (Fig. 37).

4.3.5 EO-1 Hyperion Pre-Processing

We used the 17th of July 2012 EO-1 Hyperion image, with a hyperspectral band (242 bands) and 30 meter resolution. the Hyperion image was geocoded by using Ground Control Points (GCP) taken from the aerial photograph and georeferenced into the Lambert Conformal Conic coordinate system on the ISN 1993 Lambert 1993 datum.

Eliminating uncalibrated bands and bad bands

The first step of the Hyperion data pre-processing consisted of eliminating uncalibrated bands. The Level 1 Radiometric product has a total of 242 bands, but only 198 of these are calibrated (Amici, Piscini, & Neri, 2014). In this image there are only 170 bands selected due to uncalibrated bands, bad bands and vertical stripping bands (explanation in next section). The several bands are already set to values of zero and the other bands in this image have severe noise that corresponds to strong water vapour absorption; these bands are typically removed from processing (Table 6).

Table 6. List of bad bands on the EO-1 Hyperion image.

Bad bands (Zero value)	Bad bands (strong water vapor absorption)
1-8	121 – 126
58 – 77	167 – 180
225 – 242	222-224

Vertical stripping filtering

Some of Hyperion's detectors are malfunctioning, which often results in vertical striping in the image across all bands (Amici et al., 2014). The striping effect was overcome by removing the band that has a very high stripe and also by using SPEAR Vertical Stripe Removal that provides by Envi® 5.1 . The process of this tool is to filter bright and dark pixels using a mask in order to reduce this noise. The darkest and brightest 5% of the image will be masked by default. Dark pixels are displayed as blue and bright pixels as red (Fig. 38). The red and blue percentages can be modified to include more or fewer pixels in the mask.

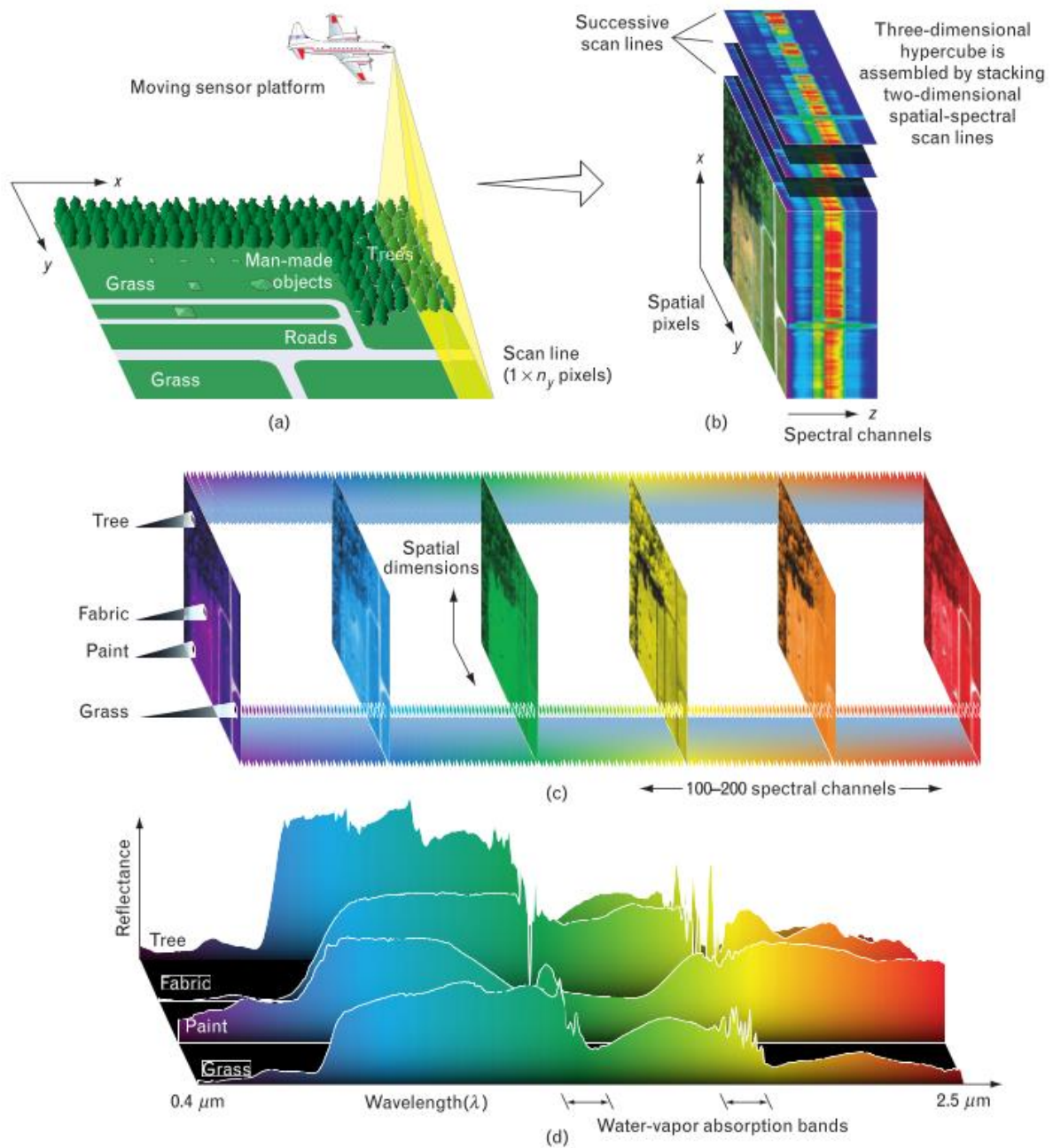


Fig. 37 The hyperspectral data cube structure. (a) Scan line: a push-broom sensor on an airborne or spaceborne platform collects spectral information for a one-dimensional row of cross-track pixels (b) Successive scan lines covered of the spectra for each row of cross-track pixels are stacked to acquire a three-dimensional hyperspectral data cube. Spatial information of a scene is represented by the x and y dimensions of the cube and the amplitude spectra of the pixels are projected into the z dimension. (c) The collected three-dimensional hyperspectral data cube presented as a stack of two-dimensional spatial images, each corresponding to a specific narrow waveband. A hyperspectral data cube usually contains of hundreds of such stacked images. (d) Spectral reflectance curves plotted for each material. Adapted from Shaw and Burke (2003).

There are several vertical stripping appear on the image. The major stripping appears on bands 121-129, 181 and 195. Minor vertical stripping also appears on bands 8-35, 181-221. Fig. 38 shows the vertical stripping on the Hyperion image on Band 125 and 221. Because too

many bands feature vertical stripping, not all bands were removed, because it would lead to a decrease in the spectral range. Only the three worst bands were removed, these are 125, 181 and 195. The rest of bands were filtered by SPEAR Vertical Stripe Removal. Although it does not completely remove the vertical stripping in all bands, the result is much better and reduces the vertical stripping. Fig. 39 shows the result band 221 before and after filtering.

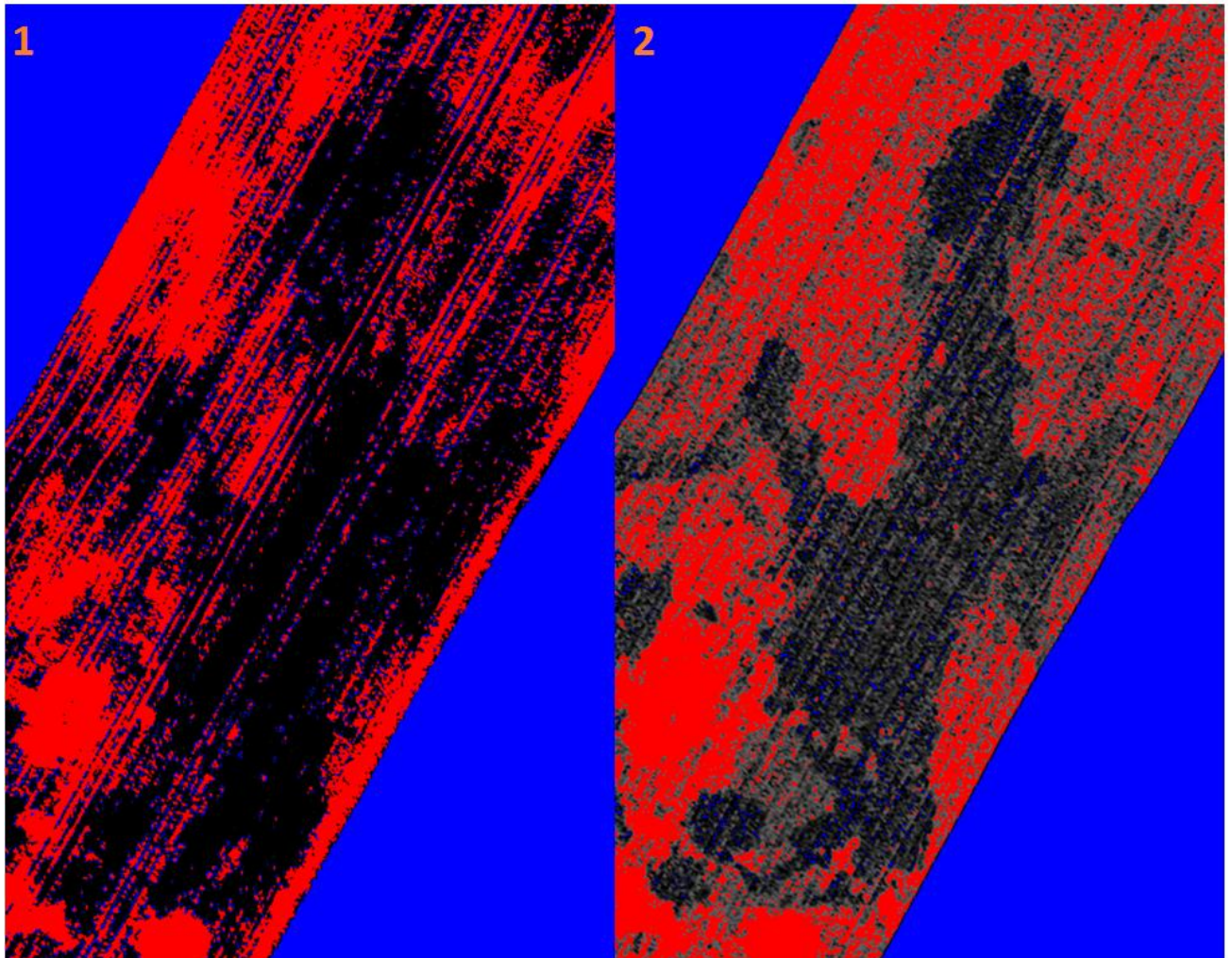


Fig. 38 Example of vertical strip that appear on the EO-1 Hyperion band image (1) Band 125 and (2) Band 221.

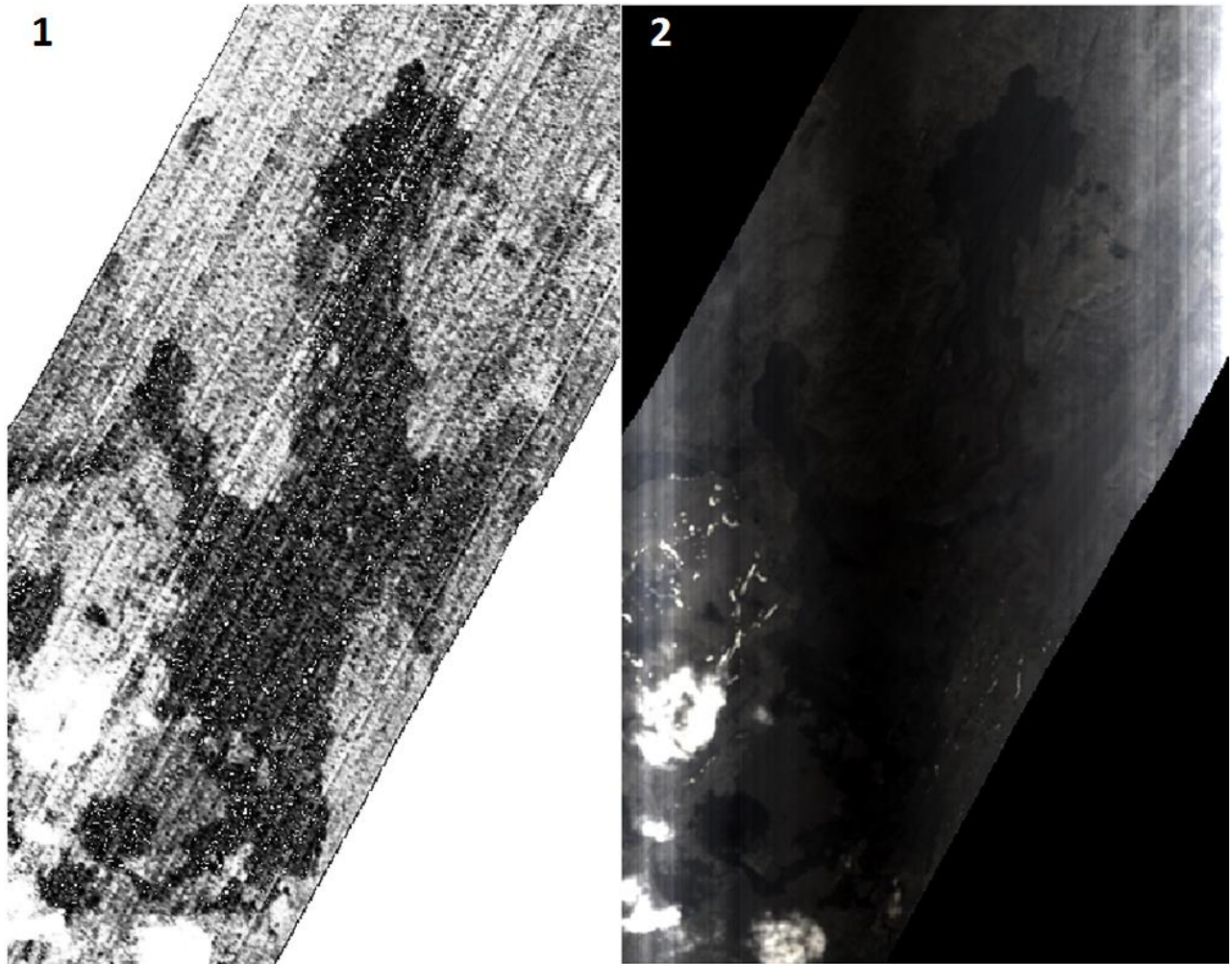


Fig. 39 Hyperion image band 221; (1) before filtered by SPEAR Vertical Stripe Removal; (2) after filtered by SPEAR Vertical Stripe Removal.

Conversion to Surface Reflectance using Fast Line-of-sight Atmospheric Analysis of Spectral Hypercubes (FLAASH)

Surface reflectance of Hyperion was retrieved using the Fast Line-of-sight Atmospheric Analysis of Spectral Hypercubes (FLAASH) algorithm which is developed in FLAASH ENVI module (EXELIS, 2004; Amici et al., 2014). FLAASH is basically an atmospheric correction tool that corrects wavelengths in the visible through near-infrared and shortwave infrared regions, up to 3 μm (EXELIS, 2004).

Unlike many other atmospheric correction programs that interpolate radiation transfer properties from a pre-calculated database of modeling results, FLAASH incorporates the MODTRAN4 radiation transfer code (EXELIS, 2004). Fig. 40 shows a schematic flow FLAASH code. The parameters for ENVI FLAASH include entering information about the type of sensor and the date of scene, selecting an atmosphere and aerosol model for the correction, and setting the options for the atmosphere correction model (Fig. 41).

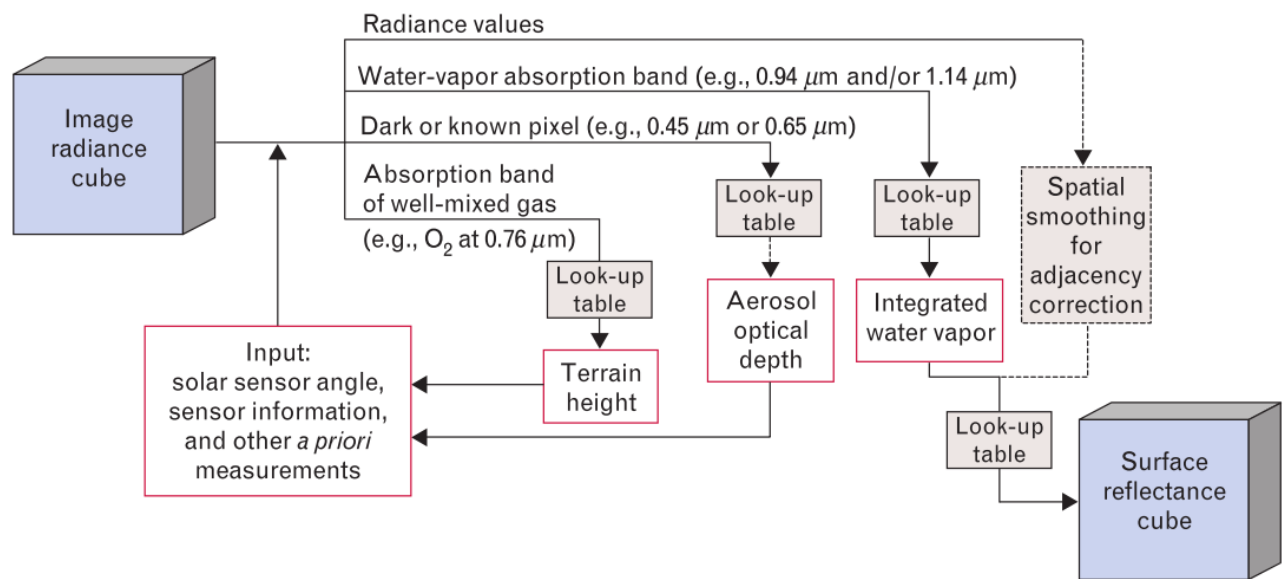


Fig. 40 Schematic flow FLAASH code showing basic steps involved in radiance to reflectance conversion (Shaw & Burke, 2003).

The screenshot shows the 'FLAASH Atmospheric Correction Model Input Parameters' dialog box. The 'Input Radiance Image' is set to 'H:\Desktop\Bahan Thesis MSc\Lava mapping\Geology of Iceland\Krafla\Test 2\Hyperspectral\New Process\T'. The 'Output Reflectance File' is set to 'H:\Desktop\Bahan Thesis MSc\Lava mapping\Geology of Iceland\Krafla\Test 2\Hyperspectral\New Process\F'. The 'Output Directory for FLAASH Files' is set to 'H:\Desktop\Bahan Thesis MSc\Lava mapping\Geology of Iceland\Krafla\Test 2\Hyperspectral\New'. The 'Rootname for FLAASH Files' is empty. The 'Scene Center Location' is set to 'DD <-> DMS'. The 'Sensor Type' is 'HYPERION'. The 'Flight Date' is 'Jul 17 2012'. The 'Flight Time GMT (HH:MM:SS)' is '12:37:32'. The 'Sensor Altitude (km)' is '705.000'. The 'Ground Elevation (km)' is '1.000'. The 'Pixel Size (m)' is '30'. The 'Atmospheric Model' is 'Sub-Arctic Summer'. The 'Aerosol Model' is 'Rural'. The 'Spectral Polishing' is 'Yes'. The 'Water Retrieval' is 'Yes'. The 'Aerosol Retrieval' is '2-Band (K-T)'. The 'Width (number of bands)' is '9'. The 'Water Absorption Feature' is '1135 nm'. The 'Initial Visibility (km)' is '40.00'. The 'Wavelength Recalibration' is 'No'. The 'Apply', 'Cancel', and 'Help' buttons are at the bottom left. The 'Hyperspectral Settings...', 'Advanced Settings...', 'Save...', and 'Restore...' buttons are at the bottom right.

Fig. 41 Parameters for ENVI FLAASH which used in this method.

Sub-Arctic Summer Atmospheric model was used in order to characterize the water vapour present in the atmosphere. The aerosol type selected was the rural one in accordance with the

Krafla scenario, not strongly affected by urban or any other industrial sources. The rest of parameters are selected by default regarding to EXELIS (2004). After applying FLAASH there were problems found on the image scene. A horizontal strip appeared on the centre of the image which caused brightness degradation between those two horizontals as shown in Fig. 42. It could be due to noise that corresponds to very strong water vapour absorption from several bands and also vertical striping filtering.

4.3.6 EO-1 Hyperion spectral endmember selection

The reflectance spectra was obtained from the selected area according to the previous method. Eight spectral ranges were collected in this image. Water spectral was not obtained in this image because there is no water present the area. These eight spectral endmember samples are shown in Fig. 43 and 44. Due to the horizontal strip after the FLAASH process, endmember collections also consider the mixing pixel between degraded brightness and not degraded which are applied in shelly pahoehoe, sandur deposit and vegetation (Fig. 43.2, 43.5 and 44.8). This was done in order to prevent huge differences in spectral signature between these horizontal strips.

4.3.7 EO-1 Hyperion spectral smoothing

Fig. 45a shows eight spectral curves which were obtained from Hyperion image with reflectance values below zero. This is due to bad bands (zero value, high water absorption and vertical stripping). In order to handle this, data was smoothed by using moving average. According to Sun (2010) moving average (spectral low pass filtering) is the most common way to smooth random noise from hyperspectral data. Theoretically, a low pass filter preserves the local means and smooth the input data signal. This low pass filter has a window size of an odd number and is running a moving average along the wavelength for each pixel based on:

$$Y_i^* = \frac{\sum_{i=-m}^m Y_{j+i}}{N}$$

Where Y_i^* is smoothed data at wavelength j , j is also the center location of smoothing operation, $N = 2m + 1$ is the window size, m is half of windows size minus 1, and Y_{j+i} is the data point at band $j + i$ within the window (Sun, 2010). It can be seen in the equation that the larger the window the more smoothing of data. In this study the size of each window is 9 for optimal smoothing according to Heitschmidt et al (2007). Figure 45b shows the spectral result after moving average smoothing.

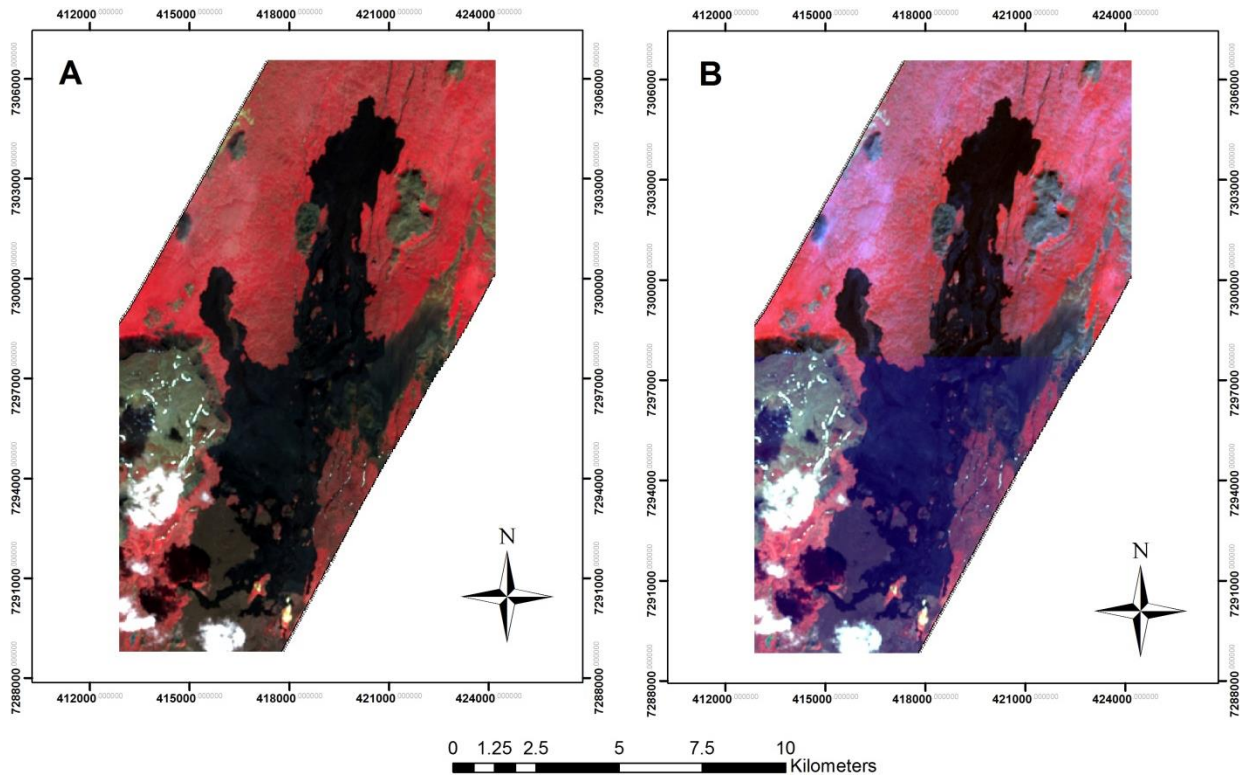


Fig. 42 EO-1 Hyperion false colour composite (46-33-20): (a) before applied FLAASH module; (b) after applied FLAASH module, there were horizontal strip which causes brightness degraded.

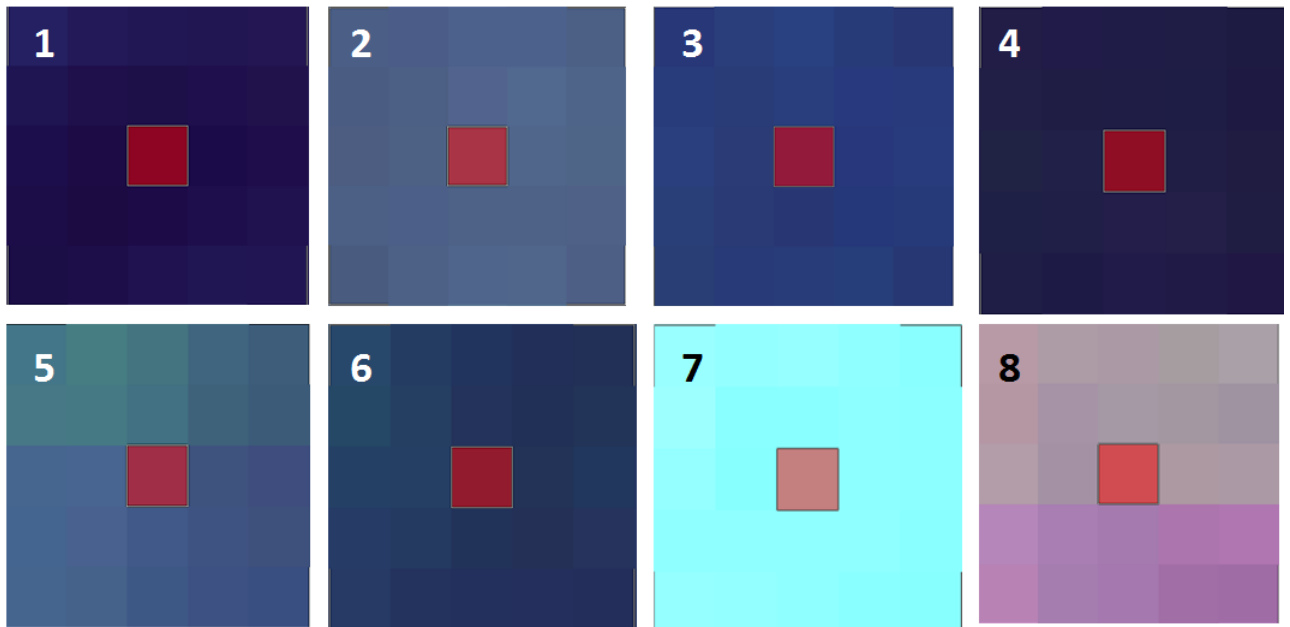


Fig. 43 Eight spectral endmember were collected from EO-1 Hyperion of Krafla area : (1) Caulflower AA; (2) Old lava; (3) Pahoehe; (4) Rubbly AA; (5) Sandur deposit; (6) Shelly Pahoehe; (7) Upper Pleistocene formation; and (8) Vegetation.

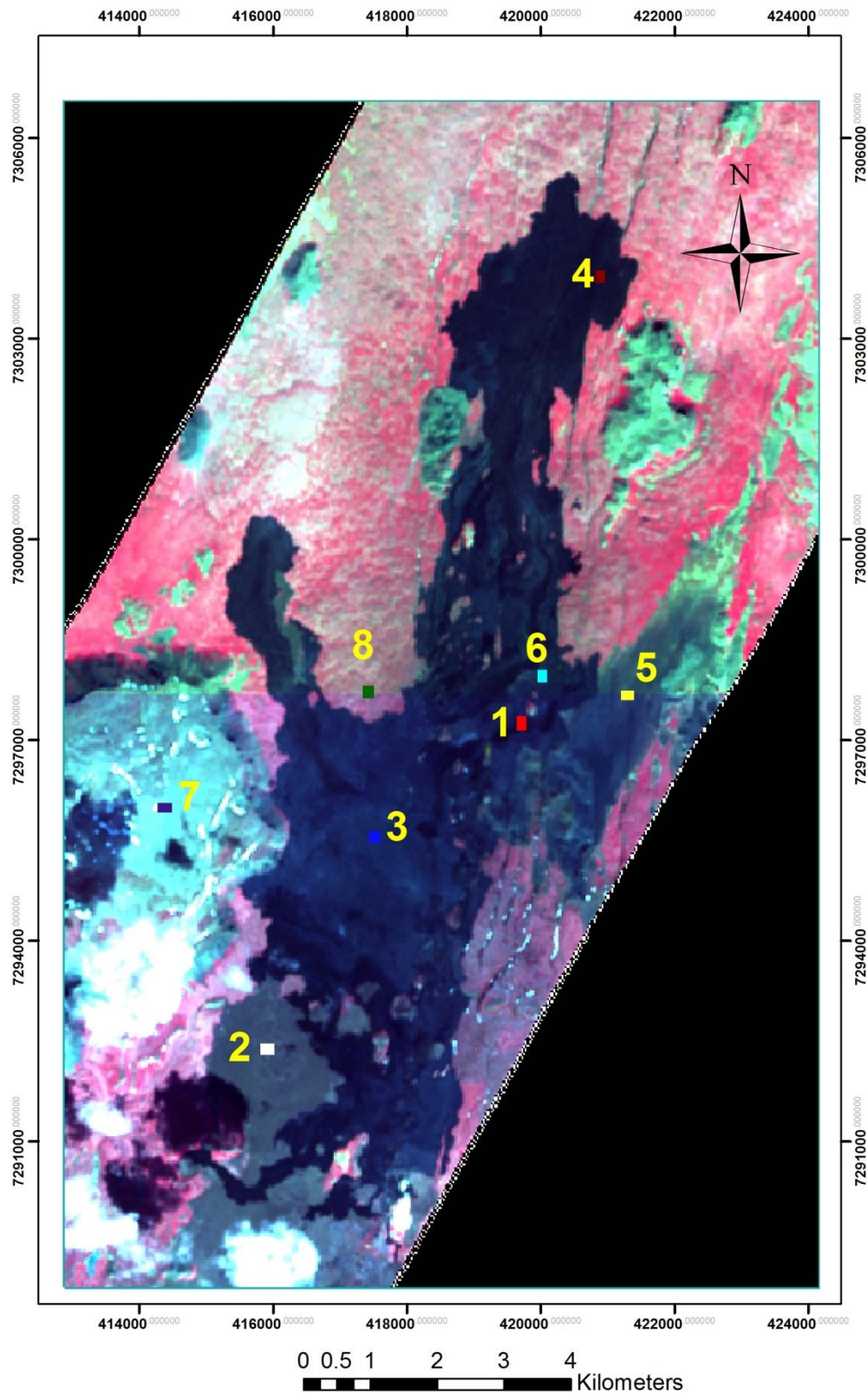


Fig. 44 Eight spectral endmember points were collected from EO-1 Hypeiron of Krafla area : 1) Caulflower AA; (2) Old lava; (3) Pahoehe; (4) Rubbly AA; (5) Sandur deposit; (6) Shelly Pahoehe; (7) Upper Pleistocene formation; and (8) Vegetation.

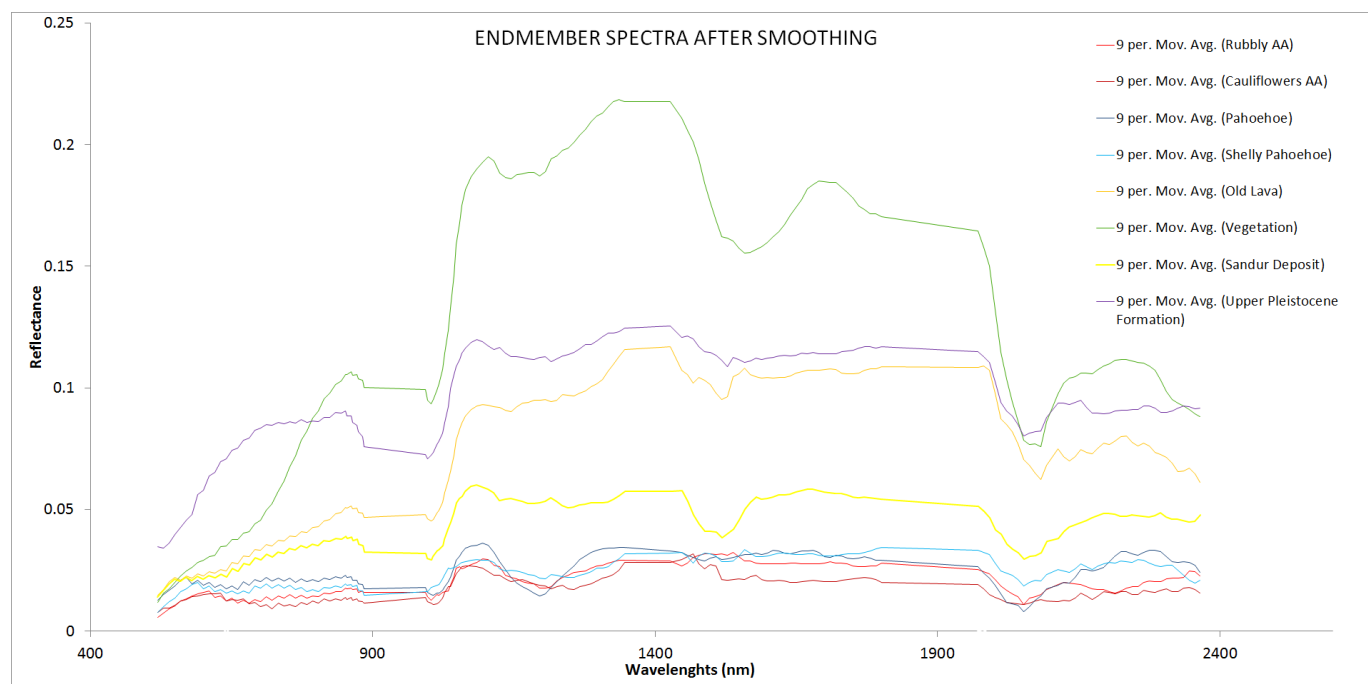
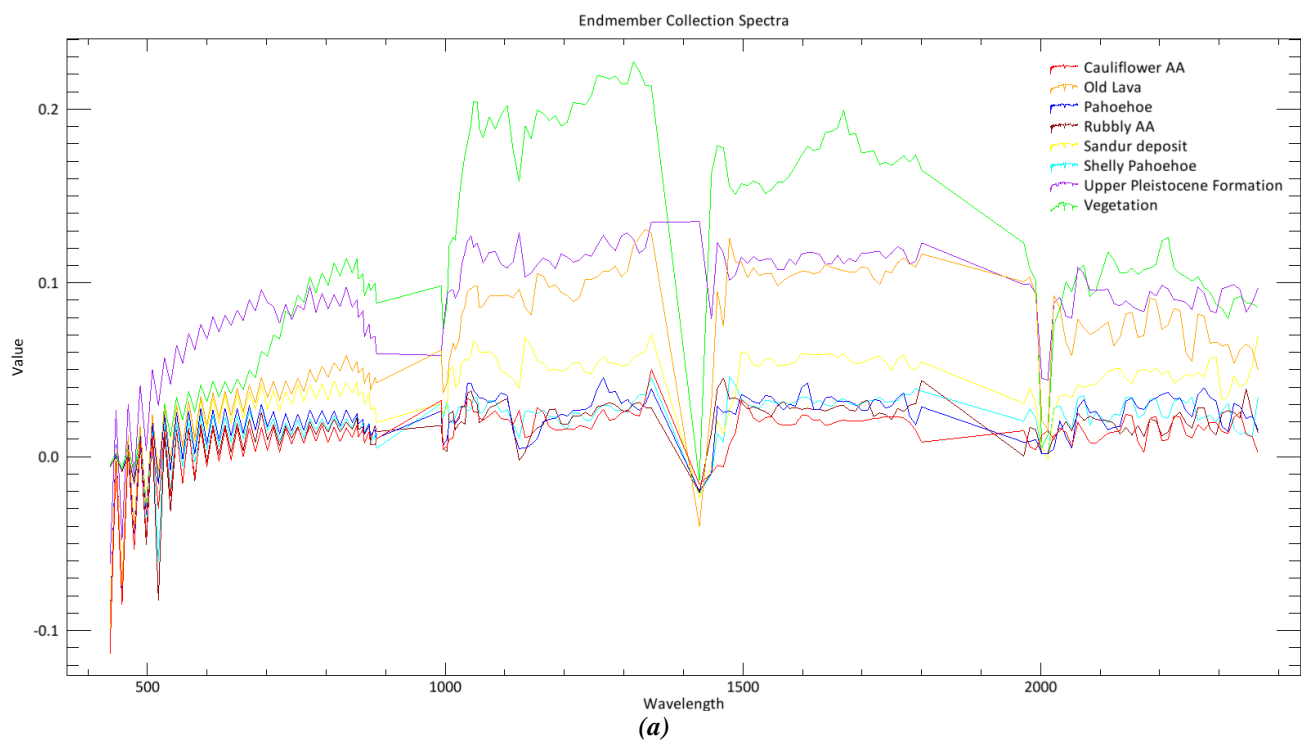


Fig. 45 EO-1 Hyperion spectral reflectance curve from nine endmember points in the Krafla area; (a) before smoothing; (b) after moving average smoothing.

4.3.7 Spectral Angle Mapper (SAM) classification

This method will classify and produce a map from the endmember spectra, as well as maximum likelihood classification, SAM classification, and supervised classification. The SAM classification was done in ENVI for both Landsat 8 OLI and EO-1 Hyperion. The parameters for SAM include the value of angles in radians. Smaller the angles will make SAM search exactly similar spectra. It causes some vegetation to be not detected due to the very different spectra. In order to handle that, on multispectral we assign 0.9 radians for the vegetation and the rest 0.1 radians (Fig. 46a). On hyperspectral, we assign sandur deposit 0.2 radians, shelly pahoehoe 0.3 radians, Upper Pleistocene formation 0.5 radians, and the rest 1 radian (Fig. 46b). These special values also assign due to mixture of the spectral.

The Spectral Angle Mapper (SAM) is a classification method which calculates the spectral similarity between the image reflectance spectrums to reference reflectance spectra (Girouard & Bannari, 2004). The reference spectra can be obtained from laboratory, field measurements or extracted directly from the image. In this method the spectral reference is extracted directly from the image endmember selection. The principle of SAM is to treat the two spectra as vectors in n -dimensional space and calculate the angle between them (Girouard & Bannari, 2004; Rashmi, Addamani, & Ravikiran, 2014). Small angles between them indicate high similarity and high angles indicate low similarity (Girouard & Bannari, 2004).

Solar illumination factors not affected by this method, because the angle between the two vectors is independent of the vectors length. It takes the arc cosine of the dot product between the test spectrums " t " to a reference spectrum " r " with the following equation (Amici et al., 2014):

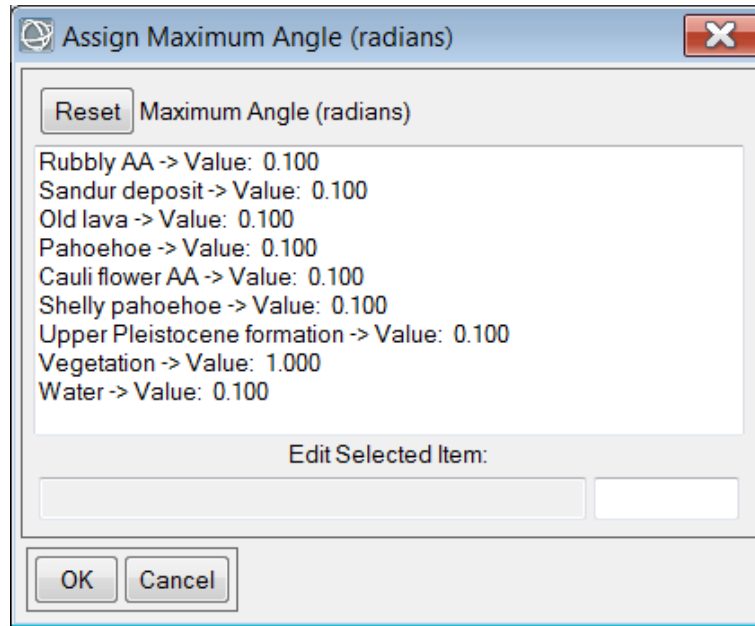
$$\alpha = \cos^{-1} \left(\frac{\sum_{i=1}^{nb} t_i r_i}{(\sum_{i=1}^{nb} t_i^2)^{1/2} (\sum_{i=1}^{nb} r_i^2)^{1/2}} \right)$$

nb = the number of bands

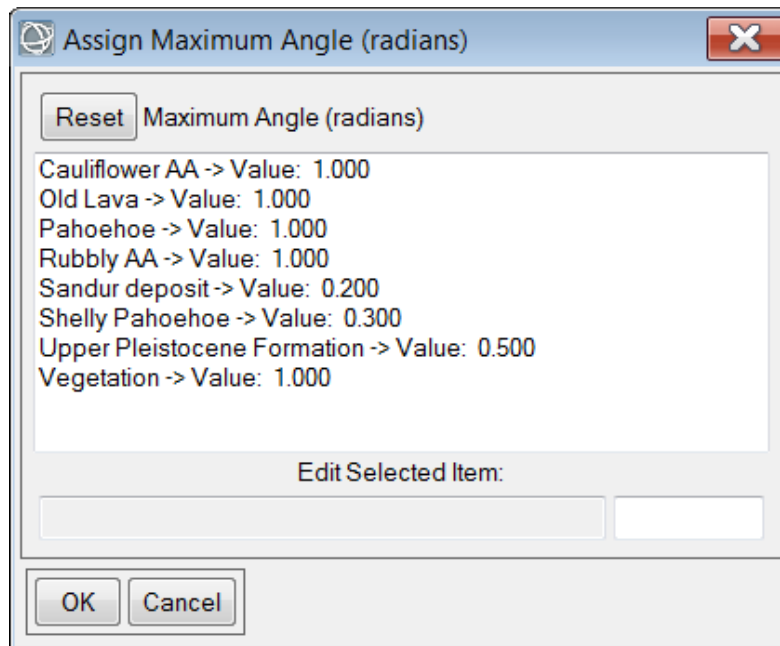
t_i = test spectrum

r_i = reference spectrum

The main advantage of the SAM algorithm is the easy and powerful classification of morphologies by mapping the spectral similarity of image spectra to reference spectra. This is because this method resists the influence of shading effects to accentuate the target reflectance characteristics (Amici et al., 2014). The main disadvantage of this method is the spectral mixture problem. The most erroneous assumption made with SAM is the supposition that endmembers chosen to classify the image represent the pure spectra of a reference material. This problem generally happens with medium spatial resolution images, such as Landsat 8 OLI and EO-1 Hyperion.



(a)



(b)

Fig. 46 (a) Maximum angles parameters for Landsat 8 OLI; (b) maximum angles parameters for EO-1 Hyperion.

4.4 Accuracy Assessment

This method will assess the accuracy of maps that have been produced comparing with the reference points. The accuracy assessment shows the percentage difference between classification result and references data. This study uses as references data the existing lava morphology from Rossi (1997) combined with aerial photography and SPOT 5 panchromatic as mentioned on section 4.1. Selection of 150 (30 each class) reference sites were based on random equal-stratified sampling which are generated on section 4.1.2. Fig. 47 shows the reference points within classified satellite images. All the images were masked to show only Krafla lava field area to minimize other areas impacting on this accuracy assessment. This assessment was processed in ERDAS using 150 references data points. The results of an accuracy assessment are usually summarized in a confusion matrix as shown in Table 7 below:

Table 7: Example of confusion matrix

		References Points			No. Classified Pixel
		Aa	Pahoehoe	Non Lava	
Classified Satellites Image	AA	2900	500	100	3500
	Pahoehoe	100	2000	100	2200
	Non Lava	0	500	2800	3300
No. References Point		3000	3000	3000	9000

A measure for the overall classification accuracy can be derived from this table by counting how many pixels were classified the same in the satellite image and on the reference and dividing this by the total number of pixels. According to this table we can estimate overall accuracy is 85.5% but this measure does not describe how well individual classes were classified.

The user and producer accuracy are two widely used measures of class accuracy. The producer's accuracy refers to the probability at this case certain surface morphology area on the ground is classified as such, while the user's accuracy refers to the probability that a pixel labelled as a certain surface morphology class in the map is really this class. As an example from Table 7, for pahoehoe the user accuracy is $\frac{2000}{2200} = 90.9\%$ and for producer accuracy is $\frac{2000}{3000} = 66.7\%$. It means as a user, we can assume that roughly 90.9% of all the pixels classified as pahoehoe are definitely pahoehoe on the surface and as a producer; only 66.7% pahoehoe pixels were classified.

The other important part of the assessment is the Kappa statistics. Kappa is another measure of the accuracy of the classification. Kappa reflects the measurements of agreement between classifications model and reality (Congalton, 1991) or to determine if the values contained in an error matrix represent a result significantly better than random (Jensen, 1996). According to (Jensen, 1996) Kappa is calculated as:

$$\kappa = \frac{N \sum_{i=1}^r x_{ii} - \sum_{i=1}^r (x_{i+} * x_{+i})}{N^2 - \sum_{i=1}^r (x_{i+} * x_{+i})}$$

Where N is the total number of sites in the matrix, r is the number of rows in the matrix, x_{ii} is the number in row i and column i , x_{+i} is the total for row i , and x_{i+} is the total for column. Kappa for the confusion matrix shown in Table 7 would be calculated as:

$$\kappa = \frac{(9000 * (2900 + 2000 + 2800)) - ((3500 * 3000) + (2200 * 3000) + (3300 * 3000))}{9000^2 - ((3500 * 3000) + (2200 * 3000) + (3300 * 3000))}$$

According to the example, the result of Kappa statistics is 0.783. Kappa of 0.783 means there is 78.3% better agreement than by chance alone. Kappa statistics values range from 0 to 1, though they can be negative and range from -1 to 1. However, since there should be a positive correlation between the remotely sensed classification and the reference data, positive Kappa values are expected (Congalton, 1991). In general, there is not a standardized interpretation of the Kappa statistic (e.g Congalton, 1991; Carletta, 1996; Banko, 1998). In this interpretation we will use the value from Congalton (1991). Typically, a perfect classification would produce a Kappa value of one, values greater than 0.80 (i.e, 80%) represent strong agreement between the remotely sensed classification and the reference data, while values between 0.4 and 0.8 represent moderate agreement (Congalton, 1991). Anything below 0.4 is indicative of poor agreement (Congalton, 1991).

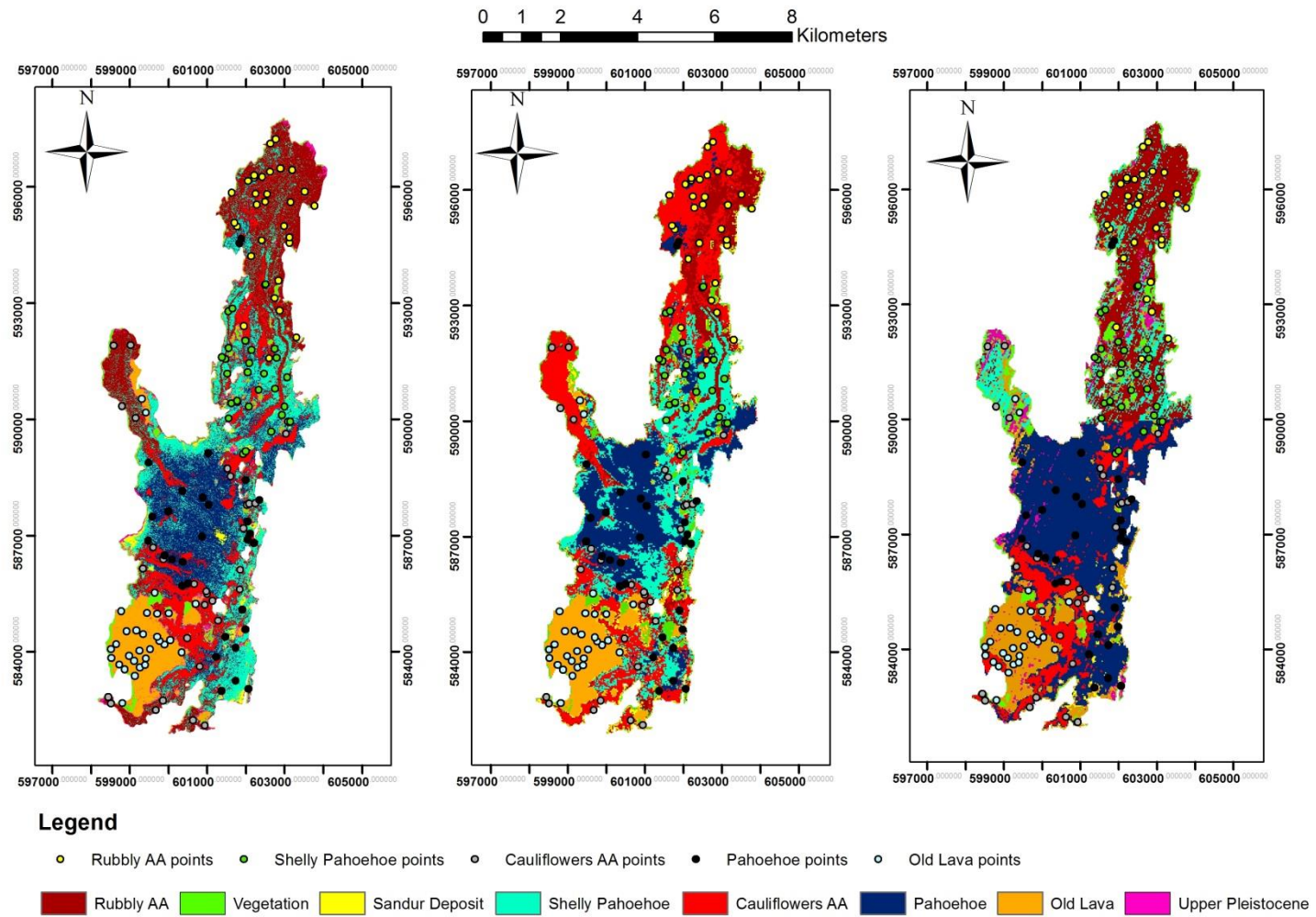


Fig. 47 Reference points overlay in (a) SPOT 5 classification; (b) Landsat 8 OLI classification; (c) EO-1 Hyperion classification.

5 Analysis and Results

5.1 Lava Morphology Visual Interpretation

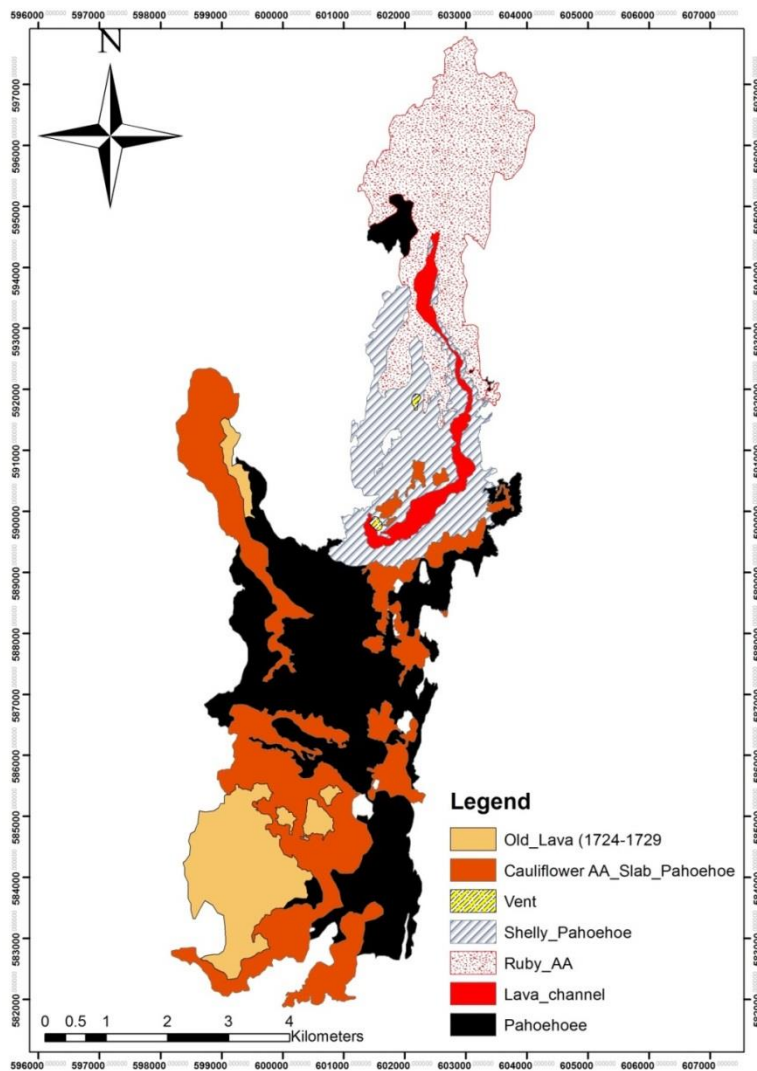


Fig. 48 Surface morphology of Krafla based on visual image interpretation.

percentage between pahoehoe and aa are relatively balance, 48.7% is pahoehoe and 47.9% is aa.

Since the resolution of the aerial photograph is very high (0.5 m) there are some advantages and the disadvantages for this interpretation. The main advantages of the interpretation from very high resolution are that it is very easy to distinguish between aa and pahoehoe on the surface (Fig. 7a, 7b, 7c, 7d, 7e), since aa morphology is relatively rough and darker than pahoehoe. The main disadvantages are that it is tricky to interpret the small patches of morphology as seen in Fig. 49, shows the cauliflower aa which have the size about 360 m², it is relatively smaller than others with similar morphology and also these found in other

The result map from the visual image interpretation show a total of seven classes (1) Rubbly aa; (2) old lava (1724-1729) (3) cauliflower aa and slabby pahoehoe; (4) pahoehoe; (5) shelly pahoehoe; (6) lava channel and (7) lava vent (Fig. 26). Only five classes were used for accuracy assessment (cauliflower aa, shelly pahoehoe, rubbly aa, shelly pahoehoe and old lava). The result on Fig. 48 shows that combination of the image success to generate detail lava surface morphology map of Krafla lava field. According to the map that was generated in the interpretation, the lava covered about 36.9 km² (excluding older lava and vents) with 33.7% classified as pahoehoe, 27.3% as cauliflower aa, 15.1% as shelly pahoehoe, 20.6% as rubbly aa and the remaining 3.3% as lava channel. While in overall

morphology besides cauliflower aa. According to that we could exclude those small patches from the map. It would influence the accuracy assessment if we included this on the map, since Landsat and Hyperion only have 30 meters resolution, so neither of these satellites could detect these small patches.

Both spatial and temporal problems occur in this lava surface morphology map, leading to misinterpretation. For spatial issues there is missing lava seen in the north part of the aerial photograph (Fig. 21a, 21b). SPOT 5 panchromatic (2.5 meters resolutions) and open channel lava morphology from Rossi (1997) were used to fill the north part of the aerial photograph, but the resolution of this satellite and map is different from aerial photograph which caused missing details of surface morphology of lava such as brightness, detail of lava and colours. Ideally if we were to fill the missing scene, the same data is recommended (aerial photography). This also leads to a temporal problem, which is that the acquisition times between aerial photograph, SPOT 5 panchromatic and open channel lava morphology were different. Since the aerial photograph were acquired on July 28th, 2012, SPOT 5 panchromatic on October 3rd, 2002, and the map from Rossi (1997) was produced on 1996. It is 10 and 16 years different between two images and the aerial photograph which means it might leads into different scene on the surface because within those years could be some weathering process on the lava field. In the lava surface morphology that was produced in this study it was assumed that there was no change on the lava field.

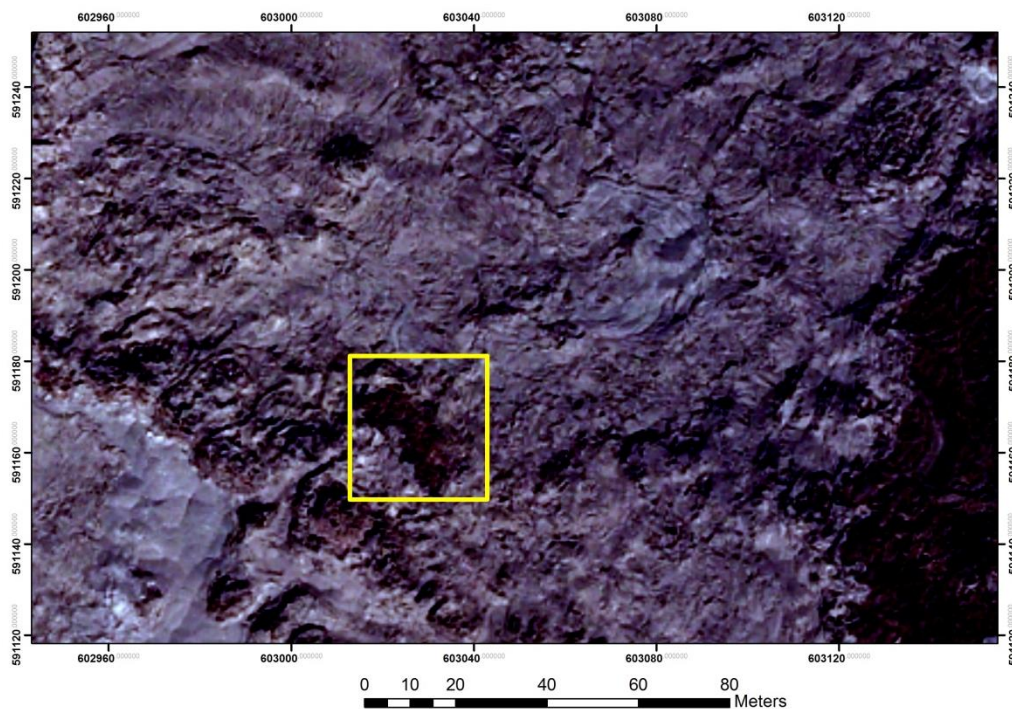


Fig. 49 Small patches of cauliflowers aa appear on aerial photograph (yellow line).

5.2 Lava Morphology Histogram Distributions

As described in chapter 4.1, a lava surface morphology sample was chosen from pixel homogeneity based on the SPOT 5 image and reference map which was produced from aerial photograph. The histograms in Fig. 50 and 51 show the distribution of digital number (DN) from the specified class in the Krafla lava field. According to the histograms there are clearly different characteristics between lava (Fig. 50) and non-lava (Fig. 51). Strictly speaking in Krafla based on SPOT 5, most of the non-lava has relatively symmetric histogram (except water) especially in band 2 (Red) and band 4 (SWIR), while the lava shows the asymmetric histogram, relatively skewed and flat (except in the old lava).

Statistical analysis was performed on the histogram (Table A2). According to these statistics the range of lava pixel intensity from all bands is 12-69: the highest pixel intensity found in the old lava from the Mývatn fires (1724-1729). This is due to weathering process making the reflectance of old lava higher than the latest one (Spinetti et al., 2009). The mean intensity value for lava from the Krafla fires show that the mean pixel intensity increases from band 1 to band 3, then decreases in band 4 as shown in Fig. 52. This characteristic is also found in the sandur deposits and water but lava has a relatively steeper slope than the sandur deposits, while water has very high intensity in the near infrared band (band 3). According to the mean plot in Fig. 52 the pahoehoe type has a higher reflectance than other morphologies but it is tricky to distinguish between pahoehoe sheet and shelly pahoehoe from this mean plot, because the value is not significantly different. As well as aa, we cannot see a significant difference between cauliflower aa and rubbly aa in bands 1 to 3 but on the SWIR band (band 4), the mean pixel intensity of cauliflower aa slightly drops with steeper slope compared to rubbly aa. While in SWIR band rubbly aa has a higher mean pixel compared to pahoehoe type.

Fig. 53 shows the feature space plot band 2 and band 4. There are overlaps between water and lava morphology clusters in feature space plot band 2 / band 4. In order to differentiate between water and lava field, we can analyse the result of space plot band 3 / band 4 because as mentioned before band 3 has a higher pixel intensity for water (Fig. 54). From space plot in band 2 / band 4 is clear that cauliflower aa has values which intersect that of pahoehoe, while in band 3 / band 4 (Fig. 54) shows the cauliflower has less intensity and did not have an intersection with any other lava morphology. Rubbly aa, pahoehoe and shelly pahoehoe have overlapping intensities both in feature space band 2 / band 4 and band 3 / band 4; this might lead to the confusion of classification (Fig. 60).

To overcome overlaps in feature space it needs to be confirmed whether it is possible to differentiate between the classes in question in at least one other feature space. If this is not possible a mathematical algorithm may be able to analyse the differences between similar classes and group them statistically. If this is too not possible then we can take more than one sample class (only include samples of which are 100% sure it represents the lava morphology class).

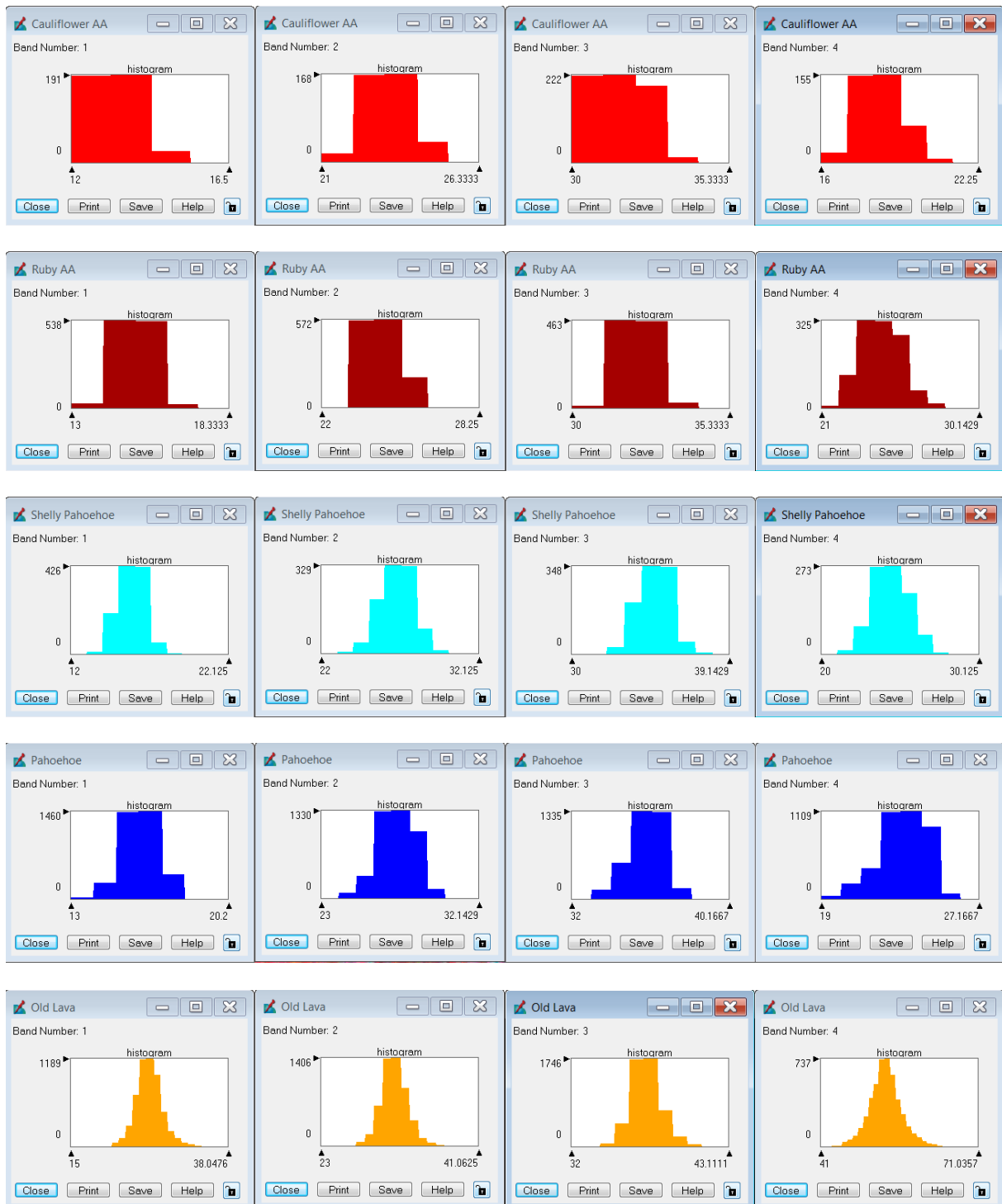


Fig. 50 Pixel histogram distribution of lava morphology in Krafla; (1) Cauliflower AA; (2) Rubbly AA; (3) Pahoehoe; and (5) Old lava.

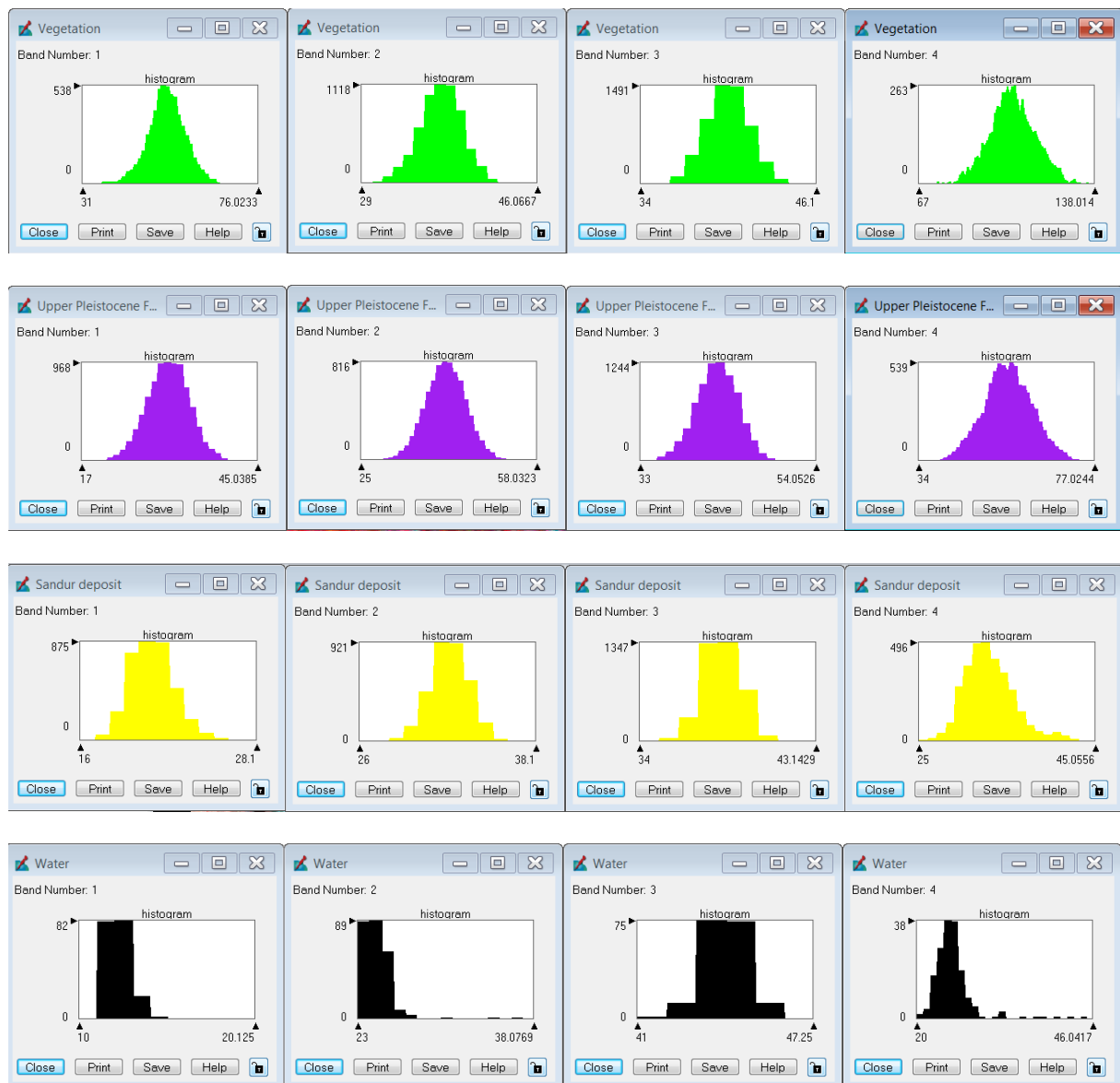


Fig. 51 Pixel histogram distribution of the area outside lava; (1) Vegetation; (2) Upper Pleistocene formation; (3) sandur deposit; and (4) water.

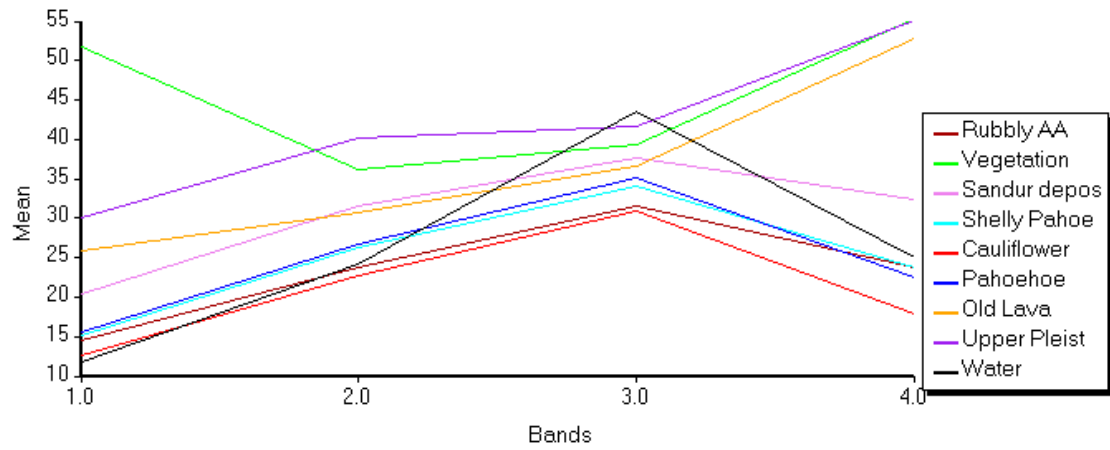


Fig. 52 SPOT 5 Mean pixel intensity plot for all bands in Krafla.

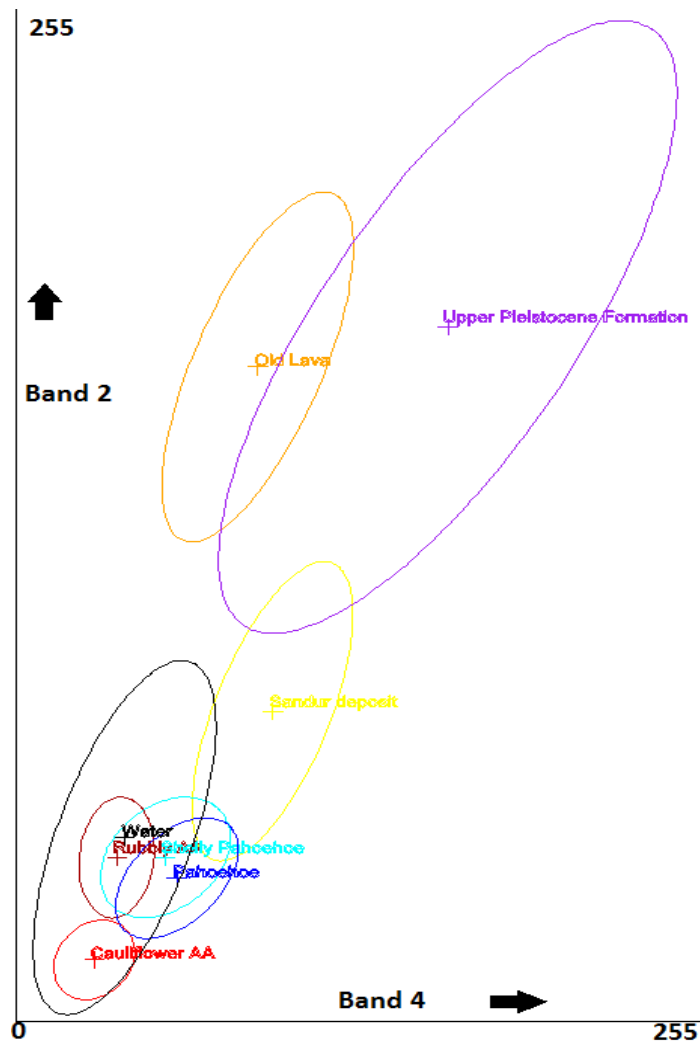


Fig. 53 Feature space plot band 2 / band 4. The circle area is the minimum and maximum value for each cluster and band, and the center of the circle is mean value.

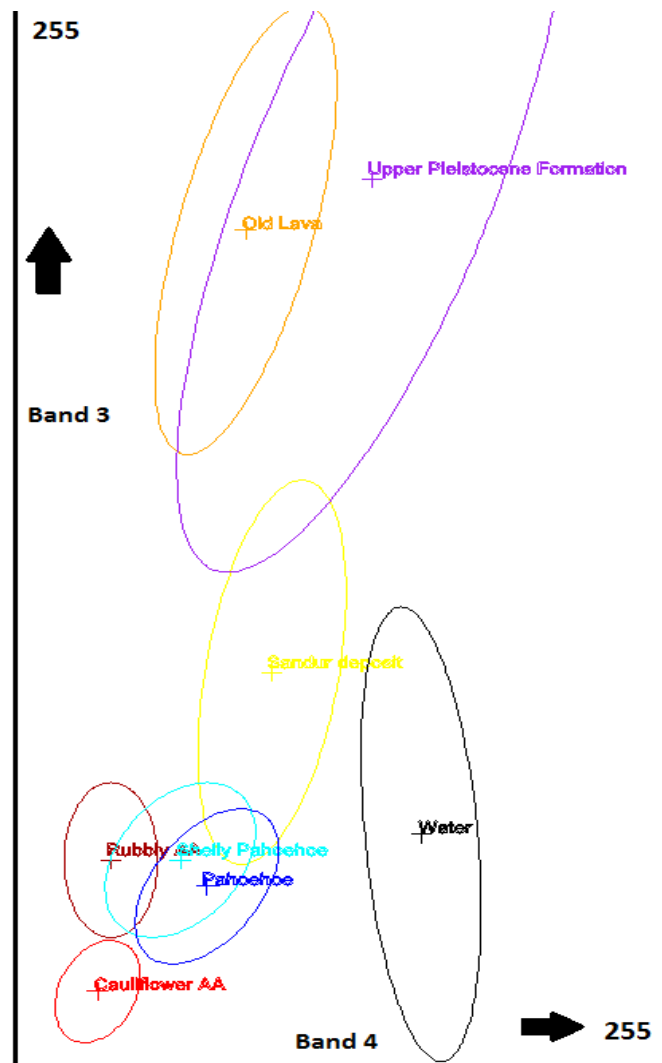


Fig. 54 Feature space plot band 3 / band 4.

5.3 Lava Morphology Spectral Reflectance Analysis

To analyse lava morphology reflectance, seven bands were used in multispectral and 170 bands for hyperspectral. The results indicate that, both multispectral and hyperspectral have higher reflectance in older lava compared to the Mývatn fires (Fig. 56a and Fig. 57), this is due to weathering (Spinetti et al., 2009). Pahoehoe lava has a higher reflectance than aa (Fig. 56s and Fig. 57) because aa has a relatively rough surface which causes diffuse reflection (Timmermans, 1995; Bakx et al., 2012).

Due to the fact that most of the lava in Krafla is basaltic (Rossi, 1997), the basaltic lava spectra was further validated from a laboratory measurement obtained from the USGS and provided in ENVI software. This basalt has the same spectral characteristic CRBG rock

surfaces which have five major absorptions a) Fe^{3+} electronic absorptions in oxides/hydroxides, b) Fe^{2+} electronic absorptions in pyroxene, c) O–H vibrations in hydroxyl, d) H_2O and e) M–OH vibrations in clay minerals (Fig. 55) as explained before in section 2.4.1 by Michalski et al. (2006). This USGS sample of weathered basalt has a higher reflectance and also has relatively strong absorptions in the five bands compared to fresh basalt (Fig. 55).

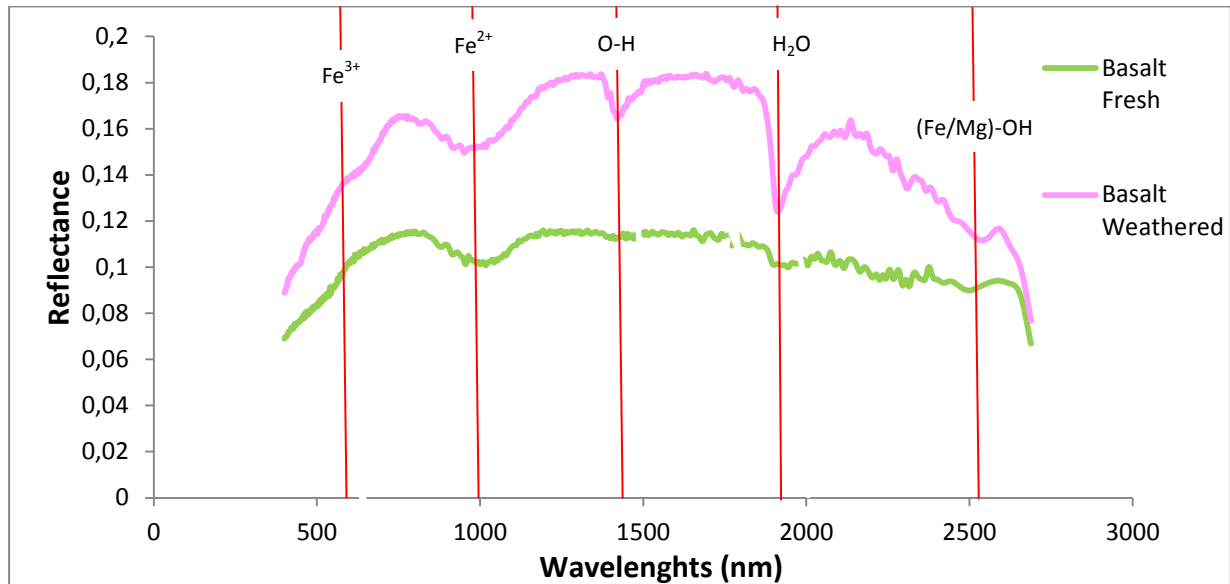
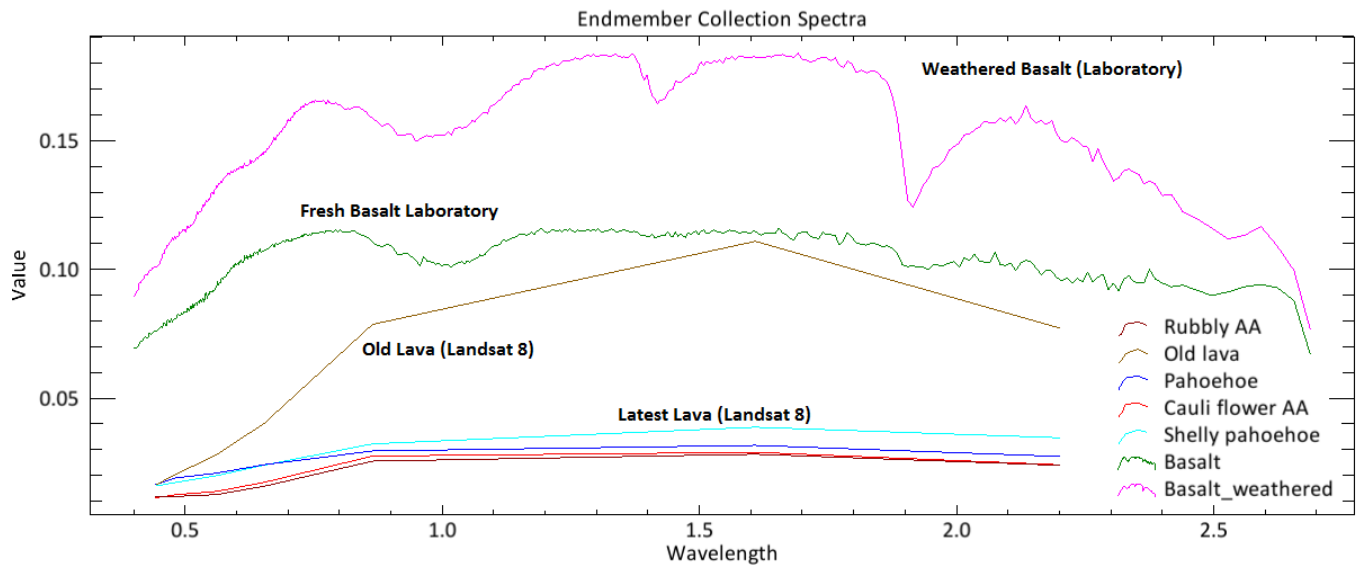


Fig. 55 Spectral reflectance curve of basalt from USGS, red lines show the absorptions features.

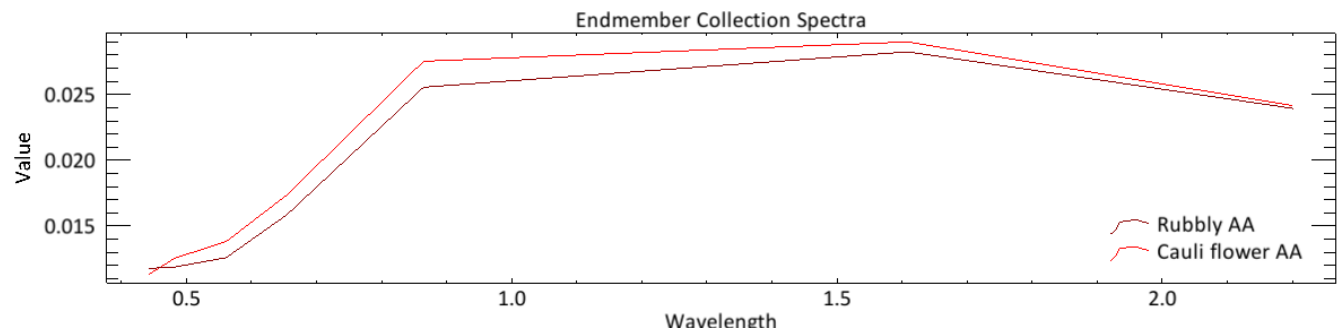
5.3.1 Multispectral reflectance analysis

The overall shape of the lava reflectance curve in the Krafla lava field is similar to that of the basaltic lava from laboratory studies (Fig. 56a), but the reflectance value is different. The main cause of the difference in lava reflectance values between the laboratory and the Landsat images is due to the different basalt sample between the satellite image and the USGS. The spectral slope of weathered lava and old lava are steeper relative to fresh lava. However, due to the band limit of multispectral data, there are so many gaps between spectral ranges that we cannot observe the absorption features in the multispectral data.

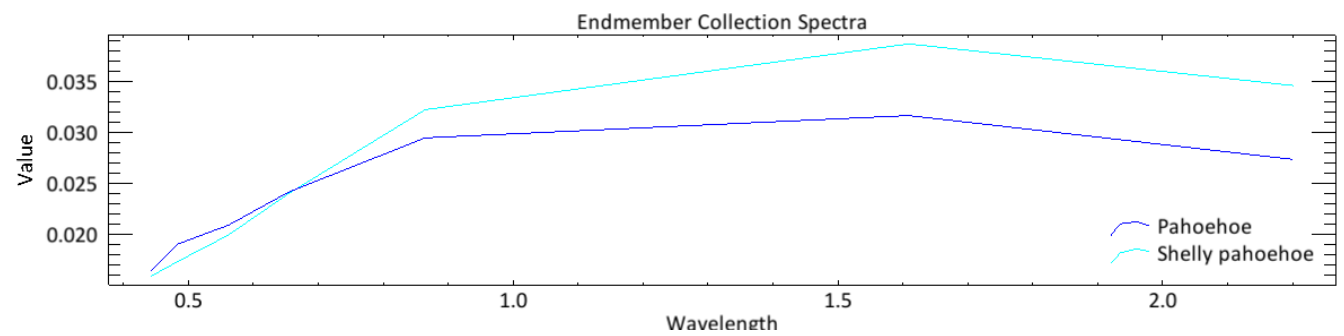
In aa type lava, average reflectance spectra of cauliflower aa has a higher reflectance than rubbly aa (Fig. 56b), but in the band 1 (443 nm) rubbly aa has higher reflectance. The average spectra of pahoehoe type lava shows that shelly pahoehoe has a higher reflectance than pahoehoe sheet. Similarly to rubbly aa, pahoehoe sheet lava has a higher reflectance in the visible band blue and green (443 nm - 590 nm).



(a)



(b)



(c)

Fig. 56 Spectral reflectance of lava morphology comparison; (a) between laboratory measurement and lava in krafla lava field; (b) between cauliflowers aa and rubbly aa; (c) between shelly pahoehe and pahoehe.

5.3.2 Hyperspectral reflectance analysis

The advantage of hyperspectral images is the number of spectral bands that are not offered by multispectral images. Spectral reflectance curves from hyperspectral data of Krafla lava are closer in value to laboratory data than multispectral is (Fig. 57). The results show that the absorption features of the old lava in Krafla are relatively similar to weathered basalt except in (Fe/Mg)-OH absorption ranges due to the limited range of remote sensing data and the shifting of absorptions features (Fig. 57). Shifting of absorption features in hyperspectral data could be due to the effect of data smoothing. Fig 62 show the effect bad data (1820 nm – 1951 nm) cause the flat spectral after data smoothing.

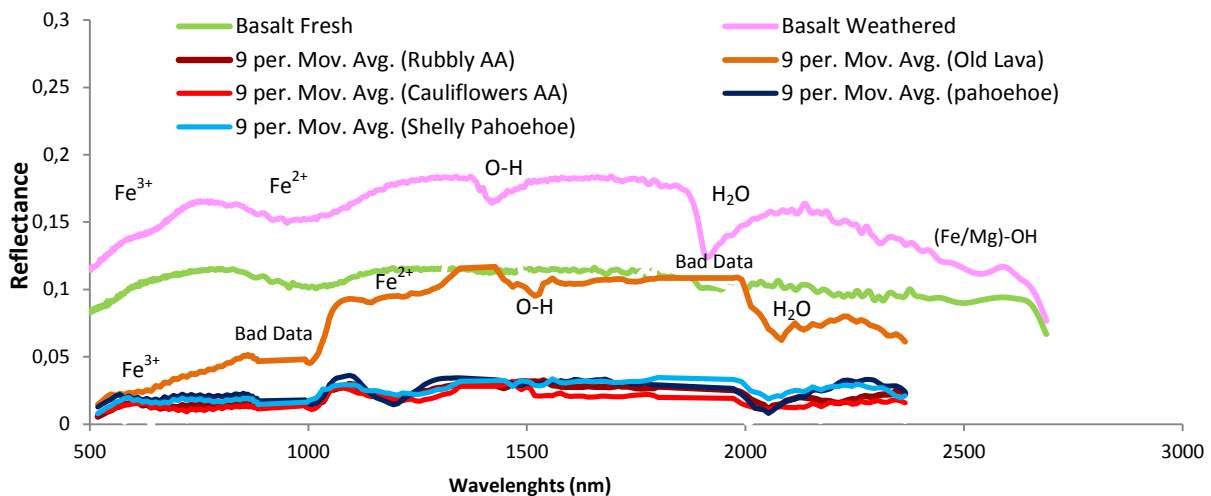


Fig. 57 Spectral reflectance of lava morphology comparison between basalt from USGS laboratory measurement and basalt lava in Krafla lava field from remote hyperspectral remote sensing with the absorptions features.

Cauliflower aa has a higher average reflectance in hyperspectral data than in multispectral. However, aa lava has the same characteristic reflectance shape of fresh basalt in both types of data (Fig. 57). In hyperspectral data, rubbly aa has absorption features in the 2200-2300 nm range (Fig 58), but because there is no spectral reflectance reference for Krafla conclusions cannot be drawn from this data.

The average reflectance spectra between pahoe-hoe and shelly pahoe-hoe show relatively similar shape (Fig. 59). Interestingly, shelly pahoe-hoe has similar spectral absorptions to of aa type lava especially in the Fe^{2+} and H_2O sensitive ranges. (Fig. 59). This could be due to the surface morphology of shelly pahoe-hoe being rougher than pahoe-hoe sheet (Fig 6a, 6b and 7a, 7b). In general, pahoe-hoe has a stronger absorption feature in the Fe^{2+} and H_2O ranges.

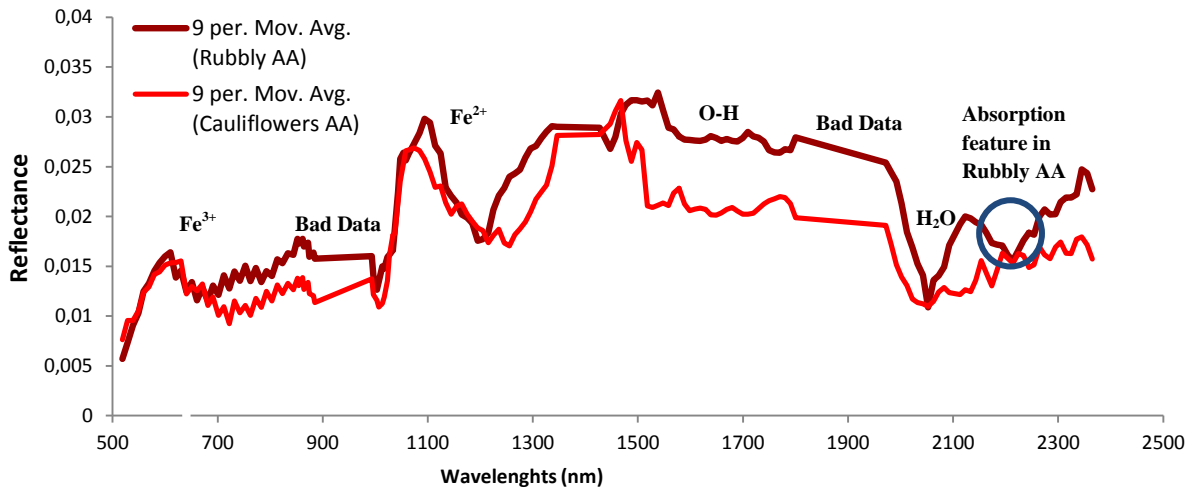


Fig. 58 Spectral reflectance of lava morphology comparison between cauliflowers aa and rubbly aa in Krafla lava field, blue circle show the absorption feature between 2200-2300 nm found in rubbly aa.

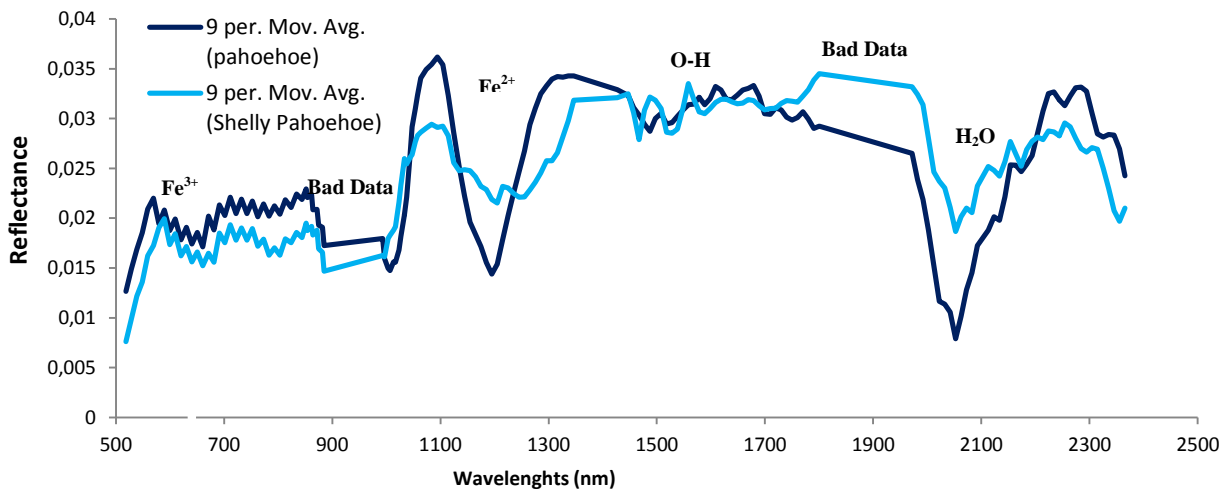


Fig. 59 Spectral reflectance of lava morphology comparison between pahoehoe and shelly pahoehoe in Krafla lava field, in general pahoehoe have stronger absorption feature in Fe^{2+} and H_2O .

However, the above characteristics and absorption features are not necessarily the main spectral reflectance differences between lava morphologies. These spectral variations can be due to several factors, like different mineralogy or composition of lava, quality of hyperspectral image data and the different of basaltic reference. As explained by Van Der Meer (2006) the spectral reflectance is often determined by the mineralogy. These absorption features are controlled by the particular crystal structure in which the absorbing species is contained and by the chemical structure of the mineral (Van Der Meer, 2006). This may lead to different absorption and shape features for each lava morphology. Further analysis of absorptions features such as depth of absorptions and width of absorptions need to be involved as Zaini (2009) has done. During data processing the methods used for smoothing the spectra need to be considered, since it is necessary for spectral variation shape. As suggested in Ruffin and King (1999), the Savitzky-Golay filtering method is a better alternative to the moving average method for smoothing hyperspectral data. Further analysis

of ground truth data of reflectance spectra of the lava field from Krafla is essential in order to validate the Hyperion image and also using airborne hyperspectral image data such as HyMap and AVIRIS could be used to improve the detail of reflectance spectra, since HyMap has between 2 and 10 m per pixel resolutions and at approximately 15 nm spectral resolutions (Zaini, 2009).

5.4 Lava Morphology Classification

There are three lava morphology classification maps were generated. Fig. 60 shows the result of SPOT 5 based on maximum likelihood classification in the Krafla lava field and Fig. 61 shows the result of Landsat 8 OLI and EO-1 Hyperion based on SAM. In this section the effect of training samples and endmember spectral collections to classification will be discussed.

5.4.1 Effect of training samples in classification

In overall classification of SPOT 5 based on pixel analysis show fairly acceptable results. On the other hand, according to statistics of accuracy assessment (Table 8) the classification obtained 67.33% overall accuracy despite of high pixel resolution data. Although this is not a bad result for classification, it can be improved. As mentioned in section 5.2 the training samples have to be 100% sure to represent the lava morphology class. In fact lava morphology classes are combinations of lava materials with various proportions of them. It is difficult to get a “pure” morphology. As mentioned in Rossi (1997), in the Krafla lava field cauliflower aa is often associated with slabby pahoehoe and pahoehoe sheet may or may not contain ropey textures. The assumption of homogeneity leads to the overlapping of feature space for some lava morphologies as seen in figure 58 and 59. Due to the high resolution of SPOT 5, the shadows also occur as noise because they are classified as cauliflower aa (Fig. 60). The classification of area outside the lava field is simple as there is little overlapping in these classes. In order to minimize the overlapping both in classification and feature classes, it is recommended to add more training samples for every lava morphology and also to prevent shadows classified as cauliflowers aa.

5.4.2 Effect of endmember spectral in classification

SAM classification resulted great deal to differentiate detail lava morphology from spectral reflectance especially in hyperspectral. Despite medium resolution and bad quality of data (caused by stripping, brightness degrading and many bad bands), the overall accuracy of hyperspectral classification is 61.33% and has the highest user accuracy (76.47% and 68.57%) when classifying cauliflowers aa and rubbly aa compared to multispectral (33.33% and 60%) and SPOT 5 (59.09% and 66.67%). Although the sample size also influence these percentages as will be discussed below. In order to improve the classification, spectral endmembers have to be collected in-situ or measured in the lab directly from known lava morphologies of Krafla. Consequently since the spectral data quality from in-situ is precise,

this might be reducing accuracy. We need to consider high quality spectral image data such as HyMap and AVIRIS to be comparable with in-situ measurement.

Using the same classification method, the multispectral data was unable to resolve the different lava morphologies in detail. As mentioned in section 5.3 multispectral has limited bands, in this study only seven bands were used. In an attempt to achieve a more reasonable classification in multispectral, we could pick more than one endmember spectral point from each class. These endmembers should be based on field knowledge and also spectral similarity. According to Inzana et al. (2003), the Landsat band ratio $5/4 \times 3/4$ can be used to successfully discriminate between mafic and non-mafic rocks (Fig. A1). Since common mafic rocks include basalt, this may be a viable option in the Krafla lava field. The image is then overlaid with a LIDAR image and DEM to see the intensity of backscattering and the height difference to distinguish the roughness of the lava morphology (Spinetti et al., 2009; Kassouk et al., 2014). This may lead to a new method where we can pick the endmember spectra according to those processes. This method could also be applied to hyperspectral images.

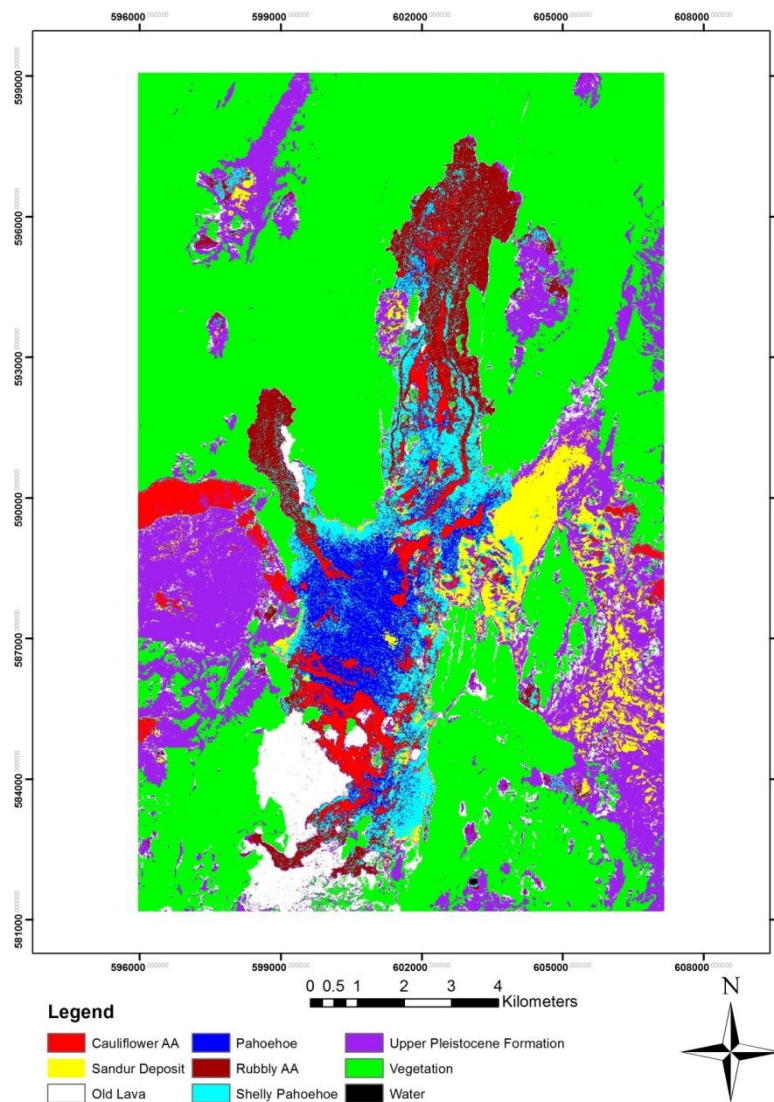


Fig. 60 Krafla's Lava morphology classification base on maximum likelihood classification.

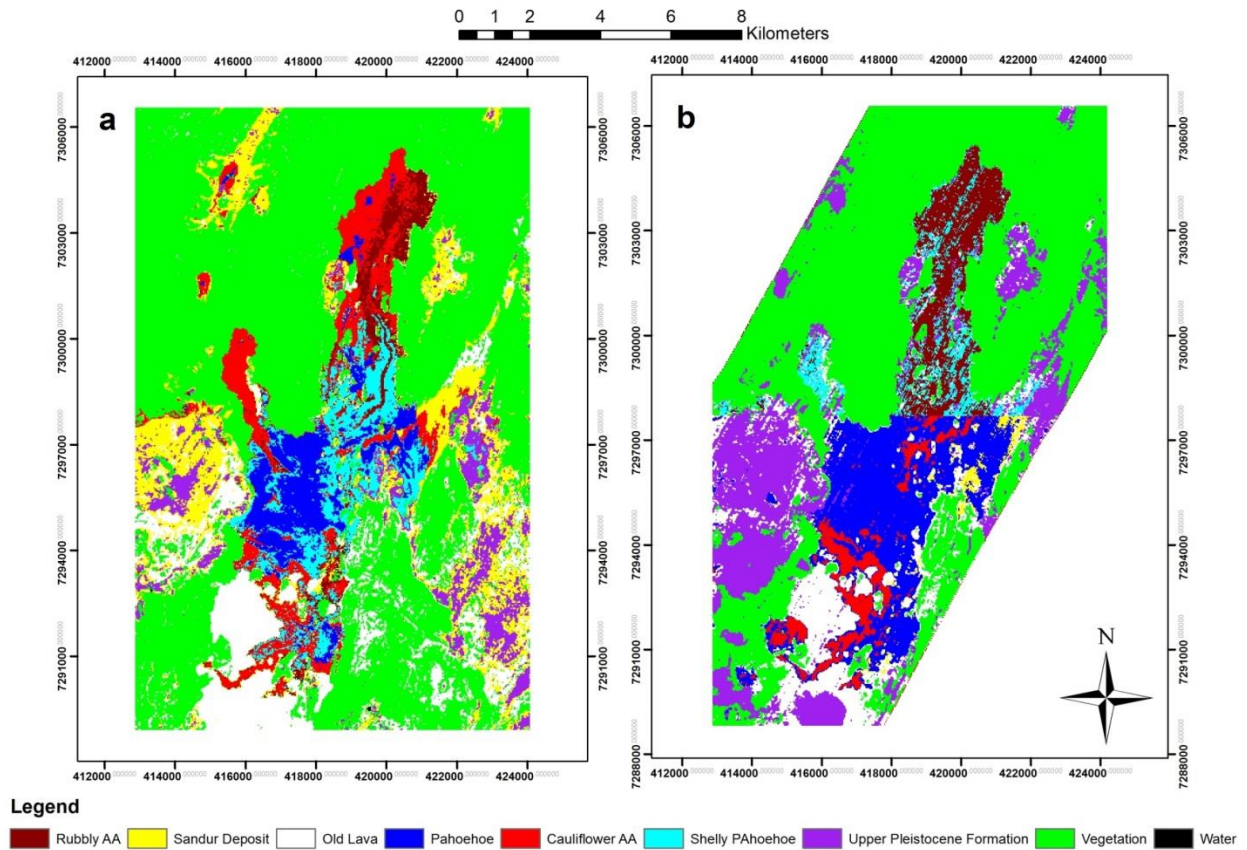


Fig. 61 (a) Landsat 8 OLI SAM classification result; (b) EO-1 Hyperion SAM classification result.

5.5 Lava Morphology Accuracy Assessment

The results of the accuracy assessment show that SPOT 5 images have an overall accuracy of 67.33%, Landsat 8 OLI of 52.67%, and EO-1 Hyperion of 63.33%. The detailed result of the accuracy assessment for each satellite is shown in Table 8 and includes user accuracy and producer accuracy for each morphology type tested. The effect of sample size, references, data quality on the accuracy and description of Kappa statistics will now be discussed.

5.5.1 Effect of sample size, references and data quality on accuracy assessment

Sample size is one of the effects that influence accuracy assessment as well as quality of reference data and of course as explained in section 5.4.1 and 5.4.2 the quality of classification itself. Modifying the sample size, however, will affect the accuracy of the map. Increasing the sample size will result in a higher precision of the estimated accuracy measures. Decreasing the sample size will lower the precision. A total of 150 samples were used in this study with random equal-stratified sampling, which means we have 30 samples for each class. In order to compare the results we generated 50 samples, 250 samples and 350 samples (Fig. 62). According to the graph, EO-1 Hyperion classified lava morphology map

has highest overall accuracy for both in lowest and highest sample (68% and 61.71%) but of course the precision for 350 samples is higher than just 50 samples.

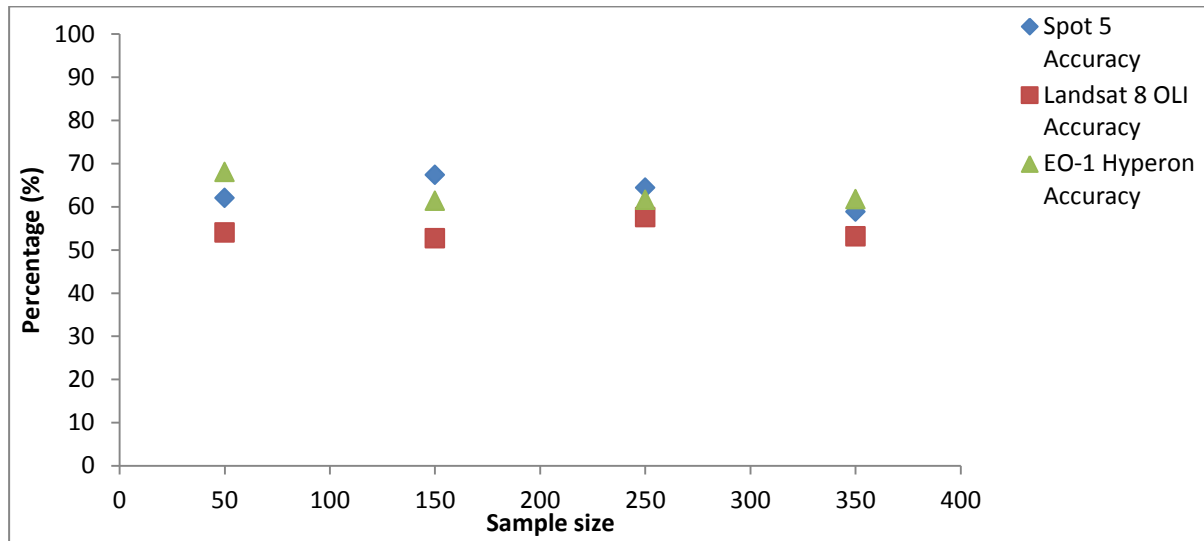


Fig. 62 Effect of sample size to accuracy assessment for different classified satellites data in Krafla lava field.

The accuracy of EO-1 Hyperion relatively increases in average 0.19% as increased of samples. Compared to EO-1 Hyperion, SPOT 5 classifications show a decrease in average 4.23%. However, the Landsat classifications have a relatively fluctuating accuracy but in general this classification has the lowest overall accuracy (below 60%) (Table 8). 50 samples per class is ideal for sample size as suggested by Lillesand and Kiefer (1987). That makes for a total of 350 sample points which is acceptable as the precision is higher.

As mentioned before, the error in ground ‘truth’ (reference) can lead to systematic bias. A bad reference will lead to poor assessment of accuracy. This could occur due to the reference data being recorded at a different time than the data; apparent errors might be due to the fact that the landscape has changed. As mentioned in section 5.1 the time difference between the reference maps and the new data is 10-16 years. To increase the accuracy of this method more accurate ground truth data is needed which is recorded around the same time as the study is carried out.

In section 4.3.5 it was explained that the EO-1 Hyperion data that was used in this thesis is not of a good quality. There are about 72 bands that were removed due to not having been calibrated, and the rest of those were filtered. As seen in Fig. 61b the stripping was not completely removed from the image and leads to stripping in the classification. This problem will impact on the accuracy as stripping may lead to false classifications.

Table 8. Results of overall, producer and user accuracy including the Kappa statistics for three satellites image(1) SPOT 5; (2) Landsat 8 OLI; and (3)EO-1 Hyperion.

Satellites Image	SPOT 5		Landsat 8 OLI		EO-1 Hyperion	
Lava Classes	User Accuracy	Producer Accuracy	User Accuracy	Producer Accuracy	User Accuracy	Producer Accuracy
Rubbly AA	66.67%	80%	60%	30%	68.57%	80%
Cauliflowers AA	59.09%	43.33%	33.33%	43.33%	76.47%	43.33%
Shelly Pahoehoe	57.14%	66.67%	51.72%	50%	64.29%	30%
Pahoehoe	78.26%	60%	62.50%	50%	58.54%	80%
Old Lava	100%	86.67%	93.10%	90%	75.86%	73.33%
Overall Accuracy	67.33%		52.67%		61.33%	
Kappa Statistics	0.597		0.4218		0.5277	

5.5.2 Descriptions of Kappa Statistics and Their Advances over Normal Accuracy Assessment

The results of the Kappa statistics from Table 8 show that SPOT 5 has 0.597, Landsat 8 OLI has 0.421 and EO-1 Hyperion has 0.5277. In general according to Congalton (1991) these values are considered to show moderate agreement between the classification and reference points. The Kappa statistics value is relatively lower than the overall accuracy because Kappa includes the error matrix in the calculation. Kappa statistics show the difference between how much agreement is actually present (“observed” agreement) and how much agreement would be expected to be present by chance alone (“expected” agreement). As an example SPOT 5 has the highest Kappa statistics value of 0.597; this means that only 59.7 % from the classification map that would result the actual lava morphology if we pick random points on the field. This principle also implies in EO-1 Hyperion which has 52.7% Kappa statistics and Landsat 8 OLI 42.1% Kappa statistics. According to the result the Kappa statistics shows an advance of the how well quality of the produced map is, rather than in normal accuracy assessment that more over only the percentage difference between reference data and the produced map.

6 Discussions

6.1 Identifying Lava Surface Morphology Using Remote Sensing

The SPOT 5, Landsat 8 OLI and Hyperion results indicate that, in general, these three satellites are capable of producing similar lava morphology maps as manual field mapping. Using maximum likelihood classification SPOT 5 is able to successfully discriminate the different lava morphologies in the Krafla lava field with a 67.33% overall. The main limitation of this method is that map that is produced is “too detailed”. This happens due to the high resolution which causes shadows and small patches to be classified as lava. This “too detailed” map can be a good advantage for the accuracy assessment if we have a very accurate lava morphology reference with a huge amount reference points. In this case since in this study only 150 reference points were used, it becomes a disadvantage to have very detailed classification in the accuracy assessment. In general the overall accuracy of SPOT 5 images is fairly acceptable to map lava morphology.

The result from the SAM method on EO-1 Hyperion data also successfully discriminates the lava morphologies in the Krafla lava field. The classification based on endmember spectra has an overall accuracy of 61.33%. However, the bad data and vertical stripping of the Hyperion images does affect the ability to extract spectral reflectance and identify individual lava morphologies. Meanwhile Landsat 8 OLI obtained 52.67% overall accuracy using the same method and endmember spectra. This accuracy result is the lowest of the satellite sources used in this study. The difference of spatial resolutions, spectral resolution and spectral range of Landsat caused a slight loss of spatial and spectral detail. Some of the spectral difference could be an effect of the pixel size, causing a greater mixing in the lava morphology spectra. Although the value of the overall accuracy cannot conclude the accuracy of individual lava morphology classes it can draw a conclusion for the overall map.

Furthermore, detailed comparison of the individual lava morphology accuracy of three satellite images using a confusion matrix approach demonstrates that the correspondence is not as good as may be thought from visual comparison and overall accuracy assessment. The majority of aa lava morphology (cauliflower and rubbly aa) classes have both low producer and user accuracy. To be acceptable the accuracy needs to be over 50%. If we look in cauliflower aa producer accuracy for three satellites image clearly show that only 43.33% of pixels classified as cauliflower aa have been correctly identified as cauliflowers aa. This result doesn't mean the satellites image are not good enough to identify cauliflower aa as we also need to consider the user accuracy. The user accuracy result from SPOT 5 of cauliflower aa show 59.09%. Therefore, despite the map produces only 43.33%, a user of this map will find that the map show 59.09% the actual cauliflowers aa. This condition also applies to the EO-1 Hyperion data which have 76.47% producer accuracy on cauliflower aa. This acceptable user accuracy reveals that the map is still reliable to identify cauliflower aa.

Landsat 8 OLI has low user accuracy for cauliflower aa (33.33%). This means that Landsat is not well-suited to identifying cauliflower lava morphology both as user and producer. As mentioned before in this section, this could be due to both spectral and spatial resolution on Landsat 8 OLI being relatively low compared to SPOT 5 and EO-1 Hyperion. EO-1 Hyperion produces 30% producer accuracy for shelly pahoehoe. This is the only value for pahoehoe

lava morphology for which accuracy falls below 50%. This is due to horizontal strip that occurred in the spectral endmember of shelly pahoehoe and also the vertical strips that appear in the western, centre (main concentration of shelly pahoehoe) and northern part in the Hyperion image. This also causes the accuracy of old lava to decrease in EO-1 Hyperion with around 73-75% on producer and user accuracy.

While these comparisons serve to highlight the accuracy and overall performance of the different satellites images, several other issues may affect the accuracy of lava surface morphology. These include the following:

1. Spatial resolution (SPOT 5 is 10 m, Landsat 8 OLI 30 m, Hyperion 30 m);
2. Image acquisition differences (date/time, atmospheric conditions,);
3. Slightly different spectral characteristics (varying band centers and spectral resolution);

Finally, the possibility of SPOT 5, Landsat 8 OLI and EO-1 Hyperion to identify individual lava flow morphologies using endmember spectra collection, maximum likelihood and spectral angle mapper classification have been handled in this thesis. According to the results, in general remote sensing is capable of mapping and assessing of detail lava morphology in Krafla lava field.

6.2 Lava Surface Morphology in the Krafla Lava Fields

There were several issues highlighted in this discussion. Since no fieldwork has been done and there is a lack of reference data in this study area, the lava morphology types in the Krafla lava field could be more than five types. This issue results in cauliflower aa and slabby pahoehoe mixed into one class. Small fragments of lava morphology like toothpaste that are associated in aa lava morphology are also not included in lava morphology as a separate class. Scoriaceous aa-clasts and large blocks of pahoehoe plates also appeared in the Krafla lava field as loose fragments and are mainly concentrated in the main lava channel. This issue could also affect the error in ground “truth” (reference points), since the small fragments and loose fragments might appear as a different morphology in remote sensing classification. Regarding those issues, lava morphology mixture into one classes have an advantage in classification for moderate spatial resolution, meanwhile for very high spatial resolution is disadvantage since the small fragments and loose fragments is detected as different morphology. If we want to produce very detailed lava morphology classifications (including loose fragments and small fragments without mixture) on moderate spatial resolution images, we need also to combine the image with a digital elevation model (DEM) and radar images in order to get a better understanding of roughness and height differences of mixtures of lava morphologies in the Krafla lava field. This mixture problem also gives an error effect in lava morphology spectral reflectance. Absorption features might not be accurate to reflect “real” morphology although in general lava spectral reflectance in Krafla is matching with basaltic lava. Since a systematic spectral radiometric survey of Krafla area has never been performed before, the experience and lessons from this study are important for designing future field work and for setting up a database structure and sampling to be used to update lava morphology maps and to study lava surface morphology classification in order to produce detail map of lava surface morphology in the future.

7 Concluded Remarks and Recommendations

7.1 Concluded Remarks

7.1.1 Lava Morphology Histogram Distributions

- Based on SPOT 5 histograms, in the Krafla lava field most of the non-lava has a relatively symmetrical histogram (except water) especially in band 2 (Red) and band 4 (SWIR), while the lava shows the asymmetrical histogram, relatively skewed and flat (except in old lava).
- The mean intensity plot of SPOT 5 shows that pahoehoe type lava has a higher reflectance than aa type lava, but there is no significant difference between pahoehoe sheet and shelly pahoehoe.
- On the SWIR band of SPOT 5 (band 4), the mean pixel intensity of cauliflower aa slightly drops with steeper slope compared to rubbly aa.
- Rubbly aa, pahoehoe and shelly pahoehoe have an overlap intensity with each other in feature space band 2 / band 4 and band 3 / band 4.
- Feature space plot in band 2 / band 4 show cauliflower aa has an intersecting value with pahoehoe, while in band 3 / band 4 shows the cauliflower aa has less intensity and did not have an intersection with any other lava morphology.

7.1.2 Lava Morphology Spectral Reflectance

- Spectral reflectance curves from hyperspectral images of the Krafla lava field is similar to the basaltic lava from laboratory measurements which is provided by ENVI and USGS (especially in four major absorptions features). The same conclusion cannot be drawn for multispectral data as this data does not have absorptions features due to limited bands.
- Both multispectral and hyperspectral data have higher reflectance on older lava from the Myvatn fires compared to the Krafla Fires and pahoehoe type lava shows higher reflectance than aa type lava.
- Multispectral data were not suited to identifying the detailed lava morphology spectral reflectance curves of cauliflower aa. On the other hand hyperspectral data were fairly good at identifying the lava morphology spectral reflectance curves.
- In Hyperspectral results, rubbly aa has absorption feature in between 2200-2300 nm and Shelly pahoehoe has overall spectra reflectance curves similar to the aa lava type especially in the Fe^{2+} and H_2O absorption feature bands.

7.1.2 Lava Morphology Mapping and Assessing

- The result map from the visual image interpretation show a total of seven classes (1) Rubbly aa; (2) old lava (1724-1729) (3) cauliflower aa and slabby pahoehoe; (4) pahoehoe; (5) shelly pahoehoe; (6) lava channel and (7) lava vent.
- Lava covered about 36.9 km² with 33.7% classified as pahoehoe, 27.3% as cauliflower aa, 15.1% as shelly pahoehoe, 20.6% as rubbly aa and the rest 3.3% as lava channel. While in overall percentage between pahoehoe and aa are relatively balance, 48.7% is pahoehoe and 47.9% is aa.
- Kappa statistics values in Krafla lava field suggest a moderate agreement between classification and reference points (0.42- 0.59).
- The accuracy result of lava morphology mapping of the SPOT 5 images using maximum likelihood classification method obtained 67.33% in overall accuracy (from 150 reference samples)
- The accuracy result of lava morphology mapping of the Landsat 8 OLI images using SAM method obtained 52.67% in overall accuracy (from 150 reference sample points)
- The accuracy result of lava morphology mapping of the EO-1 Hyperion images using SAM method obtained 61.33% in overall accuracy (from 150 reference sample points)

7.2 Recommendations

- Take more than one sample in the field as a training sample in SPOT 5 images which are 100% sure the sample represents the lava morphology class.
- Use the other option for classification of Landsat using band ratio 5/4*3/4 to discriminate between mafic and nonmafic rocks. Since common mafic rocks include basalt, this may be a viable option in Krafla lava field. After that overlay with radar image and DEM to see the intensity of backscattering and height difference to distinguish the roughness of lava morphology.
- The real ground truth in situ measurement of lava field reflectance spectra using ASD FieldSpec3 (Robertson et al., 2013) would be essential to collect from the study area in order to validate the Hyperion and Landsat images.
- Spectroscopy laboratory measurements of the Krafla lava field would give the reference of absorptions features of basaltic lava in Krafla lava field.
- Use airborne hyperspectral image data such as HyMap and AVIRIS could possible to improve detail of reflectance spectra and quality of data.
- 350 reference sample points (50 points per lava morphology classes) are acceptable for an accuracy assessment in the Krafla lava field since the precision is higher.

References

- Amici, S., Piscini, A., & Neri, M. (2014). Reflectance Spectra Measurements of Mt . Etna : A Comparison with Multispectral / Hyperspectral Satellite. *Advances in Remote Sensing*, 3(December), 235–245. doi:http://dx.doi.org/10.4236/ars.2014.34016
- Andrew, R. E. B. (2008). *Volcanotectonic Evolution and Characteristic Volcanism of the Neovolcanic Zone of Iceland*. Georg-August-Universität zu Göttingen.
- Bakx, W., Tempfli, K., Tolpekin, V., & Woldai, T. (2012). Physics. In V. Tolpekin & A. Stein (Eds.), *The Core of GIScience : a system-based approach* (pp. 71–92). Enschede: The International Institute for Geo-Information Science and Earth Observation (ITC).
- Beck, R. (2003). *EO-1 User Guide v. 2.3*.
- Bhardwaj, A., Joshi, P. K., Sam, L., Kumar, M., Singh, S., & Kumar, R. (2015). International Journal of Applied Earth Observation and Geoinformation Applicability of Landsat 8 data for characterizing glacier facies and supraglacial debris. *International Journal of Applied Earth Observations and Geoinformation*, 38, 51–64. doi:10.1016/j.jag.2014.12.011
- Björnsson, A. (1985). Dynamics of crustal rifting in NE Iceland. *Journal of Geophysical Research*, 90, 151–162. doi:10.1029/JB080i012p10151
- Byrnes, J. M., Ramsey, M. S., & Crown, D. a. (2004). Surface unit characterization of the Mauna Ulu flow field, Kilauea Volcano, Hawai'i, using integrated field and remote sensing analyses. *Journal of Volcanology and Geothermal Research*, 135(1-2), 169–193. doi:10.1016/j.jvolgeores.2003.12.016
- Congalton, R. . (1991). A review of assessing the accuracy of classifications of remotely sensed data. *Remote Sensing of Environment*, 37, 35–46.
- Dugmore, A., & Vésteinsson, O. (2012). *Black Sun, High Flame, and Flood: Volcanic Hazards in Iceland. Surviving Sudden Environmental Change*.
- Duraiswami, R. a., Bondre, N. R., & Managave, S. (2008). Morphology of rubbly pahoehoe (simple) flows from the Deccan Volcanic Province: Implications for style of emplacement. *Journal of Volcanology and Geothermal Research*, 177(4), 822–836. doi:10.1016/j.jvolgeores.2008.01.048
- Duraiswami, R. a., Gadpallu, P., Shaikh, T. N., & Cardin, N. (2014). Pahoehoe-a'a transitions in the lava flow fields of the western Deccan Traps, India-implications for emplacement dynamics, flood basalt architecture and volcanic stratigraphy. *Journal of Asian Earth Sciences*, 84, 146–166. doi:10.1016/j.jseas.2013.08.025
- Einarsson, P. (1991). *The Krafla rifting episode 1975–1989*. (A. Gardarsson & A. Einarsson, Eds.) *Náttúra Mývatns (The Nature of Lake Mývatns)*. Reykjavík: Icelandic Nature Sci. Soc.,.

- ESRI. (n.d.). ArcGIS Desktop. Retrieved from <http://help.arcgis.com/en/arcgisdesktop/10.0/help/index.html#/00170000002r000000>
- EXELIS. (2004). ENVI Atmospheric Correction Module: QUAC and FLAASH user's guide. Retrieved from <http://scholar.google.com/scholar?hl=en&btnG=Search&q=intitle:ENVI+Atmospheric+Correction+Module:+QUAC+and+FLAASH+user's+guide#0>
- Flynn, L. P., Harris, A. J. L., & Wright, R. (2001). Improved identification of volcanic features using Landsat 7 ETM+. *Remote Sensing of Environment*, 78(1-2), 180–193. doi:10.1016/S0034-4257(01)00258-9
- Girouard, G., & Bannari, a. (2004). Validated spectral angle mapper algorithm for geological mapping: comparative study between QuickBird and Landsat-TM. *XXth ISPRS Congress*, ..., 599–604. Retrieved from <http://www.isprs.org/proceedings/XXXV/congress/comm4/papers/432.pdf>
- Grönvold, K. (2008). *Volcanic geology of Krafla-Námafjall*. Retrieved December 14, 2014, from http://www.norvol.hi.is/html_i/geol_i/trip2_i.html
- Guðmundsson, A. T., & Kjartansson, H. (2007). *Living earth: Outline of the geology of Iceland*. Reykjavik: Mál og menning.
- Heitschmidt, G. W., Park, B., Lawrence, K. C., Windham, W. R., & Smith, D. P. (2007). Improved Hyperspectral Imaging System For Fecal Detection On Poultry Carcasses. *American Society of Agricultural and Biological Engineers*, 50(4), 1427–1432.
- Hirzel, A., & Guisan, A. (2002). Which is the optimal sampling strategy for habitat suitability modelling. *Ecological Modelling*, 157, 331–341. doi:10.1016/S0304-3800(02)00203-X
- Hjartardóttir, Á. R. (2013). *Fissure swarms of the Northern Volcanic Rift Zone , Iceland*. University of Iceland, Reykjavik.
- Hjartardóttir, Á. R., Einarsson, P., Bramham, E., & Wright, T. J. (2012). The Krafla fissure swarm, Iceland, and its formation by rifting events. *Bulletin of Volcanology*, 74, 2139–2153. doi:10.1007/s00445-012-0659-0
- Hon, K., Johnson, J., & Gansecki, C. (2008). *Field Interpretation of Active Volcano : A Handbook for viewing lava*. (T. Reveira, Ed.). Hawaii: U.S. Geological Survey Hawaiian Volcano Observatory.
- Inzana, J., Kusky, T., Higgs, G., & Tucker, R. (2003). Supervised classifications of Landsat TM band ratio images and Landsat TM band ratio image with radar for geological interpretations of central Madagascar. *Journal of African Earth Sciences*, 37, 59–72. doi:10.1016/S0899-5362(03)00071-X
- Jensen, J. R. (1996). *Introductory Digital Image Processing: A Remote Sensing Perspective* (Second.). Upper Saddle River, New Jersey, USA: Prentice Hall, Inc.

- John, J. St. (n.d.). *Craters of The Moon*. Retrieved from <http://www2.newark.ohio-state.edu/facultystaff/personal/jstjohn/Documents/Rocks-and-Fossils-in-the-Field/Craters-of-the-Moon-Lava-Field.htm>
- Kassouk, Z., Thouret, J.-C., Gupta, A., Solikhin, A., & Liew, S. C. (2014). Object-oriented classification of a high-spatial resolution SPOT5 image for mapping geology and landforms of active volcanoes: Semeru case study, Indonesia. *Geomorphology*, 221, 18–33. doi:10.1016/j.geomorph.2014.04.022
- Kennish, M. J., & Lutz, R. a. (1998). Morphology and distribution of lava flows on mid-ocean ridges: a review. *Earth Science Reviews*, 43, 63–90. doi:10.1016/S0012-8252(98)00006-3
- Kilburn, C. R. . (2000). Lava Flows And Flow Fields. In *Encyclopedia of Volcanoes*. Academic Press. doi:10.1029/00EO00168
- Kozák, J., & Vladimír, Č. (2010). Volcanism in Iceland. In *The Illustrated History of Natural Disasters* (pp. 79–83). Springer Netherlands. doi:10.1007/978-90-481-3325-3
- Lillesand, T. ., & Kiefer, R. . (1987). *Remote Sensing and Image Interpretation* (2nd ed.). Toronto: John Wiley and Sons, Inc. Retrieved from <http://nature.berkeley.edu/~penggong/textbook/reference.htm>
- Lombardo, V., & Buongiorno, M. F. (2006). Lava flow thermal analysis using three infrared bands of remote-sensing imagery: A study case from Mount Etna 2001 eruption. *Remote Sensing of Environment*, 101(2), 141–149. doi:10.1016/j.rse.2005.12.008
- Lu, Z., Rykhus, R., Masterlark, T., & Dean, K. G. (2004). Mapping recent lava flows at Westdahl Volcano, Alaska, using radar and optical satellite imagery. *Remote Sensing of Environment*, 91(3-4), 345–353. doi:10.1016/j.rse.2004.03.015
- Lwin, K. K. (2008). *Fundamentals of Remote Sensing and its Application in GIS*. Tsukuba: University of Tsukuba.
- Michalski, J. R., Kraft, M. D., Sharp, T. G., & Christensen, P. R. (2006). Effects of chemical weathering on infrared spectra of Columbia River Basalt and spectral interpretations of martian alteration. *Earth and Planetary Science Letters*, 248(3-4), 822–829. doi:10.1016/j.epsl.2006.06.034
- Murcia, H., Németh, K., Moufti, M. R., Lindsay, J. M., El-Masry, N., Cronin, S. J., ... Smith, I. E. M. (2014). Late Holocene lava flow morphotypes of northern Harrat Rahat, Kingdom of Saudi Arabia: Implications for the description of continental lava fields. *Journal of Asian Earth Sciences*, 84, 131–145. doi:10.1016/j.jseaes.2013.10.002
- Newland, D. (1999). *Evaluation of Stepwise Spectral Unmixing with HYDICE Data*. Rochester Institute of Technology. Retrieved from <http://www.cis.rit.edu/research/thesis/bs/1999/newland/thesis.html>

- Pedersen, G. B. ., Höskuldsson, Á., Riishuus, M. ., Jónsdóttir, I., Gudmundsson, M. ., Sigmundsson, F., ... Þórdarson, Þ. (2015). Nornahraun Lava Morphology and Emplacement: A New Terrestrial Analogue For Planetary Lava Flows. In *46th Lunar and Planetary Science Conference*. Houston. doi:10.1038/nature14111.
- Pour, A. . (2014). *Hydrothermal alteration mapping using Landsat-8 data, Sar Cheshmeh copper mining district, SE Iran*. *Journal of Taibah University for Science*. Elsevier. doi:10.1016/j.seizure.2014.02.015
- Rashmi, S., Addamani, S., & Ravikiran, S. (2014). Spectral Angle Mapper Algorithm for Remote Sensing Image Classification. *IJSET - International Journal of Innovative Science, Engineering & Technology*, 1(4), 201–205.
- Richards, J. (1999). *Remote Sensing Digital Image Analysis*. Berlin: Springer Netherlands.
- Richards, J. ., & Jia, X. (2006). *Remote Sensing Digital Image Analysis* (4th ed.). Berlin: Springer-Verlag.
- Robertson, K. M., Milliken, R. E., Ruff, S., Farmer, J., & Shock, E. (2013). Can Vis-Nir Reflectance Spectra Be Used To Assess Formation Environments of Opaline Silica on Mars? In *44th Lunar and Planetary Science Conference* (pp. 2–3). Texas.
- Rossi, M. J. (1997). Morphology of the 1984 open-channel lava flow at Krafla volcano, northern Iceland. *Geomorphology*, 20(1-2), 95–112. doi:10.1016/S0169-555X(97)00007-X
- Rossi, M. J., & Gudmundsson, a. (1996). The morphology and formation of flow-lobe tumuli on Icelandic shield volcanoes. *Journal of Volcanology and Geothermal Research*, 72(96), 291–308. doi:10.1016/0377-0273(96)00014-5
- Ruffin, C., & King, R. L. (1999). The analysis of hyperspectral data using Savitzky-Golay filtering-theoretical basis. 1. *IEEE 1999 International Geoscience and Remote Sensing Symposium. IGARSS'99 (Cat. No.99CH36293)*, 2(Part 1), 1–3. doi:10.1109/IGARSS.1999.774430
- Shaw, G. ., & Burke, H. . (2003). Spectral Imaging for Remote Sensing. *LINCOLN LABORATORY JOURNAL*, 14(1), 3–28. doi:10.1007/BF02836169
- Smets, B., Wauthier, C., & d'Oreye, N. (2010). A new map of the lava flow field of Nyamulagira (D.R. Congo) from satellite imagery. *Journal of African Earth Sciences*, 58(5), 778–786. doi:10.1016/j.jafrearsci.2010.07.005
- Smithsonian Institution. (2013a). *Global Volcanism Program / Krafla*. Retrieved December 13, 2014, from http://www.volcano.si.edu/volcano.cfm?vn=373080#bgvn_198905
- Smithsonian Institution. (2013b). *Kröflueldar - the black area around Krafla*. Retrieved December 14, 2014, from http://www.geocaching.com/geocache/GC4F8B5_kroflueldar-the-black-area-around-krafla?guid=3bb5fcef-a0c7-4a82-a4db-0a91edb34a41

- Spinetti, C., Mazzarini, F., Casacchia, R., Colini, L., Neri, M., Behncke, B., ... Pareschi, M. T. (2009). Spectral properties of volcanic materials from hyperspectral field and satellite data compared with LiDAR data at Mt. Etna. *International Journal of Applied Earth Observation and Geoinformation*, 11(2), 142–155. doi:10.1016/j.jag.2009.01.001
- Sun, D. . (2010). *Hyperspectral Imaging for Food Quality Analysis and Control*. Elsevier. Retrieved from <https://books.google.com/books?id=FVTbineZq54C&pgis=1>
- Tarquini, S., & Favalli, M. (2011). Mapping and DOWNFLOW simulation of recent lava flow fields at Mount Etna. *Journal of Volcanology and Geothermal Research*, 204(1-4), 27–39. doi:10.1016/j.jvolgeores.2011.05.001
- Thordarson, T., & Hoskuldsson, A. (2014). *Iceland. Classic Geology in Europe 3* (2nd ed.). London: Dunedin Academic Press Ltd. Retrieved from <http://library.wur.nl/WebQuery/clc/1718839>
- Thordarson, T., & Höskuldsson, Á. (2008). Postglacial volcanism in Iceland. *JÖKULL*, (58), 197–228.
- Thordarson, T., & Larsen, G. (2007). Volcanism in Iceland in historical time: Volcano types, eruption styles and eruptive history. *Journal of Geodynamics*, 43(1), 118–152. doi:10.1016/j.jog.2006.09.005
- Timmermans, W. (1995). *Remote Sensing Evapotranspiration*. Delft University of Technology, Faculty of Civil Engineering.
- USGS. (n.d.-a). *Using the USGS Landsat 8 Product*. Retrieved February 10, 2015, from http://landsat.usgs.gov/Landsat8_Using_Product.php
- USGS. (n.d.-b). *What are the band designations for the Landsat satellites?* Retrieved January 26, 2015, from http://landsat.usgs.gov/band_designations_landsat_satellites.php
- Van Der Meer, F. (2006). Basic Physics of Spectrometry. In *Imaging Spectrometry, Basic Principles and Prospective Applications* (pp. 1–6). Dordrecht: Springer.
- Wohletz, K., & Heiken, G. (1992). *Volcanology and Geothermal Energy*. Berkeley: University of California Press. Retrieved from <http://ark.cdlib.org/ark:/13030/ft6v19p151/>
- Zaini, N. (2009). *Calcite-Dolomite Mapping to Assess Dolomitization Patterns Using Laboratory Spectra and Hyperspectral Remote Sensing : A Case Study of Bédarieux Mining Area , SE France*. International Institute for Geo-Information Science and Earth Observation.

Appendix I

Table A1. Hyperion spectral coverage and detail of not calibrated bands (Beck, 2003)

Hyperion Band	Average Wavelength (nm)	Full Width at Half the Maximum FWHM (nm)	Spatial Resolution (m)	Not Calibrated (X)
B1	355.5900	11.3871	30	X
B2	365.7600	11.3871	30	X
B3	375.9400	11.3871	30	X
B4	386.1100	11.3871	30	X
B5	396.2900	11.3871	30	X
B6	406.4600	11.3871	30	X
B7	416.6400	11.3871	30	X
B8	426.8200	11.3871	30	
B9	436.9900	11.3871	30	
B10	447.1700	11.3871	30	
B11	457.3400	11.3871	30	
B12	467.5200	11.3871	30	
B13	477.6900	11.3871	30	
B14	487.8700	11.3784	30	
B15	498.0400	11.3538	30	
B16	508.2200	11.3133	30	
B17	518.3900	11.2580	30	
B18	528.5700	11.1907	30	
B19	538.7400	11.1119	30	
B20	548.9200	11.0245	30	
B21	559.0900	10.9321	30	
B22	569.2700	10.8368	30	
B23	579.4500	10.7407	30	
B24	589.6200	10.6482	30	
B25	599.8000	10.5607	30	
B26	609.9700	10.4823	30	
B27	620.1500	10.4147	30	
B28	630.3200	10.3595	30	
B29	640.5000	10.3188	30	
B30	650.6700	10.2942	30	
B31	660.8500	10.2856	30	
B32	671.0200	10.2980	30	
B33	681.2000	10.3349	30	
B34	691.3700	10.3909	30	
B35	701.5500	10.4592	30	

B36	711.7200	10.5322	30	
B37	721.9000	10.6004	30	
B38	732.0700	10.6562	30	
B39	742.2500	10.6933	30	
B40	752.4300	10.7058	30	
B41	762.6000	10.7276	30	
B42	772.7800	10.7907	30	
B43	782.9500	10.8833	30	
B44	793.1300	10.9938	30	
B45	803.3000	11.1044	30	
B46	813.4800	11.1980	30	
B47	823.6500	11.2600	30	
B48	833.8300	11.2824	30	
B49	844.0000	11.2822	30	
B71	851.9200	11.0457	30	X
B50	854.1800	11.2816	30	
B72	862.0100	11.0457	30	X
B51	864.3500	11.2809	30	
B73	872.1000	11.0457	30	X
B52	874.5300	11.2797	30	
B74	882.1900	11.0457	30	X
B53	884.7000	11.2782	30	
B75	892.2800	11.0457	30	X
B54	894.8800	11.2771	30	
B76	902.3600	11.0457	30	X
B55	905.0500	11.2765	30	
B77	912.4500	11.0457	30	
B56	915.2300	11.2756	30	
B78	922.5400	11.0457	30	
B57	925.4100	11.2754	30	
B79	932.6400	11.0457	30	
B58	935.5800	11.2754	30	X
B80	942.7300	11.0457	30	
B59	945.7600	11.2754	30	X
B81	952.8200	11.0457	30	
B60	955.9300	11.2754	30	X
B82	962.9100	11.0457	30	
B61	966.1100	11.2754	30	X
B83	972.9900	11.0457	30	
B62	976.2800	11.2754	30	X
B84	983.0800	11.0457	30	
B63	986.4600	11.2754	30	X
B85	993.1700	11.0457	30	
B64	996.6300	11.2754	30	X
B86	1003.3000	11.0457	30	

B65	1006.8100	11.2754	30	X
B87	1013.3000	11.0457	30	
B66	1016.9800	11.2754	30	X
B88	1023.4000	11.0451	30	
B67	1027.1600	11.2754	30	X
B89	1033.4900	11.0423	30	
B68	1037.3300	11.2754	30	X
B90	1043.5900	11.0372	30	
B69	1047.5100	11.2754	30	X
B91	1053.6900	11.0302	30	
B70	1057.6800	11.2754	30	X
B92	1063.7900	11.0218	30	
B93	1073.8900	11.0122	30	
B94	1083.9900	11.0013	30	
B95	1094.0900	10.9871	30	
B96	1104.1900	10.9732	30	
B97	1114.1900	10.9572	30	
B98	1124.2800	10.9418	30	
B99	1134.3800	10.9248	30	
B100	1144.4800	10.9065	30	
B101	1154.5800	10.8884	30	
B102	1164.6800	10.8696	30	
B103	1174.7700	10.8513	30	
B104	1184.8700	10.8335	30	
B105	1194.9700	10.8154	30	
B106	1205.0700	10.7979	30	
B107	1215.1700	10.7822	30	
B108	1225.1700	10.7663	30	
B109	1235.2700	10.7520	30	
B110	1245.3600	10.7385	30	
B111	1255.4600	10.7270	30	
B112	1265.5600	10.7174	30	
B113	1275.6600	10.7091	30	
B114	1285.7600	10.7022	30	
B115	1295.8600	10.6970	30	
B116	1305.9600	10.6946	30	
B117	1316.0500	10.6937	30	
B118	1326.0500	10.6949	30	
B119	1336.1500	10.6996	30	
B120	1346.2500	10.7058	30	
B121	1356.3500	10.7163	30	
B122	1366.4500	10.7283	30	
B123	1376.5500	10.7437	30	
B124	1386.6500	10.7612	30	
B125	1396.7400	10.7807	30	

B126	1406.8400	10.8034	30	
B127	1416.9400	10.8267	30	
B128	1426.9400	10.8534	30	
B129	1437.0400	10.8818	30	
B130	1447.1400	10.9110	30	
B131	1457.2300	10.9422	30	
B132	1467.3300	10.9743	30	
B133	1477.4300	11.0074	30	
B134	1487.5300	11.0414	30	
B135	1497.6300	11.0759	30	
B136	1507.7300	11.1108	30	
B137	1517.8300	11.1461	30	
B138	1527.9200	11.1811	30	
B139	1537.9200	11.2156	30	
B140	1548.0200	11.2496	30	
B141	1558.1200	11.2826	30	
B142	1568.2200	11.3146	30	
B143	1578.3200	11.3460	30	
B144	1588.4200	11.3753	30	
B145	1598.5100	11.4037	30	
B146	1608.6100	11.4302	30	
B147	1618.7100	11.4538	30	
B148	1628.8100	11.4760	30	
B149	1638.8100	11.4958	30	
B150	1648.9000	11.5133	30	
B151	1659.0000	11.5286	30	
B152	1669.1000	11.5404	30	
B153	1679.2000	11.5505	30	
B154	1689.3000	11.5580	30	
B155	1699.4000	11.5621	30	
B156	1709.5000	11.5634	30	
B157	1719.6000	11.5617	30	
B158	1729.7000	11.5563	30	
B159	1739.7000	11.5477	30	
B160	1749.7900	11.5346	30	
B161	1759.8900	11.5193	30	
B162	1769.9900	11.5002	30	
B163	1780.0900	11.4789	30	
B164	1790.1900	11.4548	30	
B165	1800.2900	11.4279	30	
B166	1810.3800	11.3994	30	
B167	1820.4800	11.3688	30	
B168	1830.5800	11.3366	30	
B169	1840.5800	11.3036	30	
B170	1850.6800	11.2696	30	

B171	1860.7800	11.2363	30	
B172	1870.8700	11.2007	30	
B173	1880.9800	11.1666	30	
B174	1891.0700	11.1333	30	
B175	1901.1700	11.1018	30	
B176	1911.2700	11.0714	30	
B177	1921.3700	11.0424	30	
B178	1931.4700	11.0155	30	
B179	1941.5700	10.9912	30	
B180	1951.5700	10.9698	30	
B181	1961.6600	10.9508	30	
B182	1971.7600	10.9355	30	
B183	1981.8600	10.9230	30	
B184	1991.9600	10.9139	30	
B185	2002.0600	10.9083	30	
B186	2012.1500	10.9069	30	
B187	2022.2500	10.9057	30	
B188	2032.3500	10.9013	30	
B189	2042.4500	10.8951	30	
B190	2052.4500	10.8854	30	
B191	2062.5500	10.8740	30	
B192	2072.6500	10.8591	30	
B193	2082.7500	10.8429	30	
B194	2092.8400	10.8242	30	
B195	2102.9400	10.8039	30	
B196	2113.0400	10.7820	30	
B197	2123.1400	10.7592	30	
B198	2133.2400	10.7342	30	
B199	2143.3400	10.7092	30	
B200	2153.3400	10.6834	30	
B201	2163.4300	10.6572	30	
B202	2173.5300	10.6312	30	
B203	2183.6300	10.6052	30	
B204	2193.7300	10.5803	30	
B205	2203.8300	10.5560	30	
B206	2213.9300	10.5328	30	
B207	2224.0300	10.5101	30	
B208	2234.1200	10.4904	30	
B209	2244.2200	10.4722	30	
B210	2254.2200	10.4552	30	
B211	2264.3200	10.4408	30	
B212	2274.4200	10.4285	30	
B213	2284.5200	10.4197	30	
B214	2294.6100	10.4129	30	
B215	2304.7100	10.4088	30	

B216	2314.8100	10.4077	30	
B217	2324.9100	10.4077	30	
B218	2335.0100	10.4077	30	
B219	2345.1100	10.4077	30	
B220	2355.2100	10.4077	30	
B221	2365.2000	10.4077	30	
B222	2375.3000	10.4077	30	
B223	2385.4000	10.4077	30	
B224	2395.5000	10.4077	30	
B225	2405.6000	10.4077	30	X
B226	2415.7000	10.4077	30	X
B227	2425.8000	10.4077	30	X
B228	2435.8900	10.4077	30	X
B229	2445.9900	10.4077	30	X
B230	2456.0900	10.4077	30	X
B231	2466.0900	10.4077	30	X
B232	2476.1900	10.4077	30	X
B233	2486.2900	10.4077	30	X
B234	2496.3900	10.4077	30	X
B235	2506.4800	10.4077	30	X
B236	2516.5900	10.4077	30	X
B237	2526.6800	10.4077	30	X
B238	2536.7800	10.4077	30	X
B239	2546.8800	10.4077	30	X
B240	2556.9800	10.4077	30	X
B241	2566.9800	10.4077	30	X
B242	2577.0800	10.4077	30	X

Table A1. (Continued) Hyperion spectral coverage and detail of not calibrated bands (Beck, 2003)

Table A2. SPOT 5 image Overall statistics of lava morphology in the Krafla lava field.

Lava Morphology	Band	Min	Max	Mean	Overall Mean	Standard Deviation
Cauliflowers AA	1	12	14	12.72	21.045	0.543
	2	21	24	22.67		0.672
	3	30	33	31		0.548
	4	16	20	17.78		0.783
Rubbly AA	1	14	16	14.42	23.389	0.581
	2	24	26	23.8		0.624
	3	32	33	31.52		0.598
	4	24	28	23.82		1.189
Pahoehoe	1	13	18	15.59	25.05075	0.807
	2	23	30	26.79		1.018
	3	32	38	35.21		0.919
	4	19	25	22.61		1.186
Shelly Pahoehoe	1	12	20	15.25	24.86975	0.864
	2	22	30	26.22		1.077
	3	30	37	34.17		0.962
	4	20	28	23.83		1.185
Old lava	1	15	36	25.91	36.5555	2.039
	2	23	39	30.81		1.589
	3	32	41	36.7		1.165
	4	41	69	52.81		3.443

Appendix II

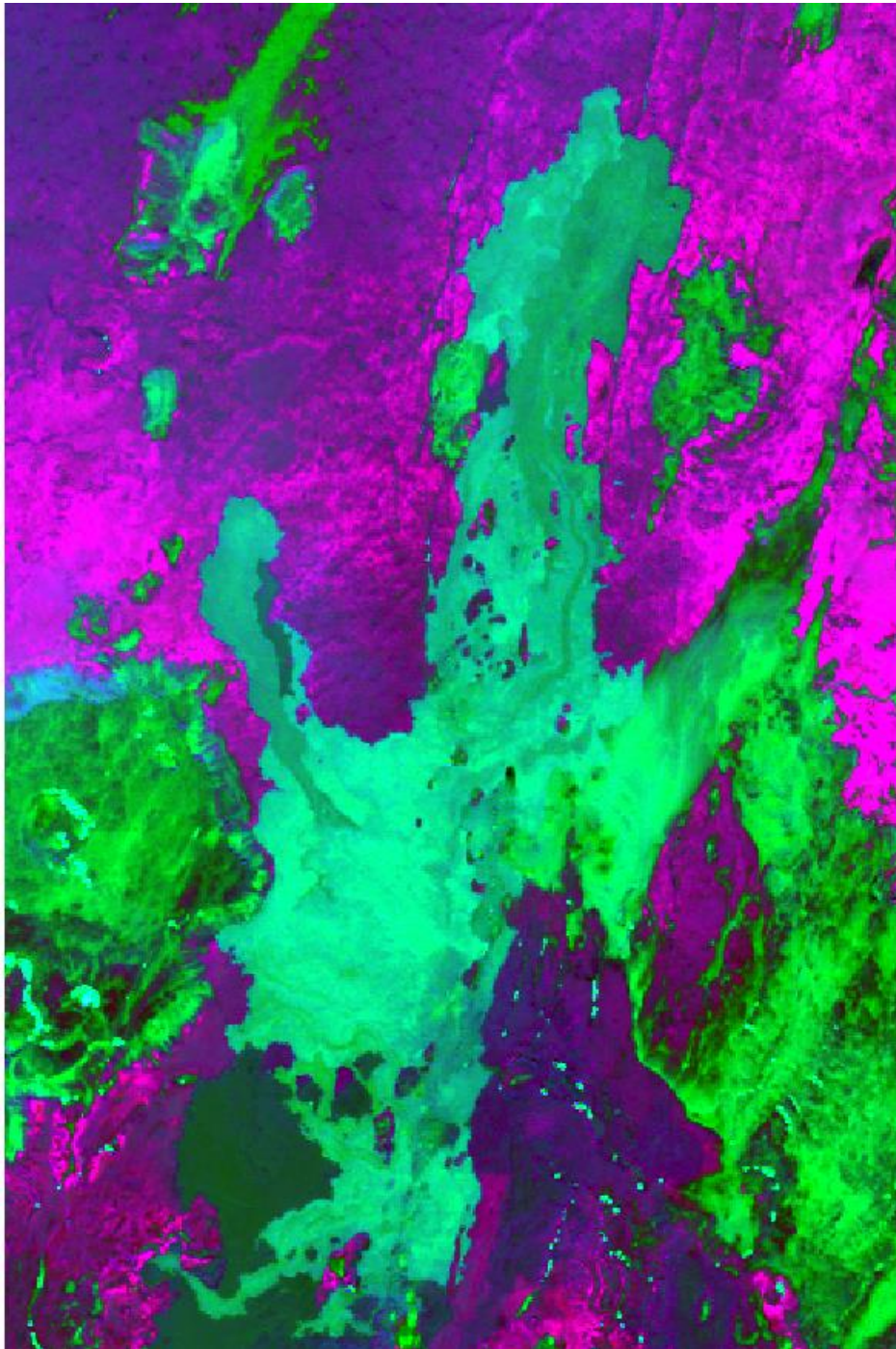


Fig. A1 Band ratio $5/4 \times 3/4$ on Landsat 8 to discriminate between mafic and nonmafic rocks